Novel Methods to Incorporate Physiological Prior Knowledge into the Inverse Problem of Electrocardiography

Application to Localization of Ventricular Excitation Origins

Zur Erlangung des akademischen Grades eines

DOKTOR-INGENIEURS

von der KIT-Fakultät für

Elektrotechnik und Informationstechnik

des Karlsruher Instituts für Technologie (KIT)

genehmigte

DISSERTATION

von

Steffen Friedrich Schuler, M.Sc.

geb. in Schwäbisch Gmünd
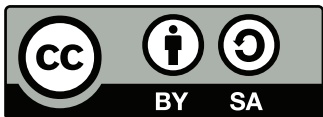
Abstract

17 million deaths a year worldwide are linked to cardiovascular diseases. Sudden cardiac death is one result in approximately 25% of all patients with cardiovascular diseases and may be connected to ventricular tachycardia. When treating the ventricular tachycardia with a catheter intervention, the detection of the so-called exit points, i.e. the spatial origin of the excitation, is a crucial step. As this procedure is very time consuming and skilled cardiologists are required, there is a need for assisting localization procedures, preferably automatic and non-invasive ones. Electrocardiographic imaging tries to meet these needs by reconstructing the electrical activity of the heart from body surface potential measurements. The resulting information can be used to reconstruct the excitation origin. However, current methods for solving this inverse problem show either low precision or poor robustness, which limits their clinical utility. This work first analyzes the forward problem in combination with two source models: transmembrane voltages and extracellular potentials. The mathematical properties of the relation between sources on the heart and the body surface potentials are analyzed systematically and the impact on the inverse problem is explained and visualized. Subsequently, this knowledge is used to solve the inverse problem. Three novel methods are introduced: Delay-based regularization, body surface potential regression, and deep learning-based localization. These three methods are compared to four state-of-the-art methods using one simulated and two clinical datasets. On the simulated as well as one clinical dataset, one of the novel methods outperformed the existing approaches, whereas on the remaining clinical dataset, Tikhonov regularization performed best. Potential reasons for these results are discussed and related to properties of the forward problem.

Zusammenfassung

17 Millionen Todesfälle jedes Jahr werden auf kardiovaskuläre Erkankungen zurückgeführt. Plötzlicher Herztod tritt bei ca. 25% der Patienten mit kardiovaskulären Erkrankungen auf und kann mit ventrikulärer Tachykardie in Verbindung gebracht werden. Ein wichtiger Schritt für die Behandlung von ventrikulärer Tachykardie ist die Detektion sogenannter Exit-Points, d.h. des räumlichen Ursprungs der Erregung. Da dieser Prozess sehr zeitaufwändig ist und nur von fähigen Kardiologen durchgeführt werden kann, gibt es eine Notwendigkeit für assistierende Lokalisationsmöglichkeiten, idealerweise automatisch und nichtinvasiv. Elektrokardiographische Bildgebung versucht, diesen klinischen Anforderungen zu genügen, indem die elektrische Aktivität des Herzens aus Messungen der Potentiale auf der Körperoberfläche rekonstruiert wird. Die resultierenden Informationen können verwendet werden, um den Erregungsursprung zu detektieren. Aktuelle Methoden um das inverse Problem zu lösen weisen jedoch entweder eine geringe Genauigkeit oder Robustheit auf, was ihren klinischen Nutzen einschränkt. Diese Arbeit analysiert zunächst das Vorwärtsproblem im Zusammenhang mit zwei Quellmodellen: Transmembranspannungen und extrazelluläre Potentiale. Die mathematischen Eigenschaften der Relation zwischen den Quellen des Herzens und der Körperoberflächenpotentiale werden systematisch analysiert und der Einfluss auf das inverse Problem verdeutlicht. Dieses Wissen wird anschließend zur Lösung des inversen Problems genutzt. Hierzu werden drei neue Methoden eingeführt: eine verzögerungsbasierte Regularisierung, eine Methode basierend auf einer Regression von Körperoberflächenpotentialen und eine Deep-Learning-basierte Lokalisierungsmethode. Diese drei Methoden werden in einem simulierten und zwei klinischen Setups vier etablierten Methoden gegenübergestellt und bewertet. Auf dem simulierten Datensatz und auf einem der beiden klinischen Datensätze erzielte eine der neuen Methoden bessere Ergebnisse als die konventionellen Ansätze, während Tikhonov-Regularisierung auf dem verbleibenden klinischen Datensatz die besten Ergebnisse erzielte. Potentielle Ursachen für diese Ergebnisse werden diskutiert und mit Eigenschaften des Vorwärtsproblems in Verbindung gebracht.

Acknowledgments

I enjoyed being part of the Institute of Biomedical Engineering (IBT), which is characterized by a spirit of freedom, mutual respect and scientific curiosity. Furthermore, I am glad that I had the chance to work on an exciting topic – although the inverse problem sometimes also made myself a little ill-conditioned.

For giving me these opportunities and for the faithful supervision with an immense expertise, I am grateful to Prof. Olaf Dössel.

For his energetic support and the ongoing commitment to keep the IBT running, I want to deeply thank Axel Loewe.

For inspiring discussions on ECGI, his interest in my work and for refereeing this thesis, I would like to thank Prof. Dana Brooks.

I am extremely thankful for the collaboration within the Consortium for ECG Imaging. In particular, I want to thank: Prof. Rob MacLeod, María Guillem, Matthijs Cluitmans, Laura Bear, Jaume Coll-Font, Jess Tate, Brian Zenger and Jake Bergquist.

Special thanks goes to Danila Potyagaylo for the great collaboration.

I want to thank all colleagues at IBT and my students. Some have become good friends. Thank you...
Lukas Baron – for the countless visits at Chicco.
Yannick Lutz – for the fantastic time in 409 and on MTB trails.
Nicolas Pilia – for good coffee, mental support and our fruitful collaboration.
Andreas Wachter – for the many beers we had together, which made life much more endurable, and for enduring me in the final phase of the PhD.
Michael Kircher – for cool discussions about inverse problems.
Ekaterina Kovacheva & Tobias Gerach – for the positive energy surrounding CardioMechanics.
Laura Unger – for being one of the most trustworthy colleagues and for the trips into the gym.
Ady Naber – for being a pleasant companion and your loyalty after moving to the third floor.
Mark Nothstein – for the continuous motivation to "go steep".
Matthias Schaufelberger – for being a great student and colleague.
Maike Rees, Gerald Moik and Pedro Álvarez Guirado – it was a pleasure to work with you.

For the financial support, I wish to thank the German Research Foundation (DFG).

Finally, my greatest and warmest thanks go to my family – thank you for the unconditional support even in difficult times!

Contents

Abbreviations

AT	activation time
BC	body surface potential (BSP) correlation
BEM	boundary element method
BR	BSP regression
BSP	body surface potential
CC BY 4.0	Creative Commons Attribution 4.0 International, https://creativecommons.org/licenses/by/4.0/
CNN	convolutional neural network
Cobiveco	Consistent Biventricular Coordinates
CRT	cardiac resynchronization therapy
CT	computed tomography
CV	conduction velocity
DLL	deep-learning-based localization
DR	delay-based regularization
ECG	electrocardiography
ECGI	electrocardiographic imaging
EDL	equivalent dipole layer
EEP	epi- and endocardial potential
EP	extracellular potential
FIM	fast iterative method
GSVD	generalized singular value decomposition
HWHM	half-width at half-maximum
LA	left atrium
LDRB	Laplace-Dirichlet rule-based
LQF	local quadratic fit
LV	left ventricle
MAD	median absolute deviation
MINRES	minimum residual method
PP	pericardial potential
PSF	point spread function
RA	right atrium
rRMSE	relative root-mean-square error
RV	right ventricle

SNR   signal-to-noise ratio
SSM   statistical shape model
STA   spatio-temporal activation time (AT) estimation
SVD   singular value decomposition
TA   temporal AT estimation
Tik   second-order Tikhonov regularization
TikGS   Tikhonov-Greensite regularization
TMV   transmembrane voltage
TND   temporal non-decreasing regularization
UVC   Universal Ventricular Coordinates
VT   ventricular tachycardia
WGN   white Gaussian noise

Chapter 1

Introduction

Electrocardiography (ECG) is the standard tool for assessment of cardiac electrical activity. However, its interpretation requires a lot of experience and its diagnostical value is limited. More comprehensive information can be obtained using body surface potential (BSP) mapping and by solving an inverse problem to reconstruct the sources of BSPs. This approach can facilitate the detection of causes for arrhythmic diseases such as ectopic foci and ventricular tachycardia (VT). However, the inverse problem is severely ill-posed and requires regularization to obtain a plausible estimation of the cardiac sources. The goal of this work is to analyze the reasons for existing problems in electrocardiographic imaging (ECGI) such as the occurence of ambiguities. For this reason, we develop methods to analyze current difficulties and to incorporate a priori knowledge into the estimation of cardiac sources and the subsequent estimation of activation times (ATs). The main result of this thesis are three original methods which are analyzed and compared with four existing approaches. We evaluate all methods on a simulated and two clinical datasets.

1.1   Structure of the Thesis

Part I – Fundamentals

- **Chapter 2** provides an introduction into cardiac anatomy and electrophysiology, electro-cardiography and abnormal heart rhythms relevant for this work.
- **Chapter 3** describes concepts and numerical methods for modeling the bioelectric fields and the excitation of the heart.
- **Chapter 4** covers basics of the inverse problem of electrocardiography.

Part II – General Tools and Analyses

- **Chapter 5** presents a new biventricular coordinate system to describe local positions in the heart.
- **Chapter 6** provides a comparison of two surface source models by analyzing their transfer coefficients.
- **Chapter 7** introduces new transmural and anisotropic regularization operators.
- **Chapter 8** describes a method for spatial downsampling of surface sources, which allows fast calculations of body surface potentials.

Part III – Solving the Inverse Problem

- **Chapter 9** describes state-of-the-art methods to solve the inverse problem.
- **Chapter 10** presents three novel methods proposed to solve the inverse problem.
- **Chapter 11** introduces methods for post-processing of inverse solutions to obtain diagnostically relevant information.

Part IV – Evaluation

- **Chapter 12** presents an evaluation of inverse methods using simulations.
- **Chapter 13** presents an evaluation of inverse methods using clinical data recorded in cardiac resynchronization therapy patients.
- **Chapter 14** presents an evaluation of inverse methods using clinical data recorded in patients with ventricular tachycardia.

Part V – Final Remarks

- **Chapter 15** provides an overall discussion of the results on all datasets.
- **Chapter 16** summarizes the main findings.
- **Chapter 17** describes ideas for future directions.

FUNDAMENTALS

Medical Fundamentals

2.1 Human Heart

2.1.1 Anatomy and Circulation

The human heart (Fig. 2.1) is a hollow muscular organ located between the lungs, under and slightly to the left of the breastbone. It fulfills the vital job of pumping blood through the body in order to supply cells with oxygen and other nutrients. This is achieved through rhythmic contractions and relaxations of its four chambers, which are integrated in a closed-loop circulation. Four valves prevent the blood from flowing in the wrong direction. The left ventricle (LV) pumps oxygenated blood through the aortic valve to the entire body, where oxygen and other nutrients are released to the cells. The deoxygenated blood then returns through the caval veins to the right atrium (RA). From there, it flows through the tricuspid valve into the right ventricle (RV). The RV pumps the blood through the pulmonary valve to the lungs, where it is oxygenated again. It then returns through the pulmonary veins to the left atrium (LA) and finally through the mitral valve back into the LV. The heart itself is supplied via the coronary arteries, originating from the aortic root, and the coronary sinus, a vein draining into the RA [1, sec. 19.1]. The phase in which the ventricles contract is called systole and the phase in which they relax is called diastole. The atria contract at the end of (ventricular) diastole and relax at the beginning of (ventricular) systole. Together, systole and diastole represent a cardiac cycle [1, sec. 19.3].

The cardiac muscle tissue (myocardium) consists of elongated muscle cells (myocytes). Their orientation rotates across the cardiac wall and forms a swirling pattern around the heart that helps to pump blood efficiently. Apart from the myocardium, the cardiac wall consists of two more layers: the endocardium lines the inner surface and the epicardium covers the outer surface. The entire heart is enclosed in a membranous sac called pericardium [1, sec. 19.1].
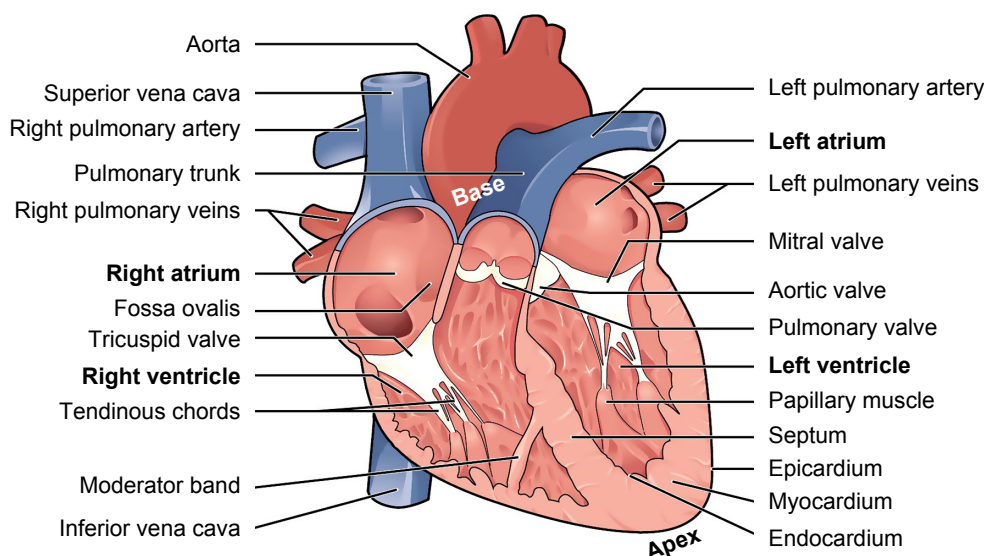
Figure 2.1: Anatomy of the human heart. Adapted from [1, sec. 19.1], licensed under CC BY 4.0.

2.1.2 Electrophysiology

The mechanical function of the heart is mediated by electrical activity. The myocytes are bounded by a membrane, which separates the interior of the cell (intracellular space) from the exterior (extracellular space). The cell membrane is made of phospholipids arranged in a bilayer containing pore-forming proteins (ion channels), which allow a controlled exchange of ions through the membrane. The distribution of ions between both sides of the membrane is determined by electrochemical gradients and leads to a difference between the intra- and the extracellular potential called transmembrane voltage (TMV). In the resting state, most ion channels are closed and the TMV is at about $-90\,\mathrm{mV}$. The cell is said to be polarized. When the cell is excited by increasing the TMV above a certain threshold, a sequence of changes in ion channel permeabilities starts. This results in a stereotypical TMV time course called action potential (Fig. 2.2). First, voltage-gated sodium channels open and an inrush of sodium ions leads to rapid depolarization. Then, the sodium channels close again and a maximum of about $30\,\mathrm{mV}$ is reached. During the plateau phase, the TMV decreases only slowy, because only few potassium channels are open and the outflow of potassium ions is compensated by an inflow of calcium ions. This calcium inflow stimulates the release of more calcium ions from the sarcoplasmatic reticulum, a reservoir within the cell. The increase in intracellular calcium leads to conformational changes of motor proteins responsible for the contraction of the cell. At a TMV of about $0\,\mathrm{mV}$, the calcium channels close and potassium channels open, allowing potassium ions to exit the cell more rapidly – the TMV decreases and the cell repolarizes. 200 to $400\,\mathrm{ms}$ after excitation, the TMV reaches the resting value again. Special membrane proteins (ion pumps) ensure that the original distribution of different ions is restored. Myocytes that are not fully repolarized either require a larger voltage to be excited (they are relatively refractory) or cannot be excited at all (they are absolute refractory).

Although the myocardium is composed of individual cells, it forms a functional syncytium: the cells are connected via gap junctions. When a cell is depolarized, the intercellular exchange of ions triggers neighboring cells to depolarize as well. This way, the excitation is conducted from cell to cell, leading to a wave-like spread of excitation [1, sec. 19.2].

During the normal heart rhythm (sinus rhythm), the excitation is initiated by special pacemaker cells within the sinoatrial node in the superior wall of the RA. From there, the excitation spreads across the atrial myocardium. The ventricles are electrically isolated from the atrial myocardium and get activated through a system of specialized pathways. This conduction system connects the sinoatrial node with the atrioventricular node between atria and ventricles. There, the excitation is delayed before being forwarded to the bundle of His. This bundle splits into a left and a right bundle branch running down the septum. The bundle branches ultimately split into the finer Purkinje fibers, which activate the ventricular myocardium from beneath the endocardium.
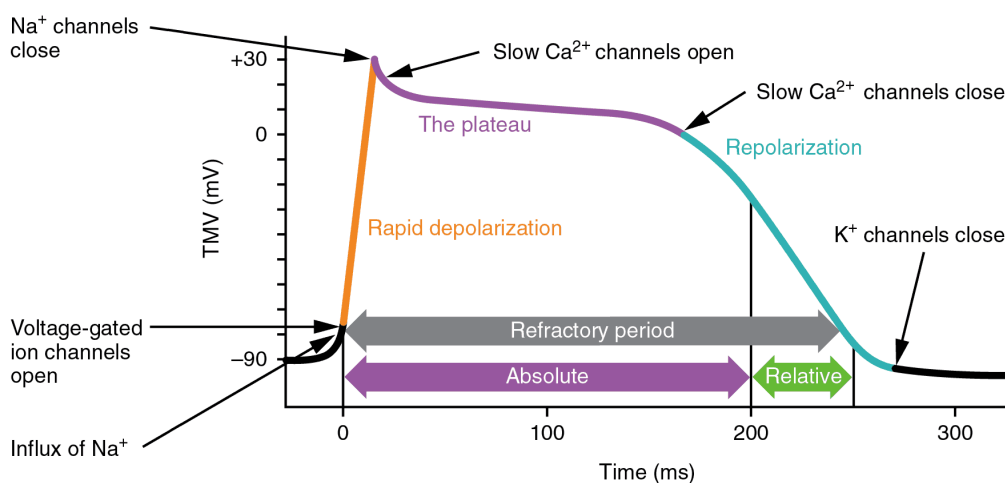
Figure 2.2: Action potential of a cardiac myocyte. Adapted from [1, sec. 19.2], licensed under CC BY 4.0.

2.2 Electrocardiography

The electrical activity of the heart gives rise to an electric field, whose potential differences can be measured on the body surface. In classical ECG, 9 electrodes are used for measurement: 3 limb electrodes (left and right arm and left foot) and 6 chest electrodes. These electrodes are used to derive 12 standard ECG leads: 6 limb leads (Einthoven I, II, III and Goldberger aVL, aVR, aVF) and 6 chest leads (Wilson V1 . . . V6). Although all leads are technically bipolar, the Goldberger and Wilson leads are called unipolar, because they are referenced to a potential that is relatively constant throughout the cardiac cycle and thus represent the potential variation at a single point [2].

Fig. 2.3 shows a normal ECG as it could be measured in lead II. The P wave corresponds
to the depolarization of the atria, the QRS complex to the depolarization of the ventricles and
the T wave to the repolarization of the ventricles. Due to the rapid activation of the ventricles
via the conduction system, the QRS complex is normally quite narrow (< 100 ms).

More comprehensive information compared to the 12-lead ECG can be obtained with
BSP mapping, which uses more electrodes – also covering the back of the torso [3]. For
example, the system used for the clinical recordings in this work allows up to 224 electrodes
that are distributed over 28 strips with 8 electrodes each. BSP mapping is usually preferred
for solving the inverse problem of ECG.
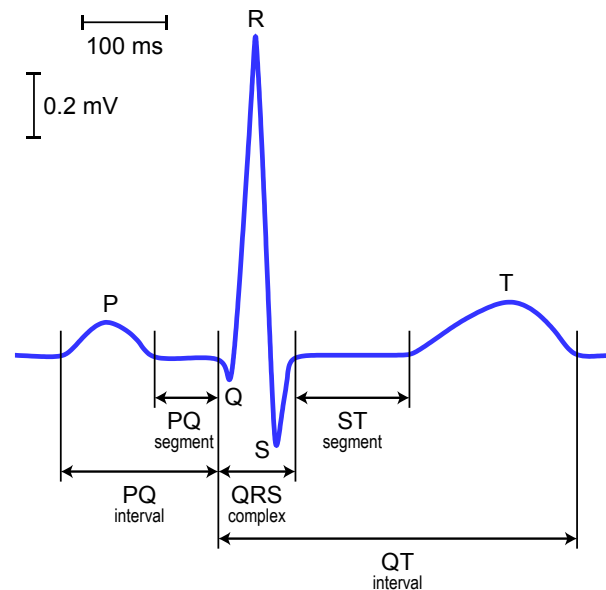
Figure 2.3: Normal ECG with annotations of waves, segments and intervals. Adapted from [4] with
permission.

2.3 Ectopic Beats, Ventricular Tachycardia and Cardiac Resynchronization Therapy

An ectopic beat, also known as premature contraction or extrasystole, is a heart beat originating
from outside the sinoatrial node. The corresponding excitation origin is called ectopic focus.
Ectopic beats are caused by spontaneously depolarizing cells or micro-reentries and can
be mimicked by pacing from an electrode on the endo- or epicardium. Most ectopic beats
are unproblematic, but in some patients, ventricular ectopic beats can develop into VT, in
particular if they happen very frequently.

VT is a type of fast, abnormal heart rhythm. In contrast to ventricular fibrillation, the electrical activity during VT is not yet completely disorganized and thus the ventricles maintain a certain level of pumping function. Short VT episodes may be unproblematic, but longer episodes are dangerous and have to be stopped by delivering an electric shock. Therefore, patients often receive an implanted cardioverter-defibrillator. In the ECG, most VTs present with wide QRS complexes (> 120 ms). If the morphology of the ECG changes from beat to beat, the VT is called monomorphic, otherwise polymorphic. Apart from ectopic foci, VTs can be caused by reentries or repolarization abnormalities. Monomorphic VTs are often scar-related, i.e. caused by non- or slow-conducting regions resulting from a heart attack and forming a reentry circuit. For these cases, a treatment option is to interrupt the reentry circuit by targeted inactivation of tissue using catheter ablation. This requires localization of the exit site of the VT, i.e. the site where the excitation wave exits the diseased myocardium and meets relatively normal myocardium. Non-invasive localization of the exit site could replace or at least shorten invasive catheter mapping procedures and thereby reduce the risk for complications.

Cardiac resynchronization therapy (CRT) is a treatment for other types of disorders, in which there is a difference in timing between the activities of both ventricles. This can occur if the excitation is blocked in one of the bundle branches. In CRT, a biventricular pacemaker with one electrode per ventricle is implanted. The RV electrode is anchored to the RV endocardium (usually in the apical region) and the LV electrode is placed epicardially within a left coronary vein. Isolated pacing from one of the electrodes provides a good scenario for validation of the ECG inverse problem, because the position of the implanted electrodes can be determined using computed tomography (CT).

Biophysical and Mathematical Fundamentals

3.1 Bioelectric Sources and Potentials

ECG is concerned with frequencies below 1 kHz. For these frequencies, the following properties of body tissues were found and can be used to describe the relation between bioelectric sources in the heart and the resulting potentials in the body [5, 6]:

- In regions without sources, the current density $\mathbf{J}$ is linearly related to the electric field $\mathbf{E}$ and capacitive effects are negligible (indicated by the strikethrough):

$$\mathbf{J} = (\sigma + j\omega\epsilon)\mathbf{E} \tag{3.1}$$

  Here, σ is the bulk conductivity tensor.

- Electromagnetic induction effects are negligible and thus the electric field can be obtained from the gradient of the scalar potential ϕ:

$$\mathbf{E} = -\nabla\phi - j\omega\mathbf{A} \tag{3.2}$$

Therefore, the relation between currents and potentials is quasi-static, i.e. can be assumed time-independent. Under quasi-static conditions, the continuity equation reduces to:

$$\nabla \cdot \mathbf{J} = -j\omega\rho = 0 \tag{3.3}$$

Bioelectric sources can be represented by an impressed current density $\mathbf{J}_s$, which extends (3.1) to:

$$\mathbf{J} = \sigma\mathbf{E} + \mathbf{J}_s \tag{3.4}$$

Combining (3.2), (3.3) and (3.4) yields the following Poisson-type equation:

$$\nabla \cdot (\sigma\nabla\phi) = \nabla \cdot \mathbf{J}_s \tag{3.5}$$

During ECG measurements, the body is surrounded by air. Hence, no current can leave the body and the following boundary condition applies to its surface S_B with the normal $\mathbf{n}$:

$$(\sigma\nabla\phi) \cdot \mathbf{n} = 0 \quad \text{on} \quad S_B \tag{3.6}$$

To uniquely determine ϕ, it is further necessary to fix its value at one point (or its linear combination at several points).

3.2 Bidomain Model

As mentioned in section 2.1.2, the myocardium forms a functional syncytium. This fact is utilized in the bidomain model [7, 8], which treats the intra- and extracellular spaces as two continuous domains connected via the cell membrane. Furthermore, it assumes that both domains coexist at every point in the myocardium. This is justified if we are not interested in the potential and current density around single cells but only in spatial averages over hundreds of cells [7]. Separate potentials ϕ_i and ϕ_e and conductivity tensors σ_i and σ_e are introduced for the intra- and extracellular domain, respectively. Due to conservation of charge, the current flowing out of one domain must flow into the other domain. Therefore, (3.5) is replaced by:

$$\nabla \cdot (\sigma_i \nabla \phi_i + \sigma_e \nabla \phi_e) = 0 \tag{3.7}$$

Using the TMV V_m to express $\phi_i = \phi_e + V_m$ yields:

$$\nabla \cdot ((\sigma_i + \sigma_e) \nabla \phi_e) = -\nabla \cdot (\sigma_i \nabla V_m) \tag{3.8}$$

Comparing (3.8) with (3.5), we see that within the myocardium, the bulk conductivity is given by $\sigma = \sigma_i + \sigma_e$ and the impressed current density is given by $\mathbf{J}_s = -\sigma_i \nabla V_m$.[1] BSPs are given by $\phi = \phi_e$ on the body surface.

3.3 Surface Sources

3.3.1 Transmembrane Voltages on the Myocardial Surface

In equation 3.8, the gradient of TMVs in the myocardial volume is the source of extracellular potentials (EPs). Yamashita and Geselowitz [10, 11] derived TMVs on only the myocardial surface as an equivalent source model, if the intra- and extracellular domains have equal anisotropy ratios, i.e. $\sigma_i = k\sigma_e$. The derivation goes as follows. As the volume conductor is linear, we can write the relation between V_m in the myocardium and ϕ on the body surface as:

---

[1]Scharf et al. [9] pointed out that in terms of first principles, the charge density is the source of the electric field and currents are a consequence. However, viewing the body as volume conductor with impressed currents as bioelectric sources is equivalent in terms of the fields produced. Furthermore, the bidomain model has proven to be extremely useful in describing the sources, because it allows to link the stereotypical electrical activity of myocytes (in the form of TMVs) with the macroscopic structure of myocardium (in the form of different, anisotropic intra- and extracellular conductivities).

$$\phi = -\int_{V_H} \sigma_i \nabla V_m \cdot \nabla Z \, dV \tag{3.9}$$

Here, V_H denotes the myocardial volume and ∇Z is the transfer impedance, also known as lead field, because it is equivalent to the electric field that results when a unit current is applied between an electrode and the reference terminal. Next, an "Ansatz" is made, so that the divergence theorem and the product rule for multiplication by the scalar V_m can be applied:

$$a := \int_{V_H} \nabla \cdot (\sigma_i V_m \nabla Z) \, dV \qquad \text{(Ansatz)} \tag{3.10}$$

$$a = \underbrace{\int_{S_H} \sigma_i V_m \nabla Z \cdot d\mathbf{S}'}_{b} \qquad \text{(Divergence theorem)} \tag{3.11}$$

$$a = \underbrace{\int_{V_H} V_m \nabla \cdot (\sigma_i \nabla Z) \, dV}_{c} + \underbrace{\int_{V_H} \sigma_i \nabla V_m \cdot \nabla Z \, dV}_{d} \qquad \text{(Product rule)} \tag{3.12}$$

Here, S_H is the myocardial surface with outward-pointing normals. We see that d is just the negative of ϕ in (3.9) and thus ϕ can be expressed as:

$$\phi = -d = -b + c \tag{3.13}$$

$$= -\int_{S_H} \sigma_i V_m \nabla Z \cdot d\mathbf{S}' + \int_{V_H} V_m \nabla \cdot (\sigma_i \nabla Z) \, dV \tag{3.14}$$

For equal anisotropy ratios, σ_i is proportional to $\sigma_i + \sigma_e$ and thus $\sigma_i \nabla Z$ in (3.14) has the same direction as $(\sigma_i + \sigma_e)\nabla Z$. Since $(\sigma_i + \sigma_e)\nabla Z$ is the lead field current, its divergence must vanish due to conservation of charge. Therefore, the volume integral in (3.14) becomes zero and ϕ only depends on V_m on the myocardial surface. For isotropic conductivities, the term $\sigma_i V_m$ represents the magnitude of a current dipole moment per unit area (unit A/m). Hence, the volumetric sources can be replaced by a dipole layer on the myocardial surface. This is also known as equivalent dipole layer (EDL) model [12]. Reducing the TMVs to values on the myocardial surface is useful for the inverse problem of ECG, because it facilitates the (theoretical) uniqueness of the solution [13].

3.3.2 Extracellular Potentials on a Surface Enclosing the Myocardium

Another surface representation of sources are the EPs ϕ themselves on a "heart" surface tightly enclosing the myocardium. As there are no actual sources outside such a surface, the right side of (3.5) becomes zero and BSPs are defined by a boundary value problem of Laplace's equation with Dirichlet boundary conditions on the heart surface. An advantage of this source representation is that it is independent from anything inside the heart surface, including myocardial anisotropy. A disadvantage is that the potentials are also influenced by

distant activity, although nearby activity can be expected to dominate. If the heart surface is the myocardial surface itself, the potentials will be called epi- and endocardial potentials (EEPs) in this work. If it is a hull around the heart (a capped version of the epicardial surface not including the endocardium), they will be referred to as pericardial potentials (PPs).

3.4 Solid Angle Analogy

In the case of an infinite and homogeneous volume conductor and isotropic conductivities σ_i and $\sigma = \sigma_i + \sigma_e$, the solution of equation 3.8 is [14, ch. 11]:

$$\phi_\infty(\mathbf{r}) = -\frac{\sigma_i}{4\pi\sigma} \int_{V_H} \nabla V_m \cdot \frac{\mathbf{r} - \mathbf{r}'}{|\mathbf{r} - \mathbf{r}'|^3} \, dV' = -\frac{\sigma_i}{4\pi\sigma} \int_{S_H} V_m \frac{\mathbf{r} - \mathbf{r}'}{|\mathbf{r} - \mathbf{r}'|^3} \cdot d\mathbf{S}' \qquad (3.15)$$

Here, $\mathbf{r}$ and $\mathbf{r}'$ are position vectors of field and source points, respectively. The expression

$$d\Omega = \frac{\mathbf{r} - \mathbf{r}'}{|\mathbf{r} - \mathbf{r}'|^3} \cdot d\mathbf{S}' \qquad (3.16)$$

represents the solid angle subtended at $\mathbf{r}$ by the infinitesimal surface element $d\mathbf{S}'$, i.e. the signed area resulting from projection of $d\mathbf{S}'$ onto a unit sphere centered at $\mathbf{r}$. Applying this geometric interpretation to (3.15) offers useful insights about the basic relation between surface TMVs and BSPs:

- BSPs are zero if TMVs are the same all over the heart (completely de- or completely repolarized), because the total solid angle spanned by the closed surface S_H is zero.
- BSPs are proportional to the negative solid angle spanned by the depolarized area enclosed by the wavefront (assuming TMVs are constant before and after depolarization).
- Shifting the depolarized area from one side of the myocardial wall to the other mainly leads to an inversion of BSPs, because $\mathbf{r}'$ stays approximately the same (assuming a thin wall), but the surface normals (and thus $d\mathbf{S}'$) point in the opposite direction.

Fig. 3.1 illustrates the relevant solid angles for a focal excitation originating from the LV endocardium (in an idealized model). Shown is a transversal slice through the torso. The two black line segments represent the depolarized areas on the epi- and endocardial surface. The corresponding solid angles with respect to two points on the body surface are depicted in red and blue. The potential at these points is proportional to the angle in blue minus the angle in red.
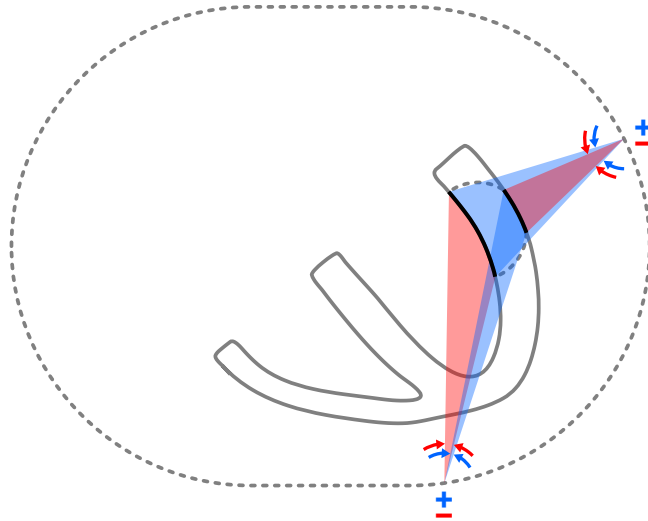
Figure 3.1: Illustration of solid angles (see text on the left).

3.5   Boundary Element Method

In the more general case of an inhomogeneous volume conductor with K boundary surfaces separating different compartments, the potential on a boundary surface l is given by [15]:

$$\phi_l(\mathbf{r}) = \frac{2\sigma}{\sigma_l^- + \sigma_l^+} \phi_\infty(\mathbf{r}) - \frac{1}{2\pi} \sum_{k=1}^{K} \frac{\sigma_k^- - \sigma_k^+}{\sigma_l^- + \sigma_l^+} \int_{S_k} \phi_k(\mathbf{r}') \, d\Omega \qquad (3.17)$$

Here, $\sigma_\bullet^-$ and $\sigma_\bullet^+$ are the conductivities inside and outside the surface denoted in the subscript and σ is the same as in (3.15). The primary sources are represented by the first term. The second term represents secondary sources at the interfaces between the compartments, which are caused by the field of the primary sources.

To calculate $\phi_l(\mathbf{r})$ with (3.17), the potentials $\phi_k(\mathbf{r})$ on the right need to be known for all surfaces. Therefore, corresponding equations for all surfaces ($l = 1, \dots, K$) are obtained and combined into a linear system of equations. Note that due to the sum in (3.17), this requires a total of K^2 iterations over the surfaces. To discretize the problem, the boundary surfaces are triangulated, basis functions over the triangles are introduced to express ϕ_l (and thus also ϕ_k) and V_m, and the sum of weighted residuals is set to zero. The entire process is known as boundary element method (BEM). The solution of the resulting system of equations is uniquely determined up to an additive constant (the zero level), which can be defined using a deflation technique [16]. Once the potentials on the surfaces are known, the potentials inside a surface l can also be obtained by evaluating the following equation [15]:

$$\phi_l^-(\mathbf{r}) = \frac{\sigma}{\sigma_l^-} \phi_\infty(\mathbf{r}) - \frac{1}{4\pi} \sum_{k=1}^{K} \frac{\sigma_k^- - \sigma_k^+}{\sigma_l^-} \int_{S_k} \phi_k(\mathbf{r}') \, d\Omega \qquad (3.18)$$

The main advantage of BEM is that it only requires meshing of the boundary surfaces instead of the entire volume, which reduces the complexity of model generation and avoids discretization errors within the volume. The main disadvantage compared to the finite element method is that it cannot account for anisotropic conductivities (at least not easily [17]) and that it leads to a dense system matrix, limiting the possible resolution of surfaces.

For details on BEM with EPs, see [18]. All transfer matrices in this work were computed with the BEM implementation by Stenroos et al. [15] with linear basis functions and point collocation weighting. Potyagaylo [19, sec. 3.3] extended this implementation for the use with TMVs.

3.6   Eikonal Equation and Fast Iterative Method

Detailed simulations of the spread of cardiac excitation can be performed with reaction-diffusion models, i.e. by coupling the bidomain or a simplified monodomain model with ordinary differential equations describing the dynamics of ionic currents through the cell membrane. Such models are required for simulating complex arrhythmias, where local

variations in cellular electrophysiology, source-sink mismatches and boundary effects play a role. For simpler activity like focal excitations, these effects may be neglected and a computationally less demanding model can be employed [20], which is based on the anisotropic eikonal equation:

$$\sqrt{(\nabla t_a)^\mathsf{T} \mathbf{D} (\nabla t_a)} = 1 \quad \text{with} \quad t_a(\mathbf{x}) = t_{init}(\mathbf{x}) \quad \forall \mathbf{x} \in \mathcal{B} \tag{3.19}$$

This equation describes the ATs t_a resulting from one or multiple wavefronts starting at the initial times t_{init} from the points in $\mathcal{B}$ and propagating with conduction velocities (CVs) encoded in the tensor $\mathbf{D}$. For transversely isotropic CVs and fiber orientations given by the angles θ and φ (ISO convention of spherical coordinates), $\mathbf{D}$ is given by:

$$\mathbf{D} = v^2 \, \mathbf{R} \begin{pmatrix} a^{-2} & 0 & 0 \\ 0 & a^{-2} & 0 \\ 0 & 0 & 1 \end{pmatrix} \mathbf{R}^\mathsf{T} \quad \text{with} \quad \mathbf{R} = \begin{pmatrix} \cos\varphi & -\sin\varphi & 0 \\ \sin\varphi & \cos\varphi & 0 \\ 0 & 0 & 1 \end{pmatrix} \begin{pmatrix} \cos\theta & 0 & \sin\theta \\ 0 & 1 & 0 \\ -\sin\theta & 0 & \cos\theta \end{pmatrix} \tag{3.20}$$

Here, v is the CV in longitudinal fiber direction and a is the anisotropy ratio leading to a CV of v/a in transversal direction. If $v = a = 1$, and $t_{init}(\mathbf{x}) = 0$ for a single point $\mathbf{x}$, then t_a is the geodesic distance to $\mathbf{x}$.

A highly parallelizable method for solving the eikonal equation is the fast iterative method (FIM) [21]. In this work, the GPU implementation of FIM for tetrahedral meshes by Fu et al.[2] has been extended for the needs of cardiac applications[3] and was used for simulations.

After solving the eikonal equation, an action potential template can be aligned with the ATs to obtain TMVs.

3.7   Rule-Based Ventricular Fiber Orientation

The fiber orientation needed for anisotropic excitation simulations can be assigned based on rules derived from histological or diffusion tensor imaging data. Streeter et al. [22] found that normal ventricular fibers show a helical structure and that the helix angle α, i.e. the angle with respect to the circumferential direction, changes continuously from about $-60°$ on the epicardum to about $+60°$ on the endocardium. In this work, the Laplace-Dirichlet rule-based (LDRB) algorithm [23] to generate fiber orientations for biventricular geometries was implemented[4]. Due to the way spherical linear interpolation is applied in the original algorithm, the resulting fibers rotate by the square-root of the transmural Laplace solution and – depending on the input angles – may exhibit a discontinuity in the free walls. Therefore, the original algorithm was slightly adapted to yield a linear transmural rotation and to circumvent the discontinuity in the free walls. For more details, see the GitHub repository. Fig. 3.2 shows the fiber orientation resulting from the adapted algorithm.

---

[2]https://github.com/SCIInstitute/SCI-Solver_Eikonal
[3]https://github.com/KIT-IBT/FIM_Eikonal
[4]https://github.com/KIT-IBT/LDRB_Fibers

−60° ▬▬▬ +60°
Helix angle α
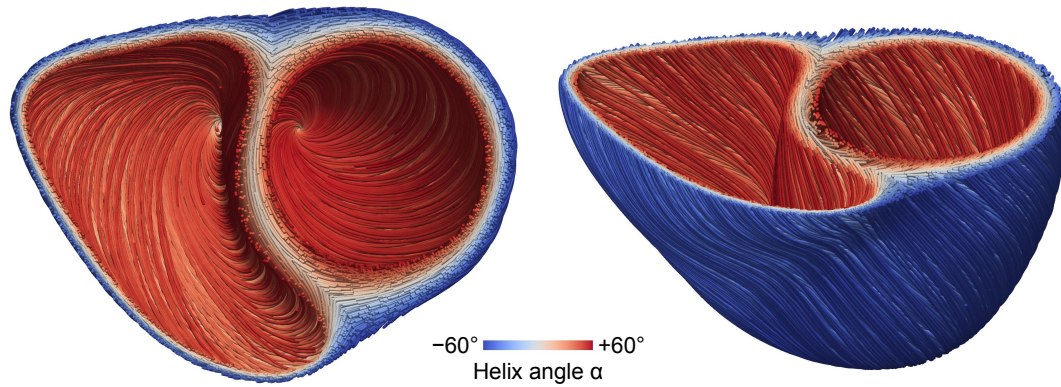
Figure 3.2: Streamlined fiber orientation computed with the adapted LDRB algorithm.

3.8 Discrete Laplacians

Discrete Laplace operators or Laplacians are useful for a variety of applications like data smoothing, interpolation or simply as a measure of smoothness. In Euclidean space, the Laplacian of a scalar function f is defined as the divergence of its gradient:

$$\Delta f = \nabla \cdot \nabla f \tag{3.21}$$

Based on [24, ch. 2], Laplacians for tetrahedral and triangle meshes can be derived as follows. Green's first identity states that:

$$\int_U f\Delta f + \nabla f \cdot \nabla f \ dV = \int_{\partial U} f\nabla f \cdot d\mathbf{S} \tag{3.22}$$

Assuming that the normal derivative of f is zero at the boundary ∂U of the domain U, the term on the right becomes zero and thus we have:

$$\int_U f\Delta f \ dV = -\int_U \nabla f \cdot \nabla f \ dV \tag{3.23}$$

For a tetrahedralized domain, this equation can be written in matrix form as:

$$\mathbf{f}^\mathsf{T}\mathbf{C}\mathbf{f} = -(\mathbf{G}\mathbf{f})^\mathsf{T}\mathbf{T}(\mathbf{G}\mathbf{f}) = -\mathbf{f}^\mathsf{T}\mathbf{G}^\mathsf{T}\mathbf{T}\mathbf{G}\mathbf{f} \tag{3.24}$$

Here, $\mathbf{f}$ contains values of f at the vertices, $\mathbf{G}$ is a sparse gradient matrix taking vertex values to tetrahedron values and $\mathbf{T}$ is a diagonal matrix containing the volumes of tetrahedrons. The entries of $\mathbf{G}$ represent the constant gradients of linear basis functions defined over the tetrahedrons. We see that the Laplacian is given by:

$$\mathbf{C} = -\mathbf{G}^\mathsf{T}\mathbf{T}\mathbf{G} \tag{3.25}$$

This matrix is also called the cotangent Laplacian [25, sec. 2.1.2]. $\mathbf{C}$ produces values integrated over the volume represented by each vertex. To get a Laplacian that produces point-wise values, we need to divide by the respective vertex volume:

$$\mathbf{L} = \mathbf{M}^{-1}\mathbf{C} \qquad (3.26)$$

Here, $\mathbf{M}$ is a diagonal mass matrix (barycentric or Voronoi) [25, sec. 2.1.3].
Laplacians for triangle meshes can be obtained in the same way (with triangle and vertex areas replacing tetrahedron and vertex volumes). The computation of gradient and Laplace operators is implemented in the gptoolbox by Jacobson [26]. In this work, the Voronoi mass matrix was used for $\mathbf{L}$.

3.9   Singular Value Decomposition

The singular value decomposition (SVD) factorizes any real matrix $\mathbf{M} \in \mathbb{R}^{M \times N}$ into a product of three matrices:

$$\mathbf{M} = \mathbf{U}\mathbf{S}\mathbf{V}^\mathsf{T} \qquad (3.27)$$

$\mathbf{U} \in \mathbb{R}^{M \times M}$ and $\mathbf{V} \in \mathbb{R}^{N \times N}$ are orthogonal matrices and $\mathbf{S} \in \mathbb{R}^{M \times N}$ is a diagonal matrix. The columns $\mathbf{u}_i$ of $\mathbf{U}$ are called left singular vectors, the columns $\mathbf{v}_i$ of $\mathbf{V}$ right singular vectors and the diagonal entries σ_i of $\mathbf{S}$ singular values. They satisfy the equations:

$$\mathbf{M}\mathbf{v}_i = \sigma_i\mathbf{u}_i \quad \text{and} \quad \mathbf{M}^\mathsf{T}\mathbf{u}_i = \sigma_i\mathbf{v}_i\,, \qquad i = 1, 2, \ldots, \min(M, N) \qquad (3.28)$$

Therefore, the SVD can be seen as solution to a generalized eigenvalue problem for non-square matrices: Application of $\mathbf{M}$ to the right singular vectors just yields a scaled version of the left singular vectors (and vice versa for $\mathbf{M}^\mathsf{T}$). Usually – and in this thesis –, the singular vectors are ordered such that the corresponding singular values are non-increasing over the index i.

The SVD has many practical applications. It can be used to analyze a matrix: "What are the basic components spanning and linking the row and column spaces and how strong is the relation between corresponding components?". It can also be used to "boil down" the information contained within a matrix, i.e. to obtain an approximation of the original matrix with reduced rank k. For that purpose, the SVD is truncated, which means that singular vectors and values for $i > k$ are discarded. The resulting matrix is the best rank-k approximation in terms of a minimal Frobenius norm of the difference with the original matrix (Eckart–Young theorem) [27, sec. 2.4].

Inverse Problem of Electrocardiography

Forward problems consist in finding the effect given the cause of a phenomenon. These kind of problems are usually well-posed, meaning there exists a unique solution that depends continuously on the input data [28]. Going the opposite way, i.e. finding the cause given the effect, is known as inverse problem. Inverse problems are particularly challenging, because in contrast to forward problems, they are usually ill-posed: there may be many solutions fitting to the observed effects and small pertubations in the input data or the model may lead to large changes in the solution. In order to obtain *meaningful* and *stable* solutions, one has to include additional information – a process called regularization. The main motivation to tackle inverse problems is usually to infer information that is not amenable to direct measurements without destroying or invading the object of interest.

In the inverse problem of ECG, one tries to infer diagnostically relevant information about the cardiac electrical activity from non-invasive measurements of BSPs [29]. It can be formulated in terms of physical sources of the electrostatic problem, activation times or even only the position of the excitation origin. In this thesis, "inverse problem of ECG" will be used as a general term that may refer to any of these formulations. "ECGI" will be used specifically for the linear inverse problem of reconstructing spatial distributions of physical sources. ECGI consists of finding meaningful solutions $\mathbf{x}$ to:

$$\mathbf{A}\mathbf{x}(t) = \mathbf{b}(t) \tag{4.1}$$

The transfer matrix $\mathbf{A}$ links the TMVs or EPs $\mathbf{x}(t)$ at a time t with the BSPs $\mathbf{b}(t)$ at the same time. Assuming a negligible deformation of the heart during the period of interest, $\mathbf{A}$ is time-independent. The ill-posedness of ECGI is largely due to the spatial blurring effect of the volume conductor. With increasing distance to the heart, the currents caused by the cardiac sources become more and more distributed in space and the corresponding potentials become blurred. Therefore, low spatial frequencies in the source distribution are transferred strongly to the body surface, while high spatial frequencies are attenuated. Consequently, the inverse problem involves an amplification of high spatial frequencies. Mathematically, the attenuation of high spatial frequencies in the forward problem is reflected in the SVD of $\mathbf{A}$ as visualized in Fig. 4.1 for both TMVs and EEPs.
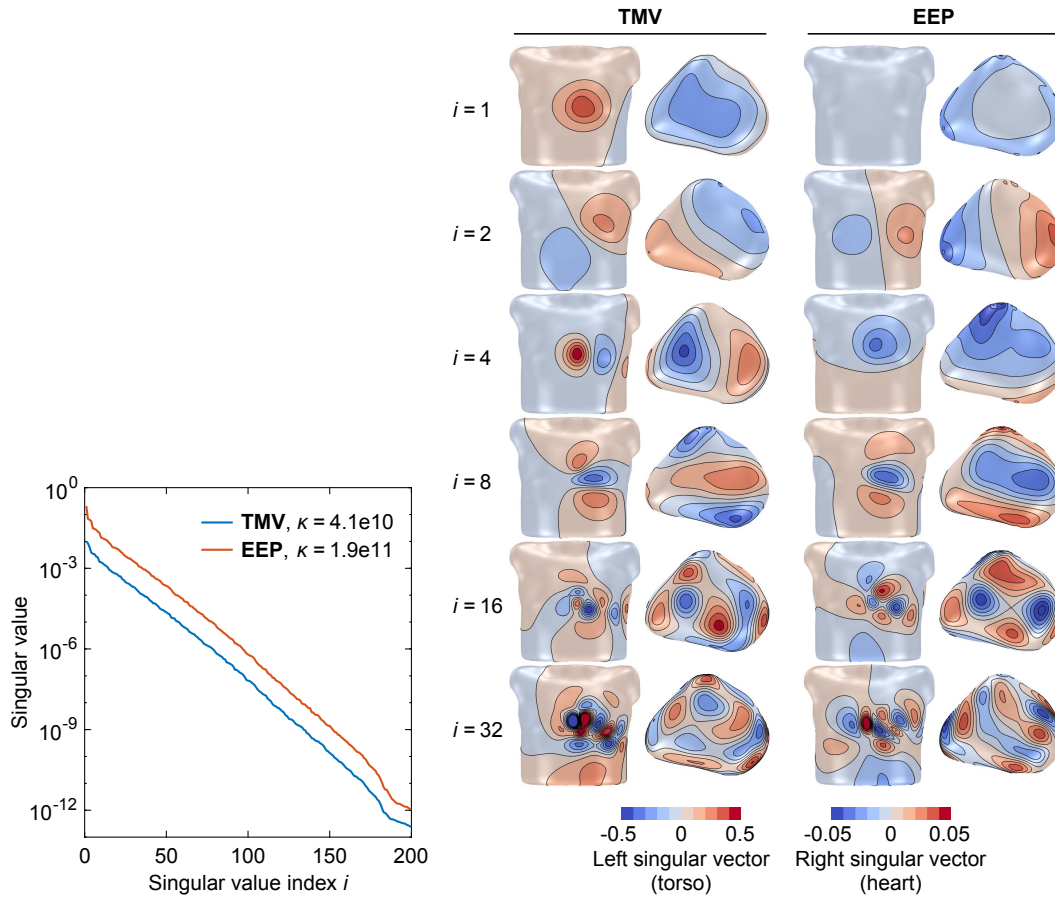
Figure 4.1: Visualization of the SVD of the transfer matrix for TMVs and EEPs (homogeneous torso with 200 electrodes). *Left:* Decay of singular values over the singular value index i. The condition number κ is given in the legend. *Right:* The spatial frequency of corresponding singular vectors increases with i.

The diagram on the left reveals that the sorted singular values show an approximately exponential decay (note the logarithmic ordinate). The corresponding left and right singular vectors are depicted on the right. It can be seen that the number of sign changes tends to increase with the singular value index i. The ratio of the largest and smallest singular value is called condition number and expresses how much the solution **x** will change with respect to a change in **b** (assuming no regularization). If the condition number is large, a small error in **b** can lead to a large error in **x**, because the multiplication with a (relatively) small singular value in the forward problem corresponds to a multiplication with its large reciprocal in the inverse problem. ECGI is severely ill-conditioned. A straightforward approach to stabilize the least-squares solution of (4.1) is to reduce the condition number of **A** by discarding singular vectors corresponding to small singular values, i.e. to replace **A** by its truncated SVD. This leads to a "hard" suppression of low singular value components in the solution and represents one possible method of regularization. Tikhonov regularization – another classical method – is characterized by a more gradual filtering effect (see [30, ch. 4] for a filter factor analysis).

4.1 Tikhonov Regularization

Tikhonov regularization [31] is a form of regularized least squares in which the regularization term is given by a sum of squared values. It minimizes the weighted sum of a squared residual norm and a squared solution norm. The residual norm represents the misfit between predicted and measured BSPs and the solution norm enforces some form of regularity or "desired" properties on the solution. The factor λ weighting the squared solution norm is called regularization parameter. Purely spatial Tikhonov regularization treats every time step independently:

$$\widehat{\mathbf{x}} = \arg\min_{\mathbf{x}} \Big(\underbrace{\|\mathbf{Ax} - \mathbf{b}\|_2^2}_{\substack{\text{squared} \\ \text{residual} \\ \text{norm}}} + \lambda(t) \underbrace{\|\mathbf{Rx}\|_2^2}_{\substack{\text{squared} \\ \text{solution} \\ \text{norm}}} \Big) \tag{4.2}$$

$\mathbf{A} \in \mathbb{R}^{M \times N}$ is the transfer matrix and $\mathbf{R} \in \mathbb{R}^{Q \times N}$ is a spatial regularization operator. $\mathbf{b} \in \mathbb{R}^{M \times 1}$ are the BSPs and $\mathbf{x} \in \mathbb{R}^{N \times 1}$ the cardiac sources at a single time step t. M is the number of electrodes and N the number of cardiac nodes. Q is usually (but not necessarily) equal to N. Equation 4.2 has the closed-form solution:

$$\widehat{\mathbf{x}} = (\mathbf{A}^\mathsf{T}\mathbf{A} + \lambda\,\mathbf{R}^\mathsf{T}\mathbf{R})^{-1}\mathbf{A}^\mathsf{T}\mathbf{b} \tag{4.3}$$

To speed up the computation for multiple values of λ, the generalized singular value decomposition (GSVD) of the matrix pair $(\mathbf{A}, \mathbf{R})$ can be utilized:

$$\mathbf{A} = \mathbf{USW}^\mathsf{T}, \quad \mathbf{R} = \mathbf{VMW}^\mathsf{T} \quad \text{with} \quad \mathbf{S}^\mathsf{T}\mathbf{S} + \mathbf{M}^\mathsf{T}\mathbf{M} = \mathbf{I} \tag{4.4}$$

Substituting (4.4) in (4.3) and using $\mathbf{U}^\mathsf{T}\mathbf{U} = \mathbf{V}^\mathsf{T}\mathbf{V} = \mathbf{I}$ yields:

$$\widehat{\mathbf{x}} = (\mathbf{W}^\mathsf{T})^{-1}(\mathbf{S}^\mathsf{T}\mathbf{S} + \lambda\,\mathbf{M}^\mathsf{T}\mathbf{M})^{-1}\mathbf{S}^\mathsf{T}\mathbf{U}^\mathsf{T}\mathbf{B} \tag{4.5}$$

The advantage of this formulation is that the GSVD and the inverse of $\mathbf{W}^\mathsf{T}$ can be precomputed and only the diagonal matrix $\mathbf{S}^\mathsf{T}\mathbf{S} + \lambda\,\mathbf{M}^\mathsf{T}\mathbf{M}$ has to be inverted for each new λ.

The solution of (4.2) is uniquely determined only if the nullspaces of $\mathbf{A}$ and $\mathbf{R}$ do not overlap. Depending on whether $\mathbf{R}$ is the identity matrix, a gradient operator or a Laplacian, one speaks of zero-, first- or second-order Tikhonov regularization, respectively. For a comparison of these three variants (and further spatial regularization methods) applied to the reconstruction of PPs, see [32].

4.2 L-curve Criterion

The choice of λ should result in an adequate trade-off between the data misfit and the regularity of the solution. A certain amount of misfit has to be tolerated due to imperfections in $\mathbf{b}$ (measurement errors) or $\mathbf{A}$ (modeling assumptions and errors in geometries and conductivities). The trade-off can be observed in a log-log plot of the solution norm over

the residual norm as a function of λ (Fig. 4.2). Due to its characteristic shape, this plot is called L-curve [33]. A heuristic approach for selecting λ is to locate the point on the L-curve with maximum curvature. Although this "L-curve criterion" is heuristic, it is not completely arbitrary and its properties have been studied extensively [33]. Using the log-log scale makes the shape of the L-curve (not the corresponding λs) independent of scalings of the two norms and thus independent of the choice of physical units. Using the curvature ensures that the identification of λ only depends on the shape of the L-curve (and not on shifts). For a comparison with other parameter choice techniques, see [34, 35].

The left half of Fig. 4.2 shows L-curves for a perfect matrix **A** and BSPs corrupted with five different levels of additive white Gaussian noise (WGN). It can be seen that with decreasing signal-to-noise ratio (SNR), the λ at the point of maximum curvature increases and the "corner" of the L-curve becomes less well defined. This effect becomes even more pronounced for an imperfect matrix **A** (right half of Fig. 4.2). Here, an inhomogeneous torso model (cavitary blood, lungs, liver) was used for forward calculations, but a homogeneous model was assumed for the inverse problem. This discrepancy in models reduces the sharpness of the L-curve corner, particularly for high SNRs, where it dominates the effect of BSP noise.
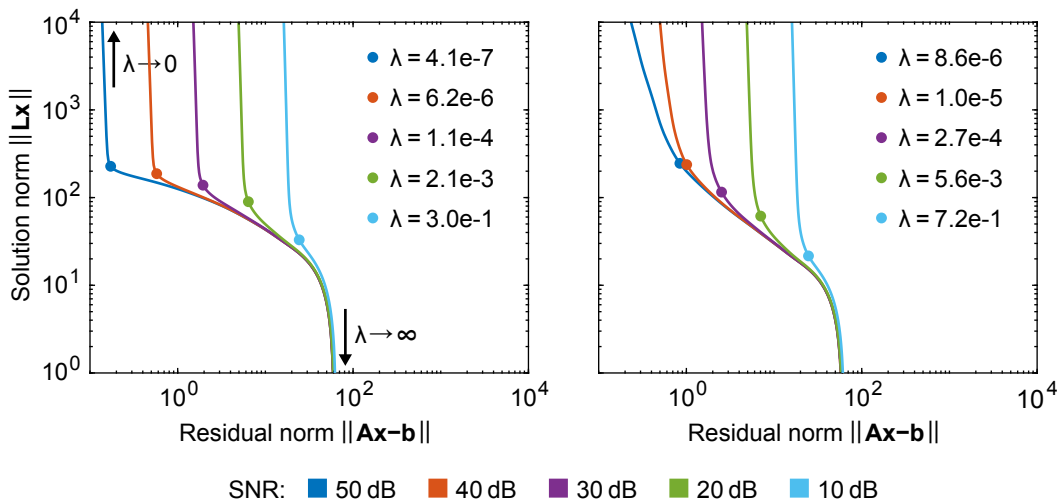
Figure 4.2: L-curves for second-order Tikhonov regularization of TMVs. 5 different SNRs are shown (WGN added to BSPs). *Left:* Perfect transfer matrix. *Right:* Imperfect transfer matrix (forward: inhomogeneous torso, inverse: homogeneous torso).

GENERAL TOOLS AND ANALYSES

Before proceeding with solving the inverse problem, a few general tools will be introduced, which are useful for processing and visualization of cardiac data. Furthermore, the main ingredients of second-order Tikhonov regularization and related methods shall be analyzed: variants of the transfer matrix $\mathbf{A}$ and the Laplacian $\mathbf{L}$ used as regularization operator. This will provide useful insights for regularization and interpretation of inverse solutions.

Consistent Biventricular Coordinates

Ventricular coordinates provide a parameterized description of local position within the ventricles and are a versatile tool for various applications in which such a description is convenient. In this work, the main motivation to use ventricular coordinates was to formulate the localization of ventricular excitation origins from the ECG as a regression task – directly yielding a patient-independent description of ventricular position (see section 10.3). To this end, we first reimplemented the Universal Ventricular Coordinates (UVC) proposed in [36]. This biventricular coordinate system defines a transventricular, a transmural, a rotational and an apicobasal coordinate. Although a great idea in general, we noticed that this coordinate system has some undesirable properties (at least for our purpose):

- There are discontinuities of the rotational and transmural coordinates at the junctions between both ventricles and the range of the rotational coordinate is different in both ventricles (leading to a hole in the space of normalized coordinates). This can be problematic particularly for regression applications.

- The coordinate values are based on solutions to Laplace's equation. However, Laplace solutions are not an accurate measure of normalized distance between two boundaries, because their linearity depends on the cross-sectional area of the region between both boundaries. This impairs the consistency of the coordinates across different geometries.

- The rotational coordinate has a singularity at the apex of each ventricle, which requires the apicobasal coordinate to become zero at exactly these singularities. This is not guaranteed by the construction of boundary conditions and in practice leads to ambiguities of the coordinates in the apical region.

To overcome these limitations, we developed a new coordinate system called Consistent Biventricular Coordinates (Cobiveco), which has been published in [37]. For a detailed description of the methodology and an extensive evaluation of Cobiveco, the reader is referred to the article. Here, only the core ideas and results shall be reported.

Fig. 5.1 shows the different concepts for the coordinate directions in the UVC system and Cobiveco. In Cobiveco, the transventricular boundary has been moved to the center of the septum to make the coordinates entirely symmetric in both ventricles. All coordinates are normalized to range between 0 and 1. The rotational coordinate is counter-rotating in both ventricles and unifies in the septum. It lies between 0 and $\frac{2}{3}$ in the free walls and between $\frac{2}{3}$ and 1 in the septum.
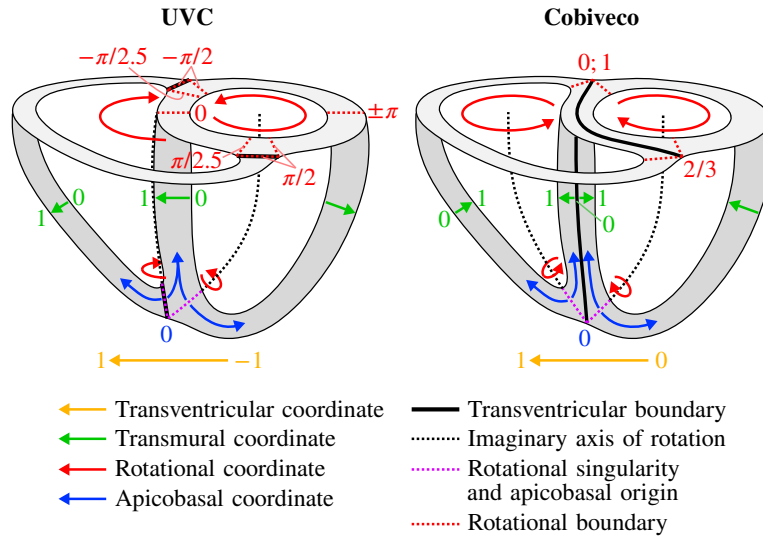
Figure 5.1: Different underlying concepts for coordinate directions and boundary values within the UVC (*left*) and the new coordinate system Cobiveco (*right*). Reproduced from [37] with permission.

To obtain the actual coordinate values, an efficient way to compute normalized distances (0...1) between two boundaries had to be found. While solutions to Laplace's equation with boundary values 0 and 1 are automatically normalized, they may change non-linearly in space – particularly when the wall thickness of the ventricles is not uniform. Solutions to the eikonal equation, on the other hand, are linear in space but represent non-normalized distances with respect to a single boundary. Eikonal solutions computed with respect to each of two boundaries represent distances along different, non-bijective trajectories, which makes it impossible to normalize one of the two solutions by dividing it by the sum of both solutions. An elegant way to obtain normalized distances along bijective trajectories is the approach originally suggested for a symmetric measure of wall thickness in [38]. A comparison showed that this "trajectory distance" approach is superior to Laplace's, the eikonal or Poisson's equation for computing coordinates and was chosen for Cobiveco. For each coordinate, it requires to solve a linear partial differential equation twice. Another novelty of Cobiveco compared to UVC is the use of implicit domain remeshing [39] for precise definiton of internal boundaries required to compute the coordinates. The new definition of boundaries also guarantees that the apicobasal coordinate is zero at the singularities of the rotational coordinate. For regression or data transfer purposes, the remaining discontinuity of the rotational coordinate r at $0 = 1$ is circumvented by transformation into two fully continuous rotational sine and cosine coordinates: $r_{\sin} = \sin(2\pi r)$ and $r_{\cos} = \cos(2\pi r)$.

Fig. 5.2 provides a visual comparison of Cobiveco and UVC for the mean shape of a statistical shape model (SSM) [40, 41] and a patient geometry. As the mean shape has a very uniform wall thickness, the contour lines of the rotational (r) and apicobasal (a) coordinates appear equidistant for both methods, but artifacts at discontinuities of the rotational coordinate can be seen for UVC (green circles). On the patient geometry, the differences are more pronounced. While the coordinates computed using Cobiveco still change very uniformly in space, there are substantial distortions in the UVC coordinates. The length of the segments between contour lines of the rotational coordinate changes up to four-fold between regions of small and large wall thickness. The apicobasal coordinate is also distributed very non-uniformly. Taking a closer look at the transmural coordinate (m) within the LV shows that it changes much faster at the endocardium than it does at the epicardium. If the coordinates always showed the same distortions for every geometry, this would only be a minor problem. However, comparing the rotational and apicobasal UVC coordinates for the patient geometry and the mean shape reveals that the same coordinate values can represent quite different anatomical regions (yellow stars). In contrast, the coordinates obtained using Cobiveco are consistent across the geometries (green stars).
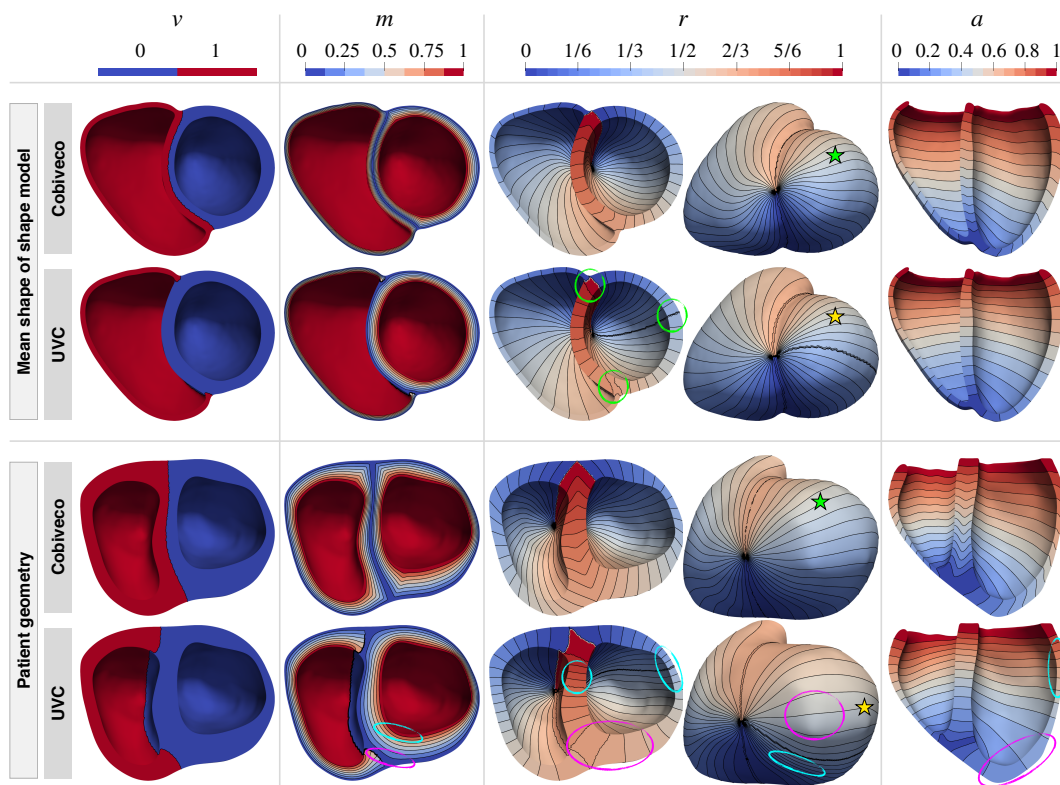
Figure 5.2: Coordinates computed using Cobiveco and UVC on two exemplary geometries. v, m, r, a: Transventricular, transmural, rotational and apicopbasal coordinate, respectively. The UVC coordinates were shifted and scaled to the same ranges as the Cobiveco coordinates to allow a direct comparison. Green circles mark artifacts at discontinuities of r for UVC. Magenta and cyan circles mark regions of stretched and compressed coordinate values, respectively. Green and yellow stars mark an exemplary point $(v, m, r, a) = (0, 0, \frac{7}{15}, \frac{1}{3})$ for Cobiveco and UVC, respectively. Adapted from [37] with permission.

A quantitative evaluation of Cobiveco was performed by computing transfer errors for 36 patient geometries. Two different types of transfer errors were considered. For the "two-way error", the ventricular coordinates were used to transfer the Euclidean coordinates from the shape model geometry to the patient geometry and then back again to the shape model geometry. The Euclidean distance between the original and the transferred Euclidean coordinates was then computed on the shape model geometry. The two-way error only reflects errors due to non-bijectivity or interpolation. To capture errors due to inconsistencies in the ventricular coordinates across different geometries, one has to transfer only in one direction, i.e., from the shape model geometry to the patient geometry, and then compute the deviation to the ground truth on the patient geometry. However, no real ground truth is available, because no error-free reference method exists to determine the anatomical point correspondences between both hearts. To overcome this problem, we used the ventricular coordinates themselves to create a synthetic "mean heart geometry" for which the ground truth is known by construction (see [37] for more details). The resulting "one-way error" therefore reflects the self-consistency of the ventricular coordinates. Both transfer errors were computed in both directions, i.e. the shape model geometry and the patient geometry were interchanged. Fig. 5.3 shows histograms of the resulting two- and one-way errors for both Cobiveco and UVC. For both types of errors, the mean could be reduced compared to UVC. Particularly the one-way error – which is most relevant in practice – improved substantially: from 7.15 to 1.51 mm (mean) and from about 24 to 6 mm (99th percentile). The spatial distribution of the mean transfer errors across all 36 geometries is depicted in Fig. 5.4. The largest reduction in two-way errors can be seen near the apex (singularities of the rotational coordinate) and at the transventricular junctions. The one-way errors reduced throughout the ventricles. The largest one-way errors for Cobiveco occur at the RV outflow tract.
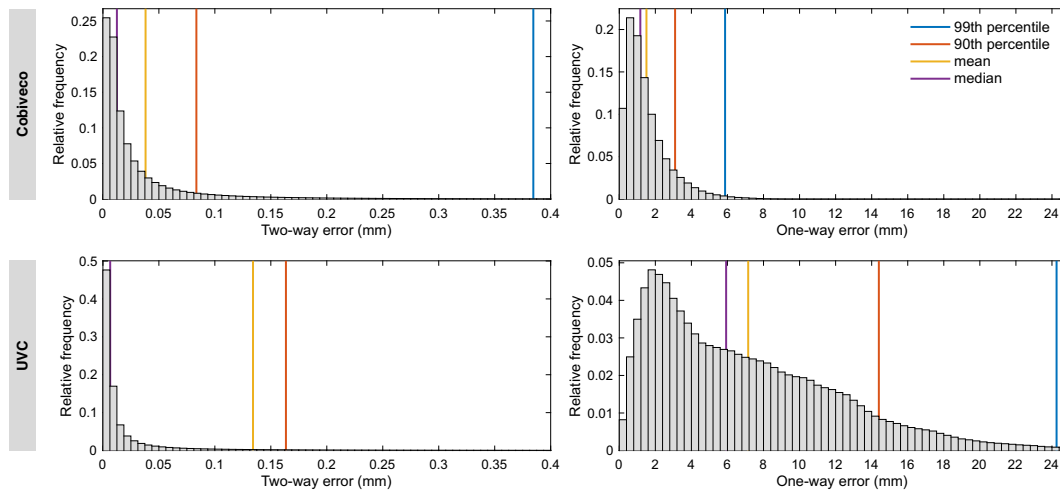
Figure 5.3: Average histograms of two-way errors (*left*) and one-way errors (*right*) evaluated for Cobiveco (*top*) and UVC (*bottom*). Histograms were averaged across all 36 patients and, for both types of errors, include both possible transfer directions. Each histogram contains about 50 M data points. Adapted from [37] with permission.
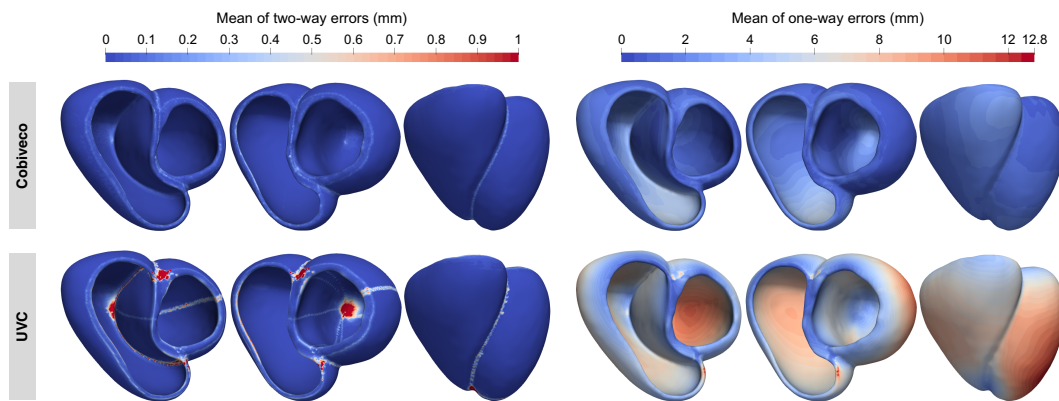
Figure 5.4: Spatial distribution of the mean transfer errors across all patients visualized on the mean shape of the SSM. As a common geometry is needed to average errors across patients, only transfer sequences with respect to the mean shape of the SSM are included here. Reproduced from [37] with permission.

Apart from regression-based localization of excitation origins, Cobiveco was also used to transfer activation times recorded using intracardiac mapping to the tomography-derived geometries used for ECGI (see section 14.1). Furthermore, Cobiveco was used to obtain polar projections of the epi- and endocardial surfaces, which allow a compact visualization without occlusions. Fig. 3 illustrates the correspondences between the 3D surfaces and the polar projections. An open-source MATLAB implementation of Cobiveco is provided[1].
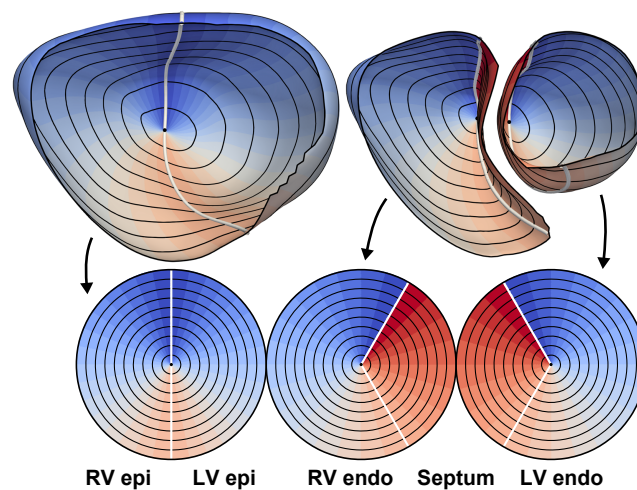
Figure 5.5: Rotational coordinate (colors) and apicobasal coordinate (black contours) used for polar projections of the epi- and endocardial surfaces. Reproduced from [42] with permission.

[1]https://github.com/KIT-IBT/Cobiveco

Analysis of Transfer Coefficients for Different Surface Sources

To understand the different properties of TMVs and EEPs as surface sources for ECGI, it is interesting to study their transfer coefficients stored in the respective transfer matrix $\mathbf{A} \in \mathbb{R}^{M \times N}$. Two questions are particularly interesting. First, how strong are sources in different regions of the heart surface transferred to the body surface? Sources that are transferred weakly will be hard to reconstruct. Second, how unique is the pattern of BSPs corresponding to a certain source point? Sources leading to similar BSPs will be hard to distinguish in the inverse problem.

To answer the first question, we can compute the length of the M-dimensional vector representing the BSP pattern corresponding to a node of the heart surface. Doing this for all nodes is the same as taking the column norm $\| \cdot \|_{\mathrm{col}}$ of the transfer matrix:

$$\mathbf{s} = \|\widetilde{\mathbf{A}}\|_{\mathrm{col}}^{\mathsf{T}} \qquad \text{with} \qquad \widetilde{\mathbf{A}} = \mathbf{A}\,\mathbf{M}^{-1} \tag{6.1}$$

Here, $\mathbf{M}$ is the mass matrix and $\widetilde{\mathbf{A}}$ is the mass-normalized transfer matrix. In contrast to $\mathbf{A}$, it contains point-wise values that are independent of the size of the surface area represented by a discrete node. $\mathbf{s} \in \mathbb{R}^{N \times 1}$ will be called "transfer strength" and can be visualized on the heart surface[1]. Fig. 6.1 shows polar projections of the transfer strengths for TMVs and EEPs and four variants of the torso model depicted in Fig. 6.1. The transfer strengths were normalized to their mean on the epicardium.

Concentrating on the case of TMVs and a homogeneous torso first (top-left of Fig. 6.1), we can see that the transfer strength depends strongly on the distance to the electrodes (compare with first row of Fig. 6.3). The transfer strength is largest at the anterior part of the RV lateral wall and smallest at the posterior side of the ventricles. Adding cavitary blood with a higher conductivity than the rest of the torso (second row of Fig. 6.1) increases the transfer strength on the endocardium. This is a consequence of the Brody effect [44, 45]. Adding furthermore lungs (third row of Fig. 6.1) decreases the transfer strength in their

---

[1]Transfer strength maps are similar to the contribution maps in [43], but instead of the contribution to a single electrode, they show the strength by which a point on the heart contributes to all electrodes.
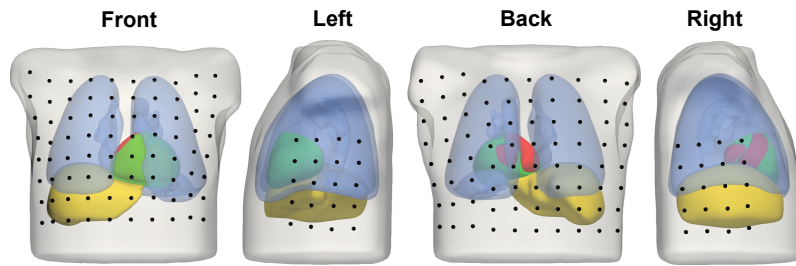
Figure 6.1: Torso model. *Green:* Ventricular myocardium (bulk conductivity: 0.2 S/m, intracellular conductivity: 0.05 S/m). *Red:* Cavitary blood (0.6 S/m). *Blue:* Lungs (0.04 S/m). *Yellow:* Liver (0.4 S/m). *Gray:* Rest of the torso (0.2 S/m). *Black dots:* 200 electrodes. Reproduced from [42] with permission.
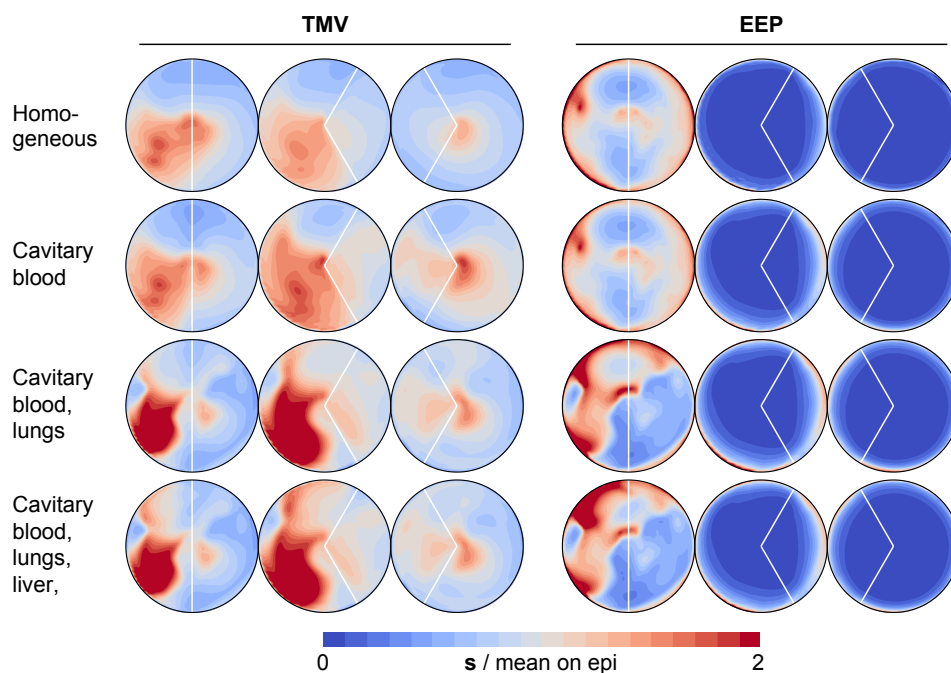
Figure 6.2: Transfer strength maps for TMVs and EEPs and four different torso models. The transfer strength **s** was normalized to its mean on the epicardium. See Fig. 5.5 for an explanation of the polar projections.

vicinity and increases the transfer strength in the remaining regions (compare with second row of Fig. 6.3). In particular, the transfer strength is increased at the anterolateral wall of the RV, because the low conductivity of the lungs forces the currents to flow preferentially within the gap between the two lungs. Lungs therefore exacerbate the non-uniformity of the transfer strength. As last compartment considered here, the liver with a conductivity between that of blood and the rest of the torso was added (last row of Fig. 6.1). This only has a minor effect: the transfer strength increases at the posterior side of the RV (compare with last row of Fig. 6.3).
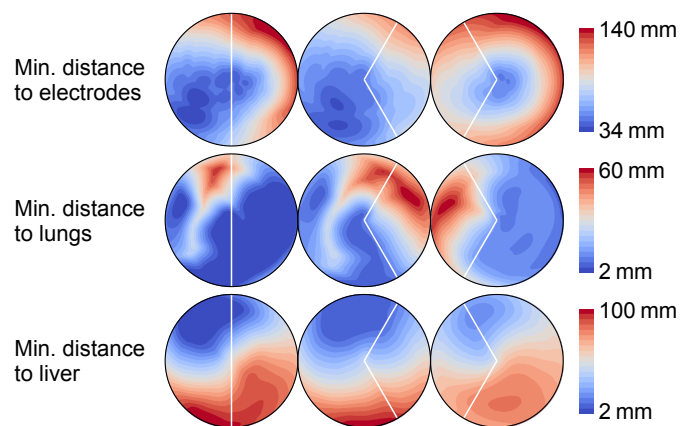
Figure 6.3: Minimal Euclidean distances from the points on the heart to the electrodes, lungs and the liver, respectively.

For EEPs and a homogeneous torso (top-right of Fig. 6.1), the main factor determining the transfer strength is the local convexity of the heart surface rather than the distance to the electrodes. Outwards curved regions like the rims around the orifices at the base and the apical epicardium show a large transfer strength, while inwards curved regions like the anterior and posterior parts of the epicardium between the two ventricles show a small transfer strength. This convexity-dependence of the transfer strength for EEPs is related to the fact that solutions to the Dirichlet problem of Laplace's equation represent a "maximally smooth inter-/extrapolation" of the boundary values to the rest of the domain. Outside the convex hull around the heart, the "extrapolated" potentials only depend on the "exposed" parts of the boundary (otherwise the extrapolation would not be maximally smooth). The relative changes of the transfer strength for the different torso inhomogeneities are qualitatively the same as for TMVs. As the endocardium is the most concave part of the heart surface, this is where the transfer strength is smallest. About 1-2 cm below the rims at the base, the endocardial transfer strength is practically zero. Fig. 6.4 demonstrates that the error in BSPs made by setting the EEPs in the dark blue region in Fig. 6.1 (for which the transfer strength is smaller than 10 % of the mean on the epicardium) to zero is small – even for an activtity originating from the septum. Note that this does not mean that endocardial or septal activity does not contribute to BSPs but that it's contribution is already included in the EPs on the epicardium. For the inverse problem, this means that it is virtually impossible to reconstruct actual endocardial activity using EEPs as source model. This may explain why EEPs are not in widespread use compared to only PPs. If EEPs are used, the values reconstructed on the endocardium will almost exclusively be determined by the regularization (which defines their relation to the epicardial values) and not directly by the data.

As the transfer strength for TMVs on the endocardium has a similar magnitude as on the epicardium, TMVs should – in principle – allow a reconstruction of endocardial activity. However, if it is possible to reduce the sources of BSPs to a representation on only the epicardium plus a small part of the basal endocardium (using EEPs), then TMVs on the epi- and endocardium must inevitably be ambiguous with respect to BSPs. This is exactly what
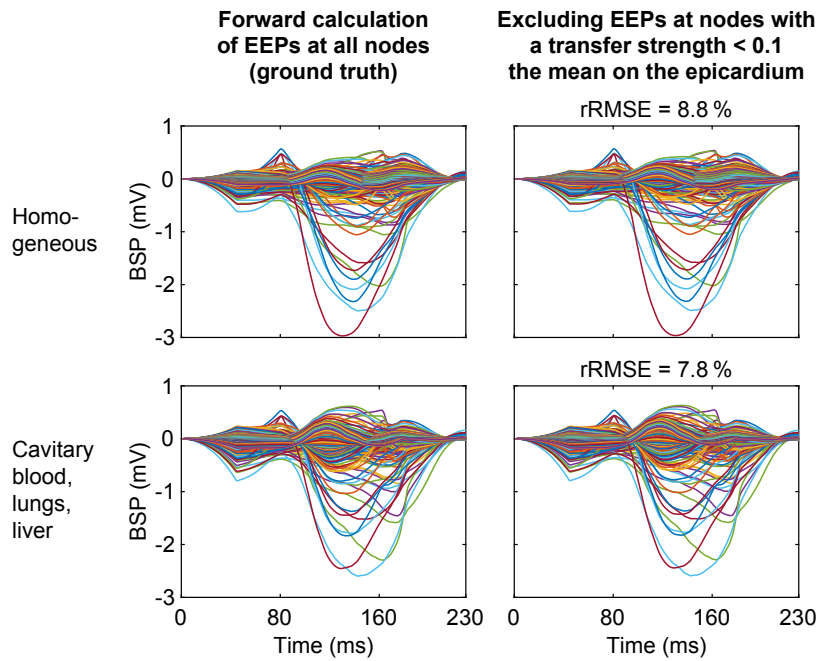
Figure 6.4: BSPs obtained by forward calculation of EEPs for a focal activation originating from the center of the RV septum. *Left:* Taking all cardiac nodes into account for forward calculation. *Right:* Excluding nodes with a transfer strength smaller than 10 % of the mean on the epicardium (dark blue regions in the right panel of Fig. 6.2). The resulting relative root-mean-square error (rRMSE) is given for two different torso models. The first epicardial breakthrough occurs at about 80 ms.
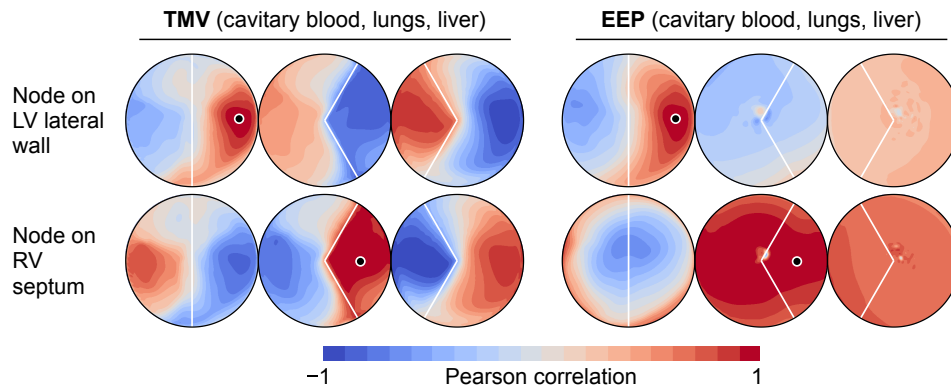
Figure 6.5: Correlation coefficients between the transfer coefficients of a single node and all other nodes. *First row:* For a node on the LV lateral wall. *Second row:* For a node on the RV septum. The respective node is marked by a black dot.

can be observed by a correlation analysis of the transfer coefficients for TMVs (left panel of Fig. 6.5). For two exemplary nodes marked with a black dot, the Pearson correlation coefficient between the corresponding column of the transfer matrix and all other columns is shown. It can be seen that there is a strong negative correlation between opposite sides of the myocardium. Furthermore, there is a strong correlation between the septum and parts

of the free walls oriented in parallel to the septum. While the ambiguity between opposite sides of the myocardium may be addressed by imposing transmural similarity, the ambiguity between the septum and the free walls cannot be resolved purely spatially. The only chance to overcome this ambiguity is to exploit the temporal or spatio-temporal evolution of TMVs. Therefore, the reconstruction of septal activity requires two ingredients: TMVs (or any other representation of sources on the right side of Poisson's equation) and temporal regularization. For completeness, the correlation coefficients for the same two nodes are also shown for EEPs (right panel of Fig. 6.5). For the node on the LV lateral wall, the correlation pattern on the epicardium looks very similar as for TMVs. For the node on the RV septum, ambiguities appearing on the endocardium are irrelevant, because the corresponding transfer strength is negligible.

The correlation analysis in Fig. 6.5 only shows ambiguities between individual nodes. As a measure of ambiguity between each one of the nodes and all other nodes, we suggest to perform zero-order Tikhonov regularization for each column $\widetilde{\mathbf{a}}_i$ in $\widetilde{\mathbf{A}}$ and optimizing λ such that the residual corresponds to a predefined SNR:

$$\lambda_i = \arg\min_{\lambda} \left(\frac{\|\widetilde{\mathbf{A}}\mathbf{w} - \widetilde{\mathbf{a}}_i\|_2}{\|\widetilde{\mathbf{a}}_i\|_2} - 10^{-\frac{\text{SNR}}{20}} \right)^2 \quad \text{with} \quad \mathbf{w} = (\widetilde{\mathbf{A}}^\mathsf{T}\widetilde{\mathbf{A}} + \lambda\,\mathbf{I})^{-1}\widetilde{\mathbf{A}}^\mathsf{T}\widetilde{\mathbf{a}}_i \qquad (6.2)$$

Here, $\mathbf{I}$ is the identity matrix. A large λ_i means that $\widetilde{\mathbf{a}}_i$ can be "easily" reproduced by a linear combination of the other columns and thus indicates a large ambiguity of transfer coefficients. The meaning of "easily" is defined by the zero-order Tikhonov constraint, which enforces a small norm of the weights $\mathbf{w}$. It thereby assures that not just nearby nodes get a large weight because their transfer coefficients are trivially similar. λ_i can be visualized on the heart surface. Fig. 6.6 shows the result for an SNR of 20 dB (plotted in log-scale and with respect to the mean on the epicardium). For TMVs (left panel), the largest ambiguities are indeed indicated at the septum, but there are also ambiguities at the anterior and posterior wall of the RV. In contrast, the anterior wall of the RV is most unambiguous for EEPs (right panel).
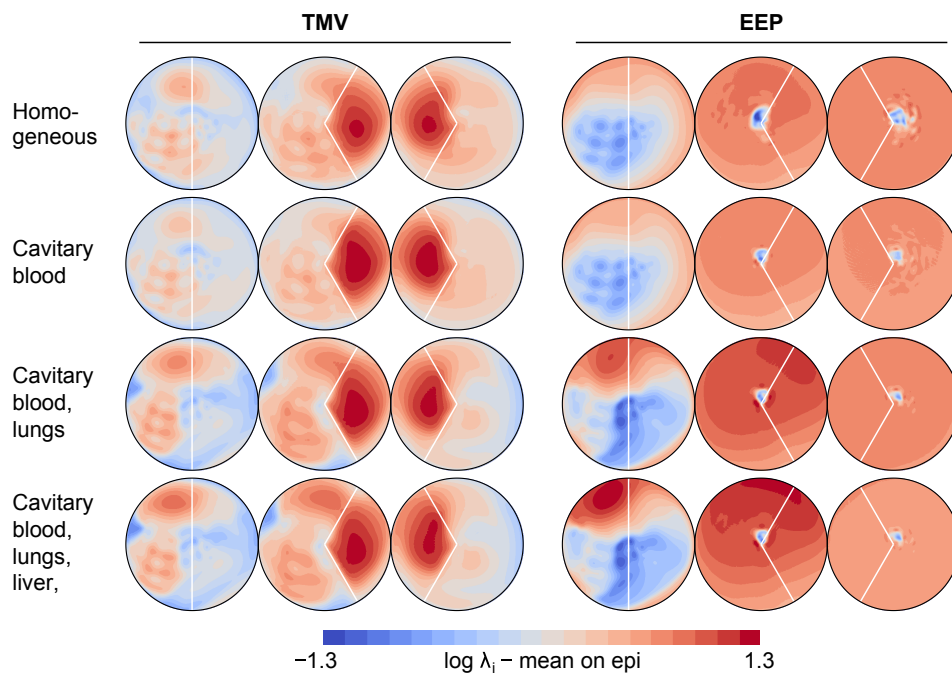
Figure 6.6: Ambiguity maps for TMVs and EEPs and four different torso models. The mean on the epicardium was subtracted from $\log \lambda_i$. For EEPs, the blue spot at the apical endocardium is an artifact (tiny $\widetilde{\mathbf{a}}_i$ in this region lead to a division by zero in (6.2)).

Laplacian Variants and Associated Point-Spread Functions

7.1 Transmural Laplacian

The analysis in the previous chapter revealed ambiguities for TMVs on opposite sides of the myocardial wall, which need to be resolved either by imposing transmural similarity or using temporal constraints. For second-order Tikhonov regularization and similar methods, a natural way to impose transmural similarity[1] is to use a Laplacian that not only operates in tangential but also in transmural direction. Erem et al. [47][2] developed an approach to estimate derivatives of functions defined on triangle meshes, which can also be used to obtain a transmural Laplacian. This approach is based on approximating the function using Euclidean-distance-weighted local quadratic fits (LQFs). We suggest an alternative approach, which uses an auxiliary tetrahedral mesh instead of Euclidean distances to define neighborhoods and a classical first-order approximation of the function over the tetrahedrons instead of LQFs. First, a tetrahedral volume mesh is generated that conforms to the triangle mesh [48]. The Laplacian of the volume mesh is then used for Laplacian interpolation of the function values from the surface to the entire volume and then applied to interpolated values. Next, the resulting values are mass-normalized and only the surface values are extracted. Mathematically, the new transmural Laplacian for triangle meshes can be written as:

$$\mathbf{L} = \mathbf{S}_{s \leftarrow v} \, \mathbf{M}_v^{-1} \, \mathbf{C}_v \, \mathbf{S}_{v \leftarrow s} \tag{7.1}$$

The index s refers to the triangulated surface mesh and the index v to the tetrahedral volume mesh. $\mathbf{C}_v$ is the Laplacian of the volume mesh as in (3.25). $\mathbf{S}_{v \leftarrow s}$ is a matrix that performs

---

[1]For the thin-walled atria, another way to impose transmural similarity is the epi-endo projection we proposed in [46].

[2]https://github.com/jcollfont/activationtimes
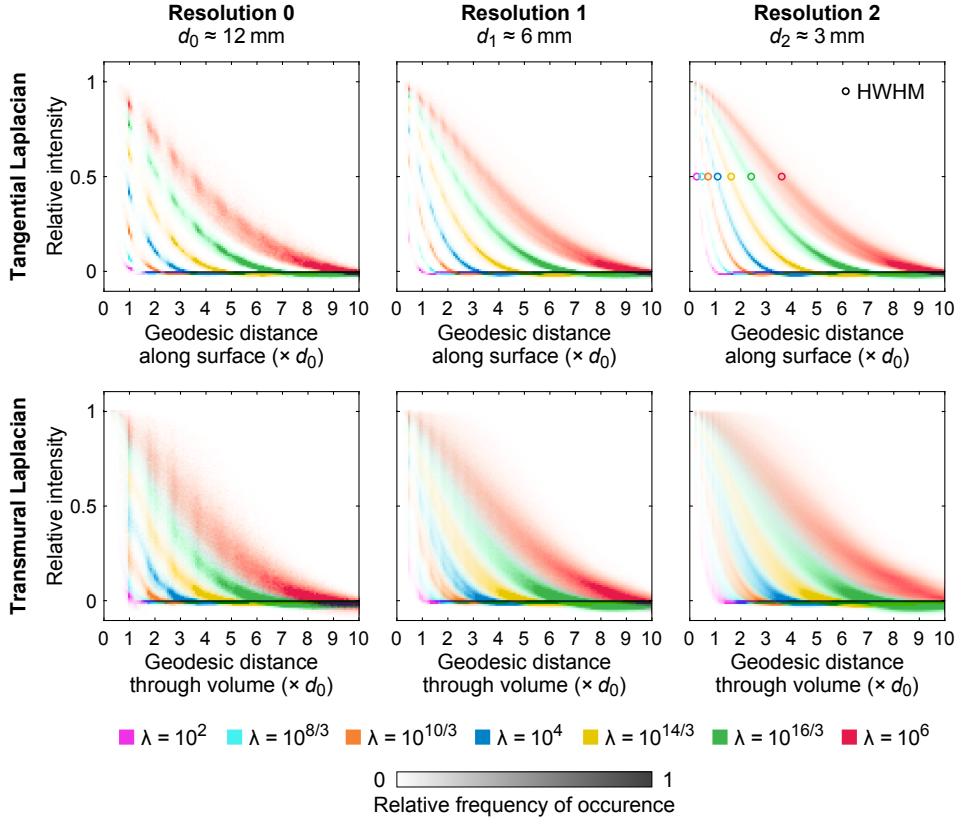
Figure 7.1: PSFs of blurring using the tangential (*top*) and the transmural (*top*) surface Laplacian for log-spaced values of λ. Shown are 2D histograms; the color intensity represents the frequency of occurence. PSFs for three mesh resolutions with mean edge lengths d are shown.

Laplacian interpolation from the surface to the volume mesh and is obtained using method B in [49] (with $\mathbf{C}_v$ as Laplacian). $\mathbf{M}_v$ is the mass matrix of the volume mesh and $\mathbf{S}_{s\leftarrow v}$ is a matrix that simply extracts the surface values from the volume mesh.

To analyze the Laplacians, we determined point spread functions (PSF) of the associated "Laplacian blurring operator" $\mathbf{P}$:

$$\mathbf{P} = (\mathbf{I} + \lambda\,\mathbf{L}^\mathsf{T}\mathbf{L})^{-1} \tag{7.2}$$

Here, $\mathbf{I}$ is the identity matrix and $\mathbf{L}$ is one particular Laplacian. Fig. 7.1 shows the PSFs for the tangential Laplacian (first row) and the new transmural Laplacian (second row). The PSFs were obtained by setting the value at a single node of a biventricular geometry to one and all others to zero. Then, $\mathbf{P}$ was applied and the resulting values were plotted over the geodesic distance to the respective "source" node. This was repeated for all nodes of the mesh, seven values of λ and three different mesh resolutions. Instead of the individual data points, a 2D histogram of all data points for each λ is shown in Fig. 7.1. The vertical stripes in the histograms correspond to the inter-node spacing of the respective mesh. It can be seen that the PSFs for the transmural Laplacian have very similar shapes as the PSFs for the tangential Laplacian. Ideally, each histogram should resemble a sharply defined curve. This
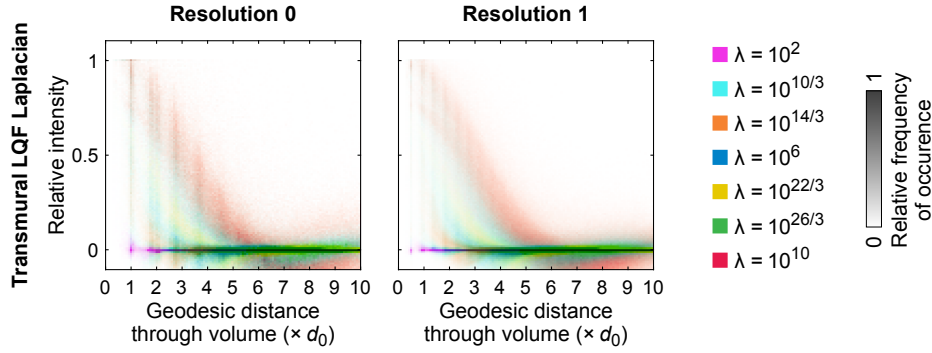
Figure 7.2: PSFs as in Fig. 7.1 but for the LQF Laplacian from [47] using Gaussian weights ($\sigma = 12\,\text{mm}$). Resolution 2 is not shown as the computation time increased drastically with the number of nodes.

is the case for the tangential Laplacian (at least for small λs). For the transmural Laplacian, the PSFs are more spread out, but still relatively sharply defined. For comparison, PSFs were also determined for the LQF Laplacian (using Gaussian weights with $\sigma = 12\,\text{mm}$). Fig. 7.2 shows that the PSFs of this Laplacian are less sharply defined.

To determine the relation between the width of the PSF and λ, the half-width at half-maximum (HWHM) was determined from the histograms for the tangential Laplacian (see top-right diagram in Fig. 7.1). Fig. 7.3 shows that the relation can be approximated by:

$$\lambda = \left(\frac{3}{4}\,\text{HWHM} \right)^4 \qquad (7.3)$$

This function is also applicable for the new transmural Laplacian.
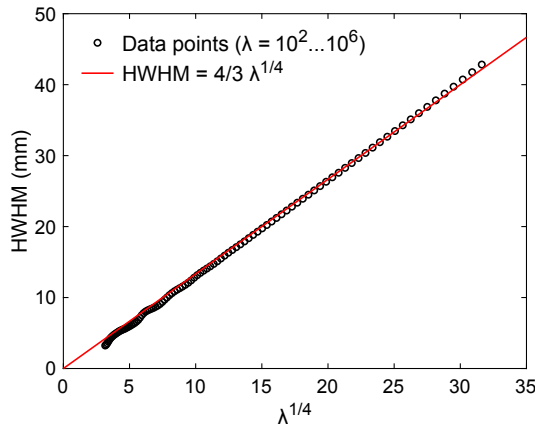
Figure 7.3: HWHM of the point spread function in Fig. 7.1 (Tangential Laplacian, Resolution 2) as function of λ.

For an exemplary λ, the PSFs on the mesh with resolution 1 are depicted in Fig. 7.4 (new Laplacian) and Fig. 7.5 (LQF Laplacian). Here, another difference between the two operators

can be observed. The new Laplacian assumes zero Neumann boundary conditions (see section 3.8), which distorts the PSF at the base. This is not the case for the LQF Laplacian. Although the distortion becomes only relevant for large λs, this can be an advantage of the LQF Laplacian.
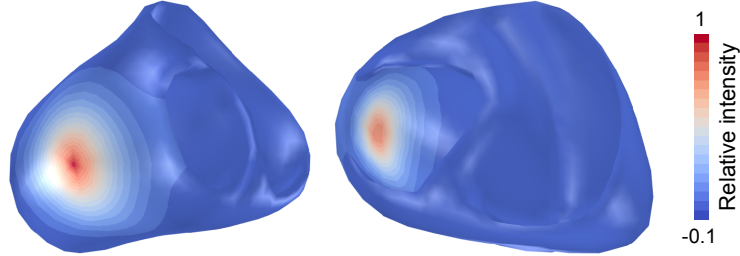
Figure 7.4: PSF of the transmural Laplacian for a node on the LV epicardium ($\lambda = 10^4$).
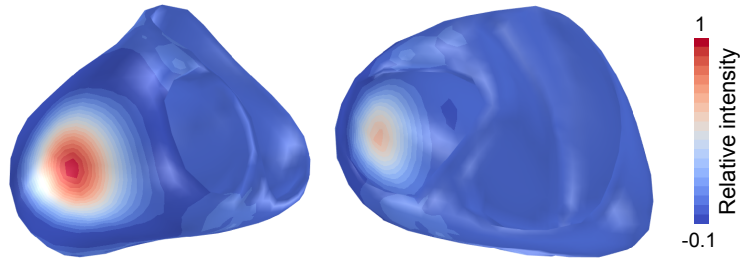
Figure 7.5: PSF as Fig. 7.4 but for the LQF Laplacian ($\lambda = 10^6$).

7.2 Anisotropic Laplacian

All Laplacians mentioned so far are isotropic. An anisotropic Laplacian can be defined as:

$$\Delta_{\mathbf{D}} f = \nabla \cdot (\mathbf{D}\nabla f) \tag{7.4}$$

The "diffusivity" tensor $\mathbf{D}$ encodes the anisotropy. A discretization of $\Delta_{\mathbf{D}}$ for triangle meshes has been derived in [50]. However, we need a discretization for tetrahedral meshes, as the fiber orientation of the heart changes transmurally and we wish to obtain an anisotropic Laplacian that also operates in transmural direction. An advantage of the derivation in section 3.8 is that it also allows to directly translate (7.4) into the discrete setting. The introduction of $\mathbf{D}$ extends (3.25) to:

$$\mathbf{C_D} = -\mathbf{G}^{\mathsf{T}}\,\mathbf{T}\,\overline{\mathbf{D}}\,\mathbf{G} \tag{7.5}$$

Here, $\overline{\mathbf{D}}$ represents the multiplication with $\mathbf{D}$ at all elements at once. For transverse isotropy, $\mathbf{D}$ can be defined as:

$$\mathbf{D} = \mathbf{R} \begin{pmatrix} a^{-1} & 0 & 0 \\ 0 & a^{-1} & 0 \\ 0 & 0 & a^2 \end{pmatrix} \mathbf{R}^{\mathsf{T}} \tag{7.6}$$

$\mathbf{R}$ is the same as in (3.20) and a is an anisotropy ratio leading to a larger diffusivity in longitudinal than in transversal fiber direction. The diagonal entries of the central matrix are chosen such that the volume of an ellipsoid with the corresponding semi-axes is independent of a. To resolve the fiber rotation across the myocardial wall, $\mathbf{C_D}$ has to be computed for a relatively fine tetrahedral mesh with at least three tetrahedrons across the wall. Having obtained $\mathbf{C_D}$, equation 7.1 can be used to obtain an anisotropic transmural Laplacian $\mathbf{L}$ for a coarse triangle mesh suitable for ECGI. Note that although the resulting $\mathbf{L}$ maps from and to the nodes of the coarse triangle mesh, it includes the fine-grained fiber orientation of the finer tetrahedral mesh used to compute $\mathbf{C_D}$.

Fig. 7.6 visualizes the PSF of the anistropic transmural Laplacian for $a = 3$. The black lines indicate the fiber orientations on the epi- and endocardial surface. Note that the apparent difference of the main axis of blurring and the fiber orientation on the epicardium is not a bug but results from the transmurally rotating fibers. While the pattern on the epicardium has the shape of an ellipse, the pattern on the endocardium is almost circular in shape.
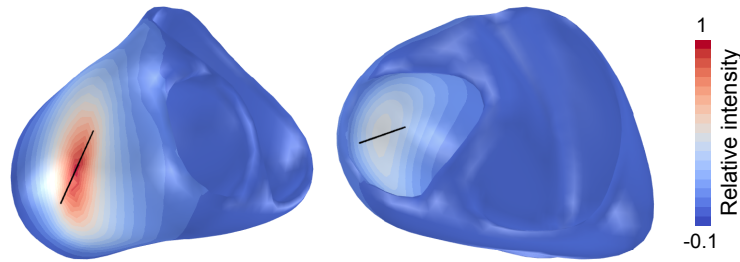
Figure 7.6: PSF as in Fig. 7.4 but for an anisotropic transmural Laplacian ($\lambda = 10^3$). The underlying fiber orientations rotate linearly across the wall. The black lines indicate the fiber orientations on the epi- and endocardium.

Spatial Downsampling of Surface Sources for Fast Forward Calculations

As mentioned in section 3.5, one drawback of BEM is the resulting dense system matrix, which limits the resolution of surface meshes that can be used for forward calculations without running out of memory or requiring long computation times. However, a spatial resolution below 1 mm is required to capture the upstroke of the TMV during depolarization or the corresponding downslope of the EP. Just mapping the cardiac sources from a fine mesh used for excitation simulations onto a coarser mesh used for BEM ("direct downsampling") causes the activation to abruptly "jump" from one node to the other, which leads to jagged time courses of BSPs (see left half of Fig. 8.1).

In [51], we hypothesized that, although high spatial frequencies associated with depolarization cannot be represented on a coarse mesh, low frequency components are sufficient to obtain a good approximation of BSPs, as the torso itself has a strong smoothing effect. We evaluated different approaches to blur the sources before downsampling and suggested a method to optimize the blurring parameter. Blurring using a tangential Laplacian ("Laplacian blur downsampling") led to an accurate approximation of BSPs, even for very coarse meshes (right half of Fig. 8.1). For a mesh with only 578 nodes and a mean edge length of 12 mm, the resulting relative root-mean-square error (rRMSE) of BSPs was about 5 % and decreased below 1 % for a mesh with a mean edge length of 3 mm. For further details, see [51].

These results confirm that a major ambiguity exists between sharp and spatially blurred versions of the cardiac sources. It also explains why second-order Tikhonov regularization is a reasonable approach to ECGI in the sense that it allows a good fit to the data while addressing a major factor responsible for ill-posedness – despite the fact that spatial smoothness is clearly not a very physiological constraint.
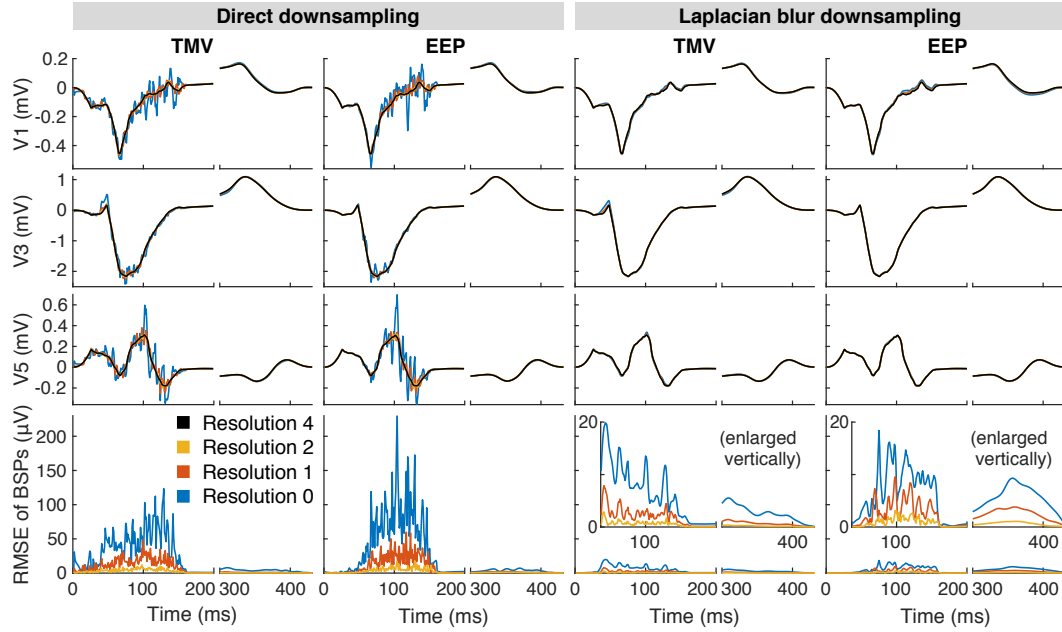
Figure 8.1: Illustration of the BSPs (Wilson leads V1, V3 and V5) resulting from direct downsampling (*left*) and Laplacian blur downsampling (*right*) of TMVs and EEPs from a fine mesh (resolution 4: 0.8 mm mean edge length) to coarser meshes (resolution 2: 3 mm, resolution 1: 6 mm, resolution 0: 12 mm). Adapted from [51] with permission.

Laplacian blur downsampling of the sources is equivalent to an "interpolation" of the transfer coefficients from the coarse to the fine mesh and using the "interpolated" transfer coefficients for forward calculation of the sources on the fine mesh:

$$\mathbf{b} = \mathbf{A}\,\mathbf{x}_{\text{coarse}} = \mathbf{A}\,\mathbf{S}\,\mathbf{P}\,\mathbf{x}_{\text{fine}} = (\mathbf{P}\,\mathbf{S}^{\mathsf{T}}\mathbf{A}^{\mathsf{T}})^{\mathsf{T}}\mathbf{x}_{\text{fine}} \tag{8.1}$$

Here, **b** are the BSPs, $\mathbf{x}_{\text{coarse}}$ the sources on the coarse mesh and $\mathbf{x}_{\text{fine}}$ the sources on the fine mesh. **P** is the Laplacian blurring operator as in (7.2) and **S** performs the actual downsampling by extracting values at the nodes of the fine mesh corresponding to the nodes of the coarse mesh. The matrix $\mathbf{P}\,\mathbf{S}^{\mathsf{T}}$ on the right of (8.1) performs the "interpolation" of the transfer coefficients: $\mathbf{S}^{\mathsf{T}}$ copies the values to the nodes of the fine mesh (assigning zero to nodes for which there are no corresponding nodes in the coarse mesh) and **P** then "distributes" the non-zero values in space. Blurring the sources rather than "interpolating" the transfer coefficients has the advantage that a coarse version of the source distribution corresponding to the BSPs is obtained, which can be useful for simulation-based inverse methods like the BSPs regression in section 10.2.

PART III

SOLVING THE INVERSE PROBLEM

This part covers the methods used in this work to solve the inverse problem ("inverse methods") and to post-process the inverse solutions in order to obtain diagnostically relevant information. In chapter 9, state-of-the-art inverse methods will be described. Novel inverse methods will be introduced in chapter 10. Chapter 11 deals with the post-processing steps. The main evaluation of all of the inverse methods will follow in part IV. Here, only selected examples will be presented to illustrate the methods.

State-of-the-Art Inverse Methods

9.1 Tikhonov Regularization (Tik)

Second-order Tikhonov regularization with a transmural Laplacian and a time-constant λ was used for the evaluation in this thesis. Although an optimal λ for each time step can potentially improve the results (see for example our evaluation in [46]), we chose to use a time-constant λ, because for clinical data, it can be challenging to reliably determine even a single λ. Using a time-constant λ, the solution can be computed for all time steps at once:

$$\widehat{\mathbf{X}} = \arg\min_{\mathbf{X}} \big(\|\mathbf{AX} - \mathbf{B}\|_{\mathrm{F}}^2 + \lambda \|\mathbf{LX}\|_{\mathrm{F}}^2 \big) = (\mathbf{A}^\mathsf{T}\mathbf{A} + \lambda\,\mathbf{L}^\mathsf{T}\mathbf{L})^{-1}\mathbf{A}^\mathsf{T}\mathbf{B} \qquad (9.1)$$

Here, $\|\cdot\|_{\mathrm{F}}$ denotes the Frobenius norm. $\mathbf{A} \in \mathbb{R}^{M \times N}$ is the transfer matrix and $\mathbf{L} \in \mathbb{R}^{N \times N}$ is the Laplacian. $\mathbf{B} \in \mathbb{R}^{M \times K}$ are the BSPs and $\mathbf{X} \in \mathbb{R}^{N \times K}$ the cardiac sources for K time steps. M is the number of electrodes and N the number of cardiac nodes.

Tikhonov regularization was evaluated for both EEPs and TMVs, while all other methods were only evaluated for TMVs. In total, Tikhonov regularization was evaluated in the following three variants, which will be referred to as denoted in the bracket:

- Tikhonov regularization with EEPs and an isotropic Laplacian (Tik EEP)
- Tikhonov regularization with TMVs and an isotropic Laplacian (Tik)
- Tikhonov regularization with TMVs and an anisotropic Laplacian (Tik aniso)

For TMVs, only the spatial gradient of the solution has an effect on BSPs and spatially constant solutions are in the nullspace of both the transfer matrix and the Laplacian. Therefore, the Laplacian was modified for TMVs by adding a matrix full of ones [4, sec. 7.2.1]. This forces the solution to have a spatial mean of zero.

9.2 Tikhonov-Greensite Regularization (TikGS)

Tikhonov-Greensite regularization (TikGS) refers to the method suggested by Greensite and Huiskamp in [52], which performs Tikhonov regularization for the projections $\mathbf{B_V}$ of BSPs

onto their P most important temporal singular vectors:[1]

$$\widehat{\mathbf{X}}_{\mathbf{V}}(:,p) = \arg \min_{\mathbf{X}_{\mathbf{V}}(:,p)} \left(\|\mathbf{A}\mathbf{X}_{\mathbf{V}}(:,p) - \mathbf{B}_{\mathbf{V}}(:,p)\|_2^2 + \lambda_p \|\mathbf{L}\mathbf{X}_{\mathbf{V}}(:,p)\|_2^2 \right) \qquad (9.2)$$

$$\text{with} \quad p = 1, 2, \ldots, P, \quad \mathbf{B}_{\mathbf{V}} = \mathbf{B}\mathbf{V}(:,1{:}P), \quad \mathbf{B} = \mathbf{U}\mathbf{S}\mathbf{V}^{\mathsf{T}}$$

$\widehat{\mathbf{X}}_{\mathbf{V}}$ is then transformed back into temporal space:

$$\widehat{\mathbf{X}} = \widehat{\mathbf{X}}_{\mathbf{V}}\mathbf{V}(:,1{:}P)^{\mathsf{T}}$$

As this method performs spatial Tikhonov regularization after applying a temporal transformation, it may be considered a spatio-temporal method. However, it treats time and space independently and does not introduce additional a priori information compared to Tik. The main advantage of TikGS is that each temporal component is regularized optimally – given an optimal λ_p can be determined for each component. If the same fixed λ is used for all components, the only advantage is a reduction of uncorrelated noise.

Based on the observation that the cumulative sum of singular values has a kink at $P = 7$, this value was used here and an individual λ_p was determined for each component. Although not used in this thesis, it is worth mentioning that Erem et. al [47] suggested a related method that uses low-order splines instead of a truncated SVD as data-driven temporal model. In combination with TMVs, both methods have been tested in [53].

9.3   Temporal Non-Decreasing Regularization (TND)

Temporal non-decreasing regularization (TND) refers to the spatio-temporal method by Messnarz et al. [54], which adds lower and upper bounds of the TMVs and an inequality constraint that forces the TMVs to not decrease over time:

$$\widehat{\mathbf{x}}(t) = \arg \min_{\mathbf{x}(t)} \left(\|\mathbf{A}\mathbf{x}(t) - \mathbf{b}(t)\|_2^2 + \lambda \|\mathbf{L}\mathbf{x}(t)\|_2^2 \right) \qquad (9.3)$$

$$\text{subject to}$$

$$0 \le \mathbf{x}(t) \le V_{\max} \quad \text{and} \quad \mathbf{x}(t) \le \mathbf{x}(t{+}1)$$

Here, t denotes the time step and $V_{\max}$ is the upper bound of TMVs. This quadratic optimization problem with linear constraints was solved in CVX [55] using Mosek's interior-point optimizer [56]. TND adds temporal prior knowledge that is only valid during depolarization. Therefore, only the QRS interval was included for this method. To reduce the computational load, the sampling frequency was reduced to 250 Hz. As spatially constant offsets of TMVs are in the nullspace of the transfer matrix, the non-decreasing constraint is only effective if the upper bound is not too large. Choosing it too small, however, is also problematic.

---

[1]Here, a MATLAB-like notation is used to address matrix elements.

9.4 Body Surface Potential Correlation (BC)

Body surface potential correlation (BC) refers to a brute-force search in which the measured BSPs are correlated with many simulated BSPs of focal excitations. The resulting Pearson correlation coefficients are Laplacian interpolated over the entire heart surface and the point with the highest correlation coefficient is identified as excitation origin.

For each patient, approximately 600 foci were uniformly distributed over the epi- and endocardial surface and focal excitation simulations were performed using an isotropic (BC iso) and an anisotropic (BC aniso) eikonal model. The CV was set to $v = 0.6 \frac{m}{s}$ [57]. For the anisotropic model, fiber orientations were defined as described in section 3.7 and the anisotropy ratio was set to $a = 2.7$ [57]. A step function was used as TMV template.

The correlation was performed over nodes and time steps at once. Only the first half of the QRS interval of the measured BSPs was taken into account for correlation. As the true start of activation and the actual CV are unknown, the correlation was performed for multiple time shifts and multiple time scalings applied to the measured BSPs:

- 11 time shifts: $-25\,\text{ms}, -20\,\text{ms}, \ldots, 25\,\text{ms}$ (with respect to the QRS onset)
- 11 time scalings: $0.5, 0.6, \ldots, 1.5$

Therefore, $11 \cdot 11 = 121$ correlations were evaluated for each of the 600 foci.

Novel Inverse Methods

In this chapter, three novel inverse methods will be presented. Each of these methods incorporates prior knowledge about the spatio-temporal spread of cardiac excitation into the solution process. The delay-based regularization in section 10.1 does this using an explicit regularization term and does not use any simulated data for reconstruction. In contrast, the body surface potential regression in section 10.2 incorporates prior knowledge by projecting the data onto a feasible set determined from simulations. Finally, the deep learning-based approach in section 10.3 uses simulated data to establish a direct relation between the BSPs and the position of the excitation origin. The first two methods are ECGI methods, while the last method does not reconstruct an image of the cardiac activity. For a probabilistic framework allowing a common ground comparison of different approaches to ECGI, see [58].

Before starting with the delay-based regularization, a few comments on spatio-temporal constraints shall be made. Cardiac electrical sources – in particular TMVs – have a strong temporal structure that can be exploited for regularization. A key property of cardiac excitation spread related to the time course of TMVs is refractoriness: After depolarization, it takes hundrets of milliseconds before the TMV falls below a level at which the cell can be excited again. A reconstruction in which the TMVs in a certain region change multiple times within a short time between levels corresponding to the de- and repolarized state are unphysiological. Preventing such a behavior using temporal constraints can resolve ambiguities existing in the purely spatial problem. For an excitation originating from the septum, for example, the TMVs reconstructed using spatial Tikhonov regularization may indicate a wavefront that "jumps" between the septum and the anterior wall of the RV as time progresses, because there are ambiguities between these two regions. Forcing the TMVs to not decrease over time, as done in TND, can resolve this ambiguity: The wavefront has to start on the septum, because if it were to start at the RV anterior wall (in the reconstruction), this would cause a violation of the non-decreasing constraint at later time steps, i.e. when the RV anterior wall would have to become repolarized in order to be activated once again by a (correctly reconstructed) wavefront coming from regions with unique transfer coefficients. Although clearly an advancement, TND still misses an important feature: During depolarization, TMVs should not be allowed to increase just slowly or to rest at a certain level. They should increase rapidly in an all-or-none fashion. Note also that extending spatial Tikhonov regularization

by imposing additional temporal smoothness as in [59] cannot effectively resolve such an ambiguity: The magnitude of the depolarized area may just decrease smoothly in time on the septum and simultaneously increase smoothly in time on the RV anterior wall (or vice versa). A very strong way to include temporal prior knowledge is to assume a specific, parameterized time course for TMVs and solving directly for the activation times. This approach is known as AT imaging [60–62] and leads to a non-linear, non-convex optimization problem that is sensitive to the initialization [63]. Furthermore, the actual TMVs may not match the assumed time course.

10.1 Delay-Based Regularization (DR)

The delay-based regularization (DR) first introduced in [64] attempts to provide an effective way to introduce temporal prior knowledge with weaker assumptions on the time course of TMVs than AT imaging and circumventing the non-convex optimization problem. The basic idea is to impose similarity between time-aligned TMVs of nearby nodes. In [65], the concept of using time-alignment to increase the spatial similarity of cardiac signals has been used for "wave-equation based interpolation" of EPs. Given the stereotypical time course of the action potential, time-aligned TMVs should be even more similar than time-aligned EPs. DR can be written as:

$$\hat{\overline{\mathbf{x}}} = \arg\min_{\overline{\mathbf{x}}} \big(\|\overline{\mathbf{A}}\overline{\mathbf{x}} - \overline{\mathbf{b}}\|_2^2 + \lambda_L \|\overline{\mathbf{L}}\overline{\mathbf{x}}\|_2^2 + \lambda_D \|\mathbf{D}\overline{\mathbf{x}}\|_2^2 \big) \tag{10.1}$$

$$\Leftrightarrow \quad (\overline{\mathbf{A}}^\mathsf{T}\overline{\mathbf{A}} + \lambda_L \overline{\mathbf{L}}^\mathsf{T}\overline{\mathbf{L}} + \lambda_D \mathbf{D}^\mathsf{T}\mathbf{D}) \,\hat{\overline{\mathbf{x}}} = \overline{\mathbf{A}}^\mathsf{T}\overline{\mathbf{b}} \tag{10.2}$$

Here, we use the notation from [59] to obtain an augmented problem including time. Overlines indicate block diagonal matrices or block vectors:

$$\overline{\mathbf{A}} = \mathbf{I}_T \otimes \mathbf{A} \tag{10.3}$$

$$\overline{\mathbf{L}} = \mathbf{I}_T \otimes \mathbf{L} \tag{10.4}$$

$$\overline{\mathbf{x}} = [\mathbf{x}_1^\mathsf{T}, \dots, \mathbf{x}_T^\mathsf{T}]^\mathsf{T} \tag{10.5}$$

$$\overline{\mathbf{b}} = [\mathbf{b}_1^\mathsf{T}, \dots, \mathbf{b}_T^\mathsf{T}]^\mathsf{T} \tag{10.6}$$

T is the number of time steps, $\mathbf{I}_T$ is a $T \times T$ identity matrix and $\otimes$ denotes the Kronecker product. $\mathbf{A}$ is the transfer matrix transforming TMVs $\mathbf{x}$ into BSPs $\mathbf{b}$ and $\mathbf{L}$ is the transmural Laplacian. The last summand in (10.1) respresents the new delay-based constraint. $\mathbf{D}$ is an $P \cdot T \times T \cdot N$ matrix (the exact number of rows depends on the boundary condition, see Fig. 10.1). N is the number of nodes and P is the number of pairs of nearby nodes. For every node pair, this matrix calculates the differences of signals after alignment in time using previously determined delays. These delays between nodes of each pair are updated iteratively. $\mathbf{D}$ has to be reassembled for every new set of delays. $\mathbf{D}$ does not have a block structure. Fig. 10.1 shows the MATLAB code to construct $\mathbf{D}$. Two different types of temporal boundary conditions can be chosen. Without periodic boundary conditions (left half of Fig. 10.1), border values are repeated for time steps that do not overlap after time alignment,

```matlab
% pairs:  P x 2 node indices
% delays: P x 1 non-negative integer delays (activation time difference for each pair)
```

```matlab
% Difference matrix D(i(k),j(k)) = v(k)        % Difference matrix D(i(k),j(k)) = v(k)
% WITHOUT periodic boundary conditions         % WITH periodic boundary conditions

sd = sum(delays);
c = 0;

i = repmat(1:P*T+sd,1,2);                       i = repmat(1:P*T,1,2);
j = NaN(1,2*(P*T+sd));                           j = NaN(1,2*P*T);
v = [ones(1,P*T+sd) -ones(1,P*T+sd)];            v = [ones(1,P*T) -ones(1,P*T)];

for p = 1:P                                      for p = 1:P
    n1 = pairs(p,1);                                 n1 = pairs(p,1);
    n2 = pairs(p,2);                                 n2 = pairs(p,2);
    d = delays(p);                                   d = delays(p);

    % Minuends: D(i(k1),j(k1)) = 1                   % Minuends: D(i(k1),j(k1)) = 1
    k1 = (p-1)*T+1+c : p*T+c+d;                      k1 = (p-1)*T+1 : p*T;
    j1 = n1:N:n1+(T-1)*N;                            j1 = n1+d*N:N:n1+(T-1+d)*N;
    j(k1) = [j1 repmat(j1(end),1,d)];               j(k1) = mod(j1-1,T*N)+1;

    % Subtrahends: D(i(k2),j(k2)) = -1               % Subtrahends: D(i(k2),j(k2)) = -1
    k2 = (P+p-1)*T+1+sd+c : (P+p)*T+sd+c+d;          k2 = (P+p-1)*T+1 : (P+p)*T;
    j2 = n2:N:n2+(T-1)*N;                            j2 = n2:N:n2+(T-1)*N;
    j(k2) = [repmat(j2(1),1,d) j2];                 j(k2) = j2;

    c = c+d;
end                                              end

D = sparse(i,j,v,P*T+sd,T*N);                    D = sparse(i,j,v,P*T,T*N);
```

Figure 10.1: MATLAB code to construct the difference matrix **D**. *Left:* Construction without periodic boundary conditions. Here, border values are repeated for time steps that do not overlap after time-alignment (note the `repmat`). *Right:* Construction with periodic boundary conditions. Here, indices exceeding the end of the signal are shifted circularly (note the `mod`). Differences between both code variants are highlighted in red.

i.e. the difference is calculated with the closest time step available in the other signal. With periodic boundary conditions (right half of Fig. 10.1), indices for non-overlapping time steps are circularly shifted to the other end of the signal. Periodic boundary conditions enforce the same value for TMVs at the beginning and the end of the signal, which should be particularly appropriate for cyclic activities like VT.

10.1.1 Solving The Linear System

Equation (10.1) is a system of $T \cdot N$ linear equations and can become very large, if many time steps or many nodes are used. Since the left-hand-side matrix is sparse, symmetric and positive definite, it can be solved using the conjugate gradient method. However, the

minimum residual method (MINRES) turned out to be more efficient for this problem. The following approximate inverse was found to work well as a preconditioner ($\mathbf{I}_N$ is an $N \times N$ identity matrix):

$$\overline{\mathbf{M}} = \mathbf{I}_T \otimes \mathbf{M} \quad \text{with} \quad \mathbf{M} = (\mathbf{A}^\mathsf{T}\mathbf{A} + \lambda_L \mathbf{L}^\mathsf{T}\mathbf{L} + \lambda_D \mathbf{I}_N)^{-1} \tag{10.7}$$

We use the MATLAB implementation of MINRES with function handles replacing both the coefficient matrix and the preconditioner matrix. This allows to save a lot of memory, as the block diagonal matrices do not have to be created explicitly. Instead, $\overline{\mathbf{x}}$ is reshaped into a matrix $\mathbf{X}$ and multiplications with $(\mathbf{A}^\mathsf{T}\mathbf{A} + \lambda_L \mathbf{L}^\mathsf{T}\mathbf{L})$ in (10.2) and $\mathbf{M}$ in (10.7) are performed as a matrix product (note the missing overlines). Only the multiplication with $\mathbf{D}^\mathsf{T}\mathbf{D}$ in (10.1) has to be done using the block vector form $\overline{\mathbf{x}}$. As $\mathbf{D}$ has only $2 \cdot P \cdot T$ nonzero elements, this is not a problem (the exact number of non-zeros depends on the boundary condition, see Fig. 10.1).

10.1.2 Iterative Update of Delays and Choice of Regularization Parameters

Our aim is to get a solution that is predominantly regularized by the delay-based constraint. However, optimal delays are not known beforehand. Thus, we perform an initial reconstruction using second order Tikhonov, which is equivalent to setting λ_D to zero in (10.1). Delays are determined from activation times estimated from this initial solution and updated iteratively from solutions obtained by gradually letting λ_L go to zero and increasing λ_D. Throughout iterations, λ_L is reduced according to a smooth function and λ_D is increased.

Solving (10.1) many times with a fixed λ_L to obtain an L-curve for λ_D is computationally demanding. Therefore, we use a different approach: λ_D is adjusted, so that the data misfit term $\|\overline{\mathbf{A}}\overline{\mathbf{x}} - \overline{\mathbf{b}}\|_2$ is held constant. This is achieved by finding the root of the following residual using the secant method:

$$r_i(\lambda_D') = \|\overline{\mathbf{A}}\overline{\mathbf{x}}_i(\lambda_D') - \overline{\mathbf{b}}\|_2 - \|\overline{\mathbf{A}}\overline{\mathbf{x}}_1 - \overline{\mathbf{b}}\|_2 \quad \text{with} \quad \lambda_D' = \log(\lambda_D)$$

$\overline{\mathbf{x}}_1$ is the initial solution obtained for $\lambda_L = \lambda_{L,1}$, $\lambda_D = 0$. To further speed up computations, λ_D' is extrapolated quadratically from previous iterations before running the secant method. Moreover, the previous solution $\overline{\mathbf{x}}_{i-1}$ is used as initial estimate for MINRES.

For the evaluation in this thesis, λ_L was reduced by 3 decades across 50 iterations:

$$\lambda_{L,i} = 10^{-3\,(i-1)/(50-1)}\, \lambda_{L,1} \quad \text{with} \quad i = 1, \ldots, 50$$

10.1.3 Theoretical Considerations

As only the gradient of TMVs produces BSPs (see equation 3.8), spatially constant offsets of TMVs are in the nullspace of $\mathbf{A}$ and cannot be recovered with the static inverse problem, i.e. by reconstructing each time step independently. The delay-based constraint however,

links time and space in a way that allows to recover such nullspace components. Suppose, for example, the spatial gradient of TMVs is zero. For each time step, any spatially constant value of TMVs would thus be allowed by the term $\|\overline{\mathbf{A}}\overline{\mathbf{x}} - \overline{\mathbf{b}}\|_2^2$. However, such an arbitrary, time-changing value would lead to deviations of time-shifted signals and is thus not permitted, as it leads to a large value of $\|\mathbf{D}\overline{\mathbf{x}}\|_2^2$. In other words, the temporal change of spatially constant offsets is made unique by the delay-based constraint. What remains undetermined is a spatially *and* temporally constant offset.

Following the same line of reasoning, a common deflection in time-aligned TMVs will lead to a spatial gradient in non-aligned TMVs that has to fit to the given BSPs. From theoretical considerations, the delay-based constraint therefore adds a regularization that is particularly effective for TMVs, while supporting their physiological properties.

However, there is an ambiguity between the size of the delays and the TMV amplitude: It is possible to decrease the time delays while increasing the TMV amplitude such that the spatial gradients of TMVs – and thus also the BSPs – do not change. For a simple one-dimensional example with only two nodes, this is illustrated in Fig. 10.2. In the diagram at the top-left, the two black sigmoids represent TMV time courses for the two nodes with a predefined delay of $\Delta t = 1$. The red and blue curves were obtained by scaling the delay by a factor of 0.6 and 0.2, respectively, subject to the constraint that their difference ΔTMV (the TMV gradient) stays the same as for the black curves (diagram at the bottom-left). It can be seen that there is a reciprocal relation between the delays and the TMV amplitude. The
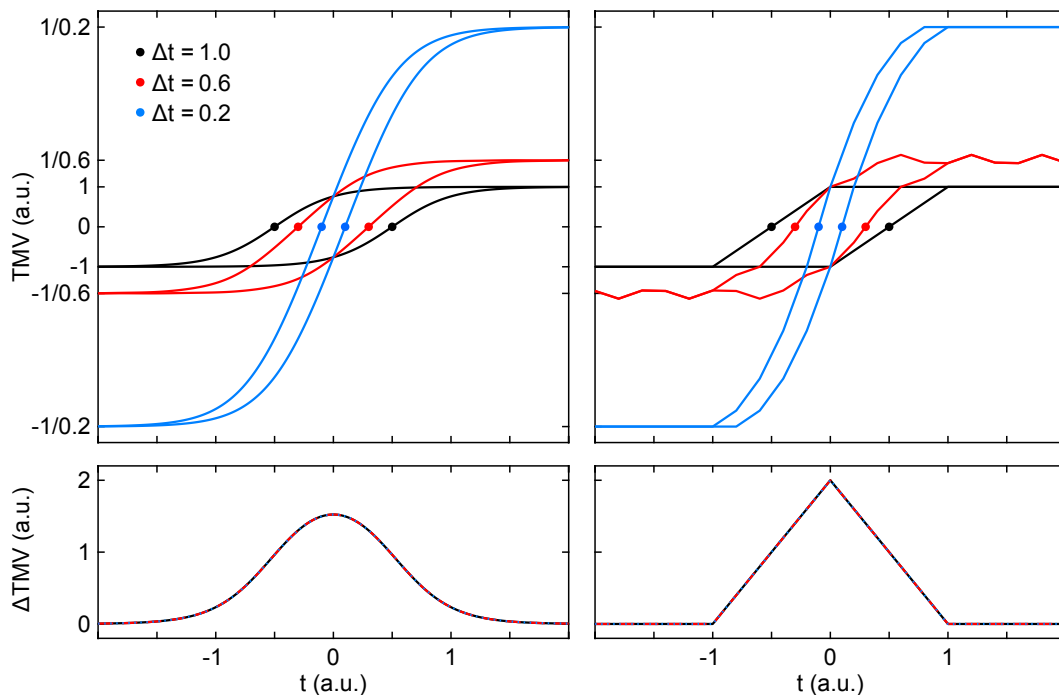
Figure 10.2: Illustration of the reciprocal relation between the TMV amplitude and the time delays Δt for a sigmoid function (*left*) and a piecewise linear function (*right*) as simple representations of the TMV time course.

diagrams on the right demonstrate that this also works for a piecewise linear time course as another example – although it becomes obvious that the waveform might change slightly for a different delay (red curve). Note that the ambiguity between inter-node delays and amplitudes does not only apply to the DR, but is a general property of TMVs, which implies that the absolute values of ATs estimated from TMVs are only meaningful if their amplitude is correct. In practice, we observed that the delays get underestimated and the TMV amplitude gets overestimated during the iterations of DR. To address this problem, either the slope of the TMVs can be constrained (which requires an additional λ) or the delays in each iteration can be scaled by a factor > 1.

In this thesis, the delays were scaled by a factor of 1.05. As the delays can become too large throughout the iterations, we identified the iteration with minimal $\|\mathbf{D\bar{x}}\|_2$ as "optimal" iteration and used the corresponding solution. The node pairs were defined as nodes with a distance of 2 edge lengths. For heart meshes with about 2000 nodes, as used in this thesis, this corresponds to a distance of about 12 mm. The node pair distance should not be chosen too small to avoid round-off errors in the integer-valued delays. For a distance of 12 mm and a CV of 0.6 m/s, the maximum round-off error is 5 % of the sampling period.

10.1.4 Exemplary Results

Fig. 10.3 shows exemplary reconstruction results for a simulated pacing at the RV septum. These results were obtained without periodic boundary conditions. Throughout the iterations, the spot with minimal AT gradually moves from the RV anterior wall onto the septum. The time courses for iteration 1 (second-order Tikhonov regularization) do not resemble an action potential, include multiple ambiguous deflections and include a lot of noise. Throughout the iterations, the time courses become cleaner and an action potential waveform with only one deflection representing depolarization is recovered. In this case, $\|\mathbf{D\bar{x}}\|_2$ was minimal at iteration 40. Note that no specific time course but only similarity between nearby nodes is assumed.

An open-source implementation of DR is provided[1].

---

[1]https://github.com/CECGImaging/DelayBasedRegularization
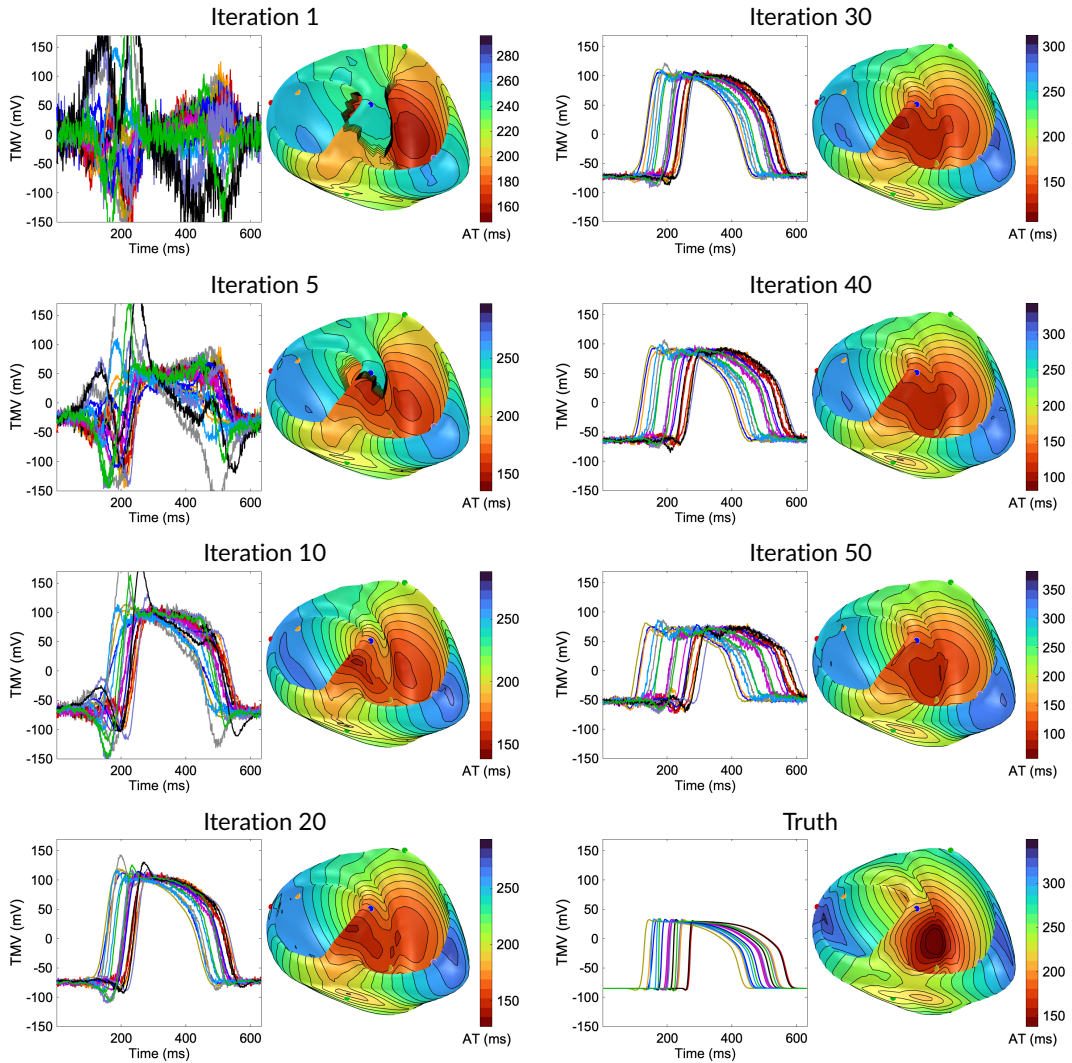
Figure 10.3: Exemplary reconstruction using DR for a simulated pacing at the RV septum (anisotropic excitation model; inhomogeneous torso model for forward and inverse calculations; SNR = 20 dB); node pair distance = 2 edges; spatio-temporal activation time estimation with $\sigma = 20\,\mathrm{ms}$.

10.2 Body Surface Potential Regression (BR)

The body surface potential regression (BR) was introduced in [66], where it was applied to ectopic activity in the atria. In [67], it was first applied to ventricular activity. BR performs a regression of the measured BSPs in terms of spatio-temporal BSP basis vectors determined from simulations of focal activities. The solution in source space is then expressed using TMV basis vectors corresponding to the BSP basis vectors.

10.2.1 Generation of Basis Vectors

As in [68], we use the SVD to generate basis vectors. In order to get a spatio-temporal basis, we define an observation as the column-wise concatenation of values at all nodes for all time steps within a time window of length L. As we do not know the time delay between the activity to be reconstructed and the activities used to create the basis, we include all possible delays by continuously time-shifting the window by a single time step. This way, a total of $K-L+1$ observations are generated for each simulation, where K is the total number of time steps. Row-wise concatenation of all observations (all time shifts of all simulations) then yields a data matrix $\mathbf{D}$. Using $\mathbf{x}_k$ to denote TMVs for all nodes at a time step k, the TMV data matrix $\mathbf{D_x}$ is thus given as:

$$
\mathbf{D_x} = \begin{bmatrix} \begin{pmatrix} \mathbf{x}_1^\mathsf{T} & \mathbf{x}_2^\mathsf{T} & \cdots & \mathbf{x}_L^\mathsf{T} \\ \mathbf{x}_2^\mathsf{T} & \mathbf{x}_3^\mathsf{T} & \cdots & \mathbf{x}_{L+1}^\mathsf{T} \\ \vdots & \vdots & & \vdots \\ \mathbf{x}_{K-L+1}^\mathsf{T} & \mathbf{x}_{K-L+2}^\mathsf{T} & \cdots & \mathbf{x}_K^\mathsf{T} \end{pmatrix} \\ \vdots \\ \text{(repeat for all simulations)} \end{bmatrix} \tag{10.8}
$$

To include the full beginning and end of excitations, the simulated TMVs are padded by repeating their border elements $\frac{L-1}{2}$ times before insertion into the data matrix. By replacing $\mathbf{x}$ with $\mathbf{b}$, a BSP data matrix $\mathbf{D_b}$ can be constructed in exactly the same way. From $\mathbf{A}\mathbf{x}_k = \mathbf{b}_k$, it follows that the whole TMV data matrix can be forward calculated using a block diagonal transfer matrix $\widetilde{\mathbf{A}}$:

$$
\widetilde{\mathbf{A}}\,\mathbf{D_x^\mathsf{T}} = \mathbf{D_b^\mathsf{T}} \quad \Leftrightarrow \quad \mathbf{D_b} = \mathbf{D_x}\,\widetilde{\mathbf{A}}^\mathsf{T} \quad \text{with} \quad \widetilde{\mathbf{A}} = \mathbf{I}_L \otimes \mathbf{A} \tag{10.9}
$$

$\mathbf{I}_L$ is the $L \times L$ identity matrix and $\otimes$ denotes the Kronecker product.
We now perform an SVD of the BSP data matrix:

$$
\mathbf{D_b} = \mathbf{U}\mathbf{S}\mathbf{V_b^\mathsf{T}} \tag{10.10}
$$

The columns of $\mathbf{V_b}$ are spatio-temporal basis vectors of BSPs. We now want to find the corresponding TMV basis vectors $\mathbf{V_x}$, for which holds:

$$
\mathbf{V_b} = \widetilde{\mathbf{A}}\,\mathbf{V_x} \tag{10.11}
$$

Substituting (10.9) and (10.11) in (10.10) yields:

$$
\mathbf{D_x}\,\widetilde{\mathbf{A}}^\mathsf{T} = \mathbf{U}\mathbf{S}\mathbf{V_x^\mathsf{T}}\,\widetilde{\mathbf{A}}^\mathsf{T} \quad \Leftrightarrow \quad \mathbf{V_x^\mathsf{T}} = (\mathbf{U}\mathbf{S})^+ \mathbf{D_x} = \mathbf{S}^+\mathbf{U}^\mathsf{T}\mathbf{D_x} \tag{10.12}
$$

$(\cdot)^+$ denotes the Moore–Penrose pseudoinverse. This shows that the TMV basis can directly be calculated from the TMV data matrix using an inversion of $\mathbf{U}\mathbf{S}$, the scores matrix obtained from the SVD of the BSP data matrix. An inversion of $\widetilde{\mathbf{A}}$ is not required.

10.2.2 Regression in Terms of Basis Vectors

Now the BSPs of a patient show up. They will be called $\mathbf{B} = [\mathbf{b}_1, \mathbf{b}_2, \ldots, \mathbf{b}_K]$ in the following. Here, K is the total number of time steps to be reconstructed. To reconstruct TMVs in terms of a reduced number P of basis vectors, we first perform a least-squares regression using BSP basis vectors. This results in the optimal basis vector weights $\mathbf{W}_r$:[2]

$$\mathbf{W}_r = \arg\min_{\mathbf{W}} \left\| \mathbf{V_b}(:, 1{:}P)\,\mathbf{W} - \widetilde{\mathbf{B}} \right\|_F^2 \tag{10.13}$$

$\|\cdot\|_F$ denotes the Frobenius norm and $\widetilde{\mathbf{B}}$ are the "measured" BSPs reshaped into the format of basis vectors. They are given by:

$$\widetilde{\mathbf{B}}(:, k) = \mathrm{reshape}\big(\mathbf{B}(:, k{:}k{+}L{-}1),\, LM,\, 1\big) \quad \text{for} \quad k = 1, 2, \ldots, K{-}L{+}1 \tag{10.14}$$

Since the columns of $\mathbf{V_b}$ form an orthonormal basis, the solution to (10.13) is given by:

$$\mathbf{W}_r = \mathbf{V_b}(:, 1{:}P)^\top\, \widetilde{\mathbf{B}} \tag{10.15}$$

This can be seen as filtering the BSPs by projecting them onto the P most important BSP basis vectors. The weights $\mathbf{W}_r$ are now used to obtain the reconstructed TMVs $\widetilde{\mathbf{X}}_r$ as linear combination of corresponding TMV basis vectors:

$$\widetilde{\mathbf{X}}_r = \mathbf{V_x}(:, 1{:}P)\,\mathbf{W}_r \tag{10.16}$$

Each column of $\widetilde{\mathbf{X}}_r$ contains the row-wise concatenation of all time windows with length L. As final solution $\mathbf{X}_r$, we therefore extract the central time step of each window:

$$\mathbf{X}_r = \mathbf{V_x}\big(\tfrac{L-1}{2}N{+}(1{:}N),\, 1{:}P\big)\,\mathbf{W}_r \tag{10.17}$$

Corresponding BSPs can be obtained in the same manner:

$$\mathbf{B}_r = \mathbf{V_b}\big(\tfrac{L-1}{2}M{+}(1{:}M),\, 1{:}P\big)\,\mathbf{W}_r = \mathbf{A}\,\mathbf{X}_r \tag{10.18}$$

The main novelties of BR are that the basis vectors are spatio-temporal and that the SVD is applied in BSP space instead of in source space, which leads to an optimal low-rank basis (Eckart-Young theorem) with respect to what can be measured on the body surface. If the basis vectors were created in source space, they may still contain redundant information with respect to BSPs. A second-order Tikhonov constraint may be used for additional regularization, which replaces (10.15) by:

$$\mathbf{W}_r = \arg\min_{\mathbf{W}} \left(\left\| \mathbf{V_b}(:, 1{:}P)\,\mathbf{W} - \widetilde{\mathbf{B}} \right\|_F^2 + \lambda \left\| \mathbf{L}\mathbf{V_x}(:, 1{:}P)\,\mathbf{W} \right\|_F^2 \right) \tag{10.19}$$

Here, the tangential Laplacian is used for $\mathbf{L}$, because the basis vectors already resolve transmural ambiguities.

---

[2]Here, a MATLAB-like notation is used to address matrix elements.

In this thesis, the basis was created from the same simulations also used for the BC method (600 focal excitation simulations per heart). In combination with isotropic excitations, the method will be called BR iso and in combination with anisotropic excitations BR aniso. Using the insights from [66], a length of $L = 71$ ms was chosen. The basis dimension was fixed at $P = 200$, which corresponds to about 95 % of the sum of singular values.

10.3 Deep Learning-Based Localization (DLL)

The deep learning-based localization (DLL) uses a machine learning pipeline consisting of two convolutional neural networks (CNNs) to estimate the position of the excitation origin directly from BSPs and without requiring patient-specific geometries. The BSPs are arranged as image (electrodes × time) and directly used as input to the CNNs. The first CNN predicts the start and end times of activation. The BSPs are then reduced to the predicted activation interval and fed into a second CNN, which predicts the position of the excitation origin by regression of Cobiveco coordinates. Both CNNs use the ResNeXt-50 architecture [69] with input and output layers adapted to the problem [70]. They were trained on about 1,260,000 simulated BSPs from 700 heart models and then directly applied to new simulated and clinical data. Fig. 10.4 (A) gives an overview of the workflow to generate the simulated BSPs. A shape model [40, 41] was used to generate 700 heart models for training, 150 for validation and 150 for testing (Fig. 10.4, B). The heart models were then combined with a torso model and 3 variations of position and orientation within the torso were obtained for each heart (Fig. 10.4, C). 600 focal excitations were simulated for each heart using an eikonal model (Fig. 10.4, D) and forward calculations were performed using BEM. The torso model also included cavitary blood. To make the BSPs more realistic, they were corrupted with WGN as well as recorded muscle artifacts and baseline wander [71]. Then, they were filtered using clinical settings, normalized and arranged in a Cartesian grid for interpolation of the missing values at the armpits (Fig. 10.4, E). The cartesian arrangement of BSPs was then reshaped into a BSP image with the format 224 electrodes × 700 time steps à 1 ms (padding the BSPs at the end). This BSP image is resampled to 350 time steps à 2 ms and used as input to the first CNN. The BSP image is then trunctated to the activation interval predicted by the first CNN and resampled to a fixed length of 125 time steps to obtain the input for the second CNN. The ventricular coordinates predicted by the second CNN describe the anatomical position of the excitation origin. If a patient-specific heart geometry is available, Cobiveco can be computed on this geometry and the predicted ventricular coordinates can be transformed back into Euclidean coordinates describing the absolute position of the excitation origin. To apply DLL to clinical data, only the electrode positions have to be known. The electrodes are projected onto the torso geometry used for training and the measured BSPs are interpolated. To force the second CNN to capture the main characteristics of BSPs, we additionally trained it on BSPs filtered using a spatio-temporal SVD basis comprising 100 basis vectors. This variant is called DLL SVD. SVD filtering is meant to transform the measured BSPs into the space of known input variations. DLL has been developed in collaboration with Nicolas Pilia and in the student theses of Gerald Moik and Maike Rees. For further details, see [70].
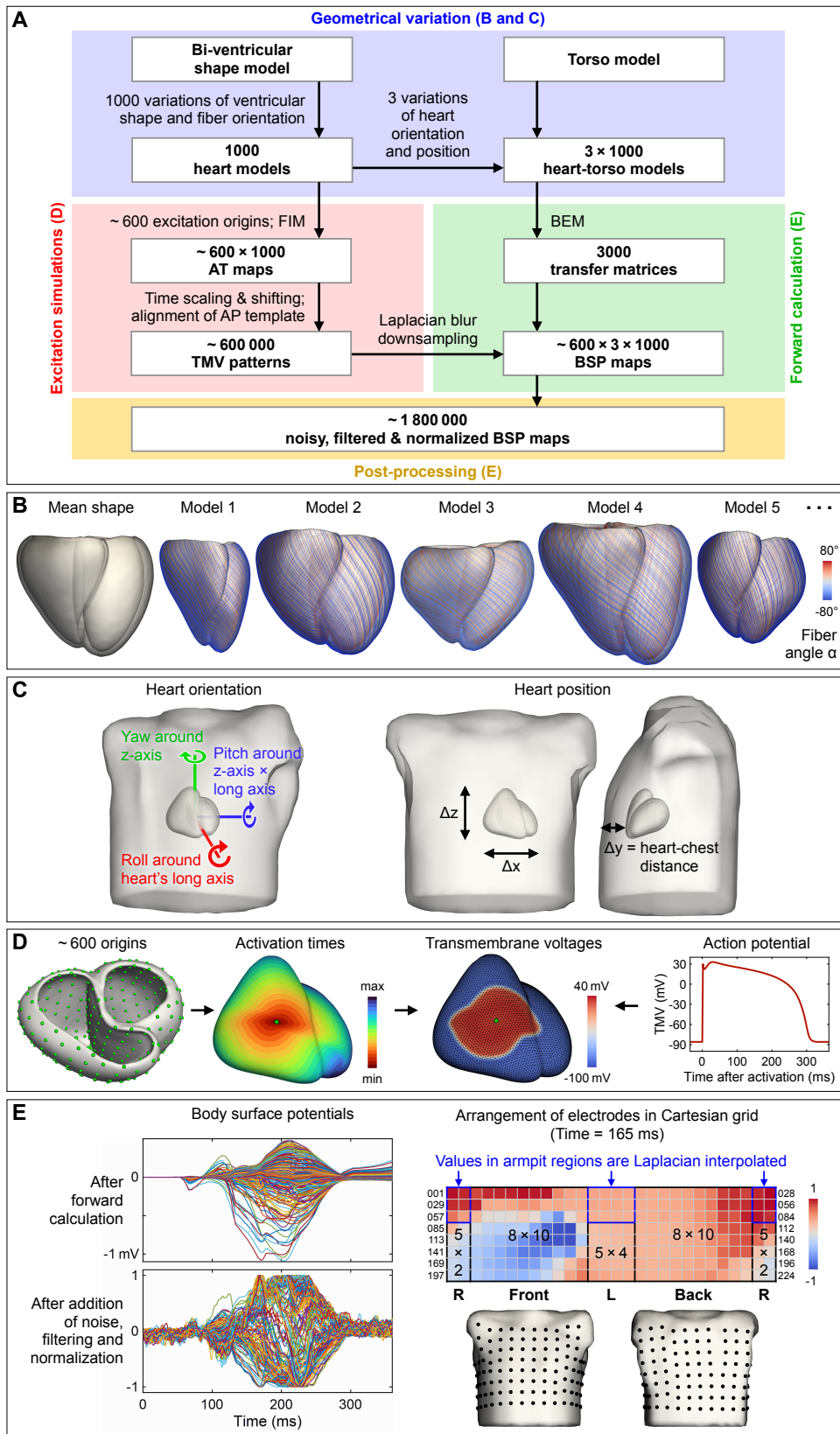
Figure 10.4: Workflow to generate simulated data for DLL (**A**) and illustration of the main steps: Variation of ventricular shape and fiber orientation (**B**), variation of heart orientation and position within the torso (**C**), excitation simulations (**D**), forward calculation and post-processing of BSPs (**E**). Adapted from [70].

Post-Processing

11.1 Baseline Correction of Transmembrane Voltages

As mentioned before, spatially constant components of TMVs do not influence BSPs. For all methods except TND and DR, this means that the baseline of reconstructed TMVs is "floating" over time. To get a meaningful time course of TMVs, we suggest a baseline correction based on spatial statistics [64, 67] as illustrated in Fig. 11.1. If the majority of nodes is not depolarized, a lower percentile computed across space should be a good estimate of the lower bound of TMVs. Similarly, if the majority of nodes is depolarized, an upper percentile should be a good estimate of the upper bound. If half of the nodes are depolarized, the median TMV should lie between the lower and upper bound of TMVs and the median of absolute deviation from this median TMV should be maximal. The median absolute deviation (MAD) therefore represents a robust statistic to detect the central time of depolarization. This depolarization center t_d can then be used to switch between the lower and upper bound for defining the baseline. The same can be done in reverse with respect to the repolarization center t_r. In total, this yields the following baseline signal $g(t)$, which is subtracted from the TMVs:

$$g(t) = \begin{cases} P_{10}[\mathbf{x}(t)] & , \ t < t_d \\ P_{90}[\mathbf{x}(t)] - P_{90}[\mathbf{x}(t_d)] + P_{10}[\mathbf{x}(t_d)] & , \ t_d \leq t < t_r \\ P_{10}[\mathbf{x}(t)] - P_{10}[\mathbf{x}(t_r)] + P_{90}[\mathbf{x}(t_r)] - P_{90}[\mathbf{x}(t_d)] + P_{10}[\mathbf{x}(t_d)] , \ t \geq t_r \end{cases}$$

$$(11.1)$$

with

$$t_d = \arg\max_t \ \mathrm{MAD}[\mathbf{x}(t)]$$

$$t_r = \arg\max_t \ \mathrm{MAD}[\mathbf{x}(t)], \quad t > t_d + 100\,\mathrm{ms}$$

Here, $P_{10}[\cdot]$ and $P_{90}[\cdot]$ denote the 10th and 90th percentile.
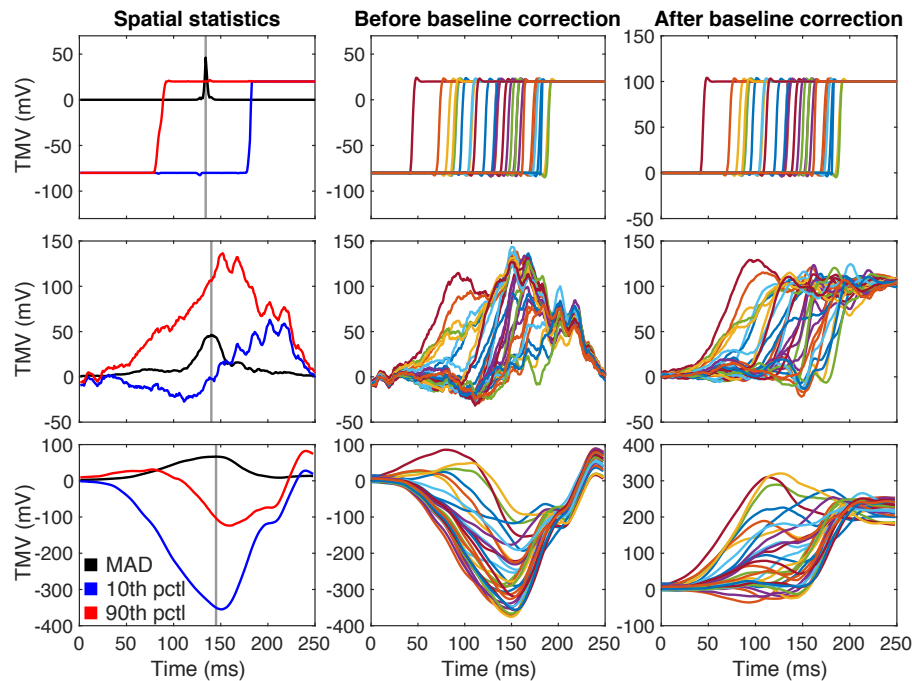
Figure 11.1: Baseline correction of TMVs for an LV pacing (only the depolarization is shown). *Left:* Spatial statistics of TMVs. *Center:* TMVs at 30 points across the ventricles before baseline correction. *Right:* TMVs after baseline correction. *Top-to-bottom:* Simulated truth, reconstruction for the simulation using BR, reconstruction for a clinical case using BR. Adapted from [67] with permission.

11.2 Activation Time Estimation

ATs represent the timing of depolarization and are one of the most important parameters for assessment of abnormalities in the spread of cardiac excitation. In [42], an extensive evaluation of four different AT estimation methods and the related parameters was performed on simulated data. In particular, ATs estimated from EEPs and TMVs reconstructed using second-order Tikhonov regularization were compared regarding line-of-block artifacts, i.e. regions of falsely crowded isochrones in the spatial distribution of ATs. TMVs in combination with sufficient temporal smoothing applied during AT estimation were found to be most robust to line-of-block artifacts. Based on the results in [42], only "deflection-based" AT estimation methods are considered in this thesis:

- Temporal AT estimation (TA): The time where the temporal derivative of TMVs or negated EEPs is maximal is detected (method Defl-T in [42]).

- Spatio-temporal AT estimation (STA): The time where the product of the temporal derivative and the norm of the spatial gradient of TMVs or negated EEPs is maximal is detected [72] (method Defl-ST in [42]).

Before computing the derivatives, the signal is filtered using a zero-phase Gaussian filter (total order: 2) with standard deviation σ. If not stated otherwise, the following values were used in this thesis: $\sigma = 50$ ms for TMVs and $\sigma = 20$ ms for EEPs. For more details, see [42].

11.3 Focus Detection

To detect the excitation origin (focus), the ATs were first smoothed using a tangential Laplacian and a HWHM of 20 mm. To allow a precise localization, the smoothed ATs were then Laplacian interpolated to a three times subdivided version (edge length < 1 mm) of the mesh used for reconstruction (edge length ca. 6 mm) and the minimum was detected as focus.

11.4 Metrics

Two metrics were used to evaluate the reconstruction results in this thesis: The AT correlation and the localization error. The AT correlation is the Pearson correlation coefficient between reconstructed and ground truth ATs. The localization error is defined as the geodesic distance (through the myocardial volume) between the reconstructed and the ground truth excitation origin. The geodesic distance was computed using FIM on a tetrahedralization of the fine surface mesh used for the focus detection in the previous section.

Violin plots will be used to display the metrics. They show the smoothed probability density and statistical measures as explained in Fig. 11.2.
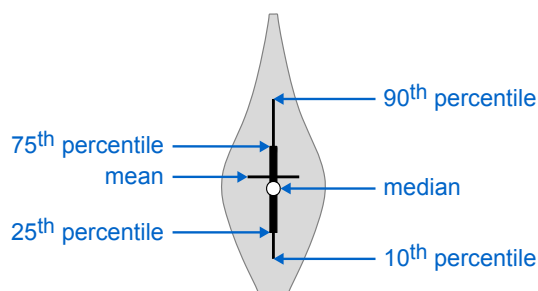
Figure 11.2: Exemplary violin plot with annotation of statistical measures.

EVALUATION

In this part, the inverse methods described in part III will be evaluated on three different datasets: Simulated data, clinical data recorded in CRT patients and clinical data recorded in patients with VT. By comparing the same methods on these different datasets, we aim to draw a comprehensive picture of their performance under idealized and realistic conditions. Simulations have the advantage that all parameters can be controlled and a perfect ground truth is available. They allow to systematically study the impact of different assumptions for the spread of cardiac excitation and the torso model. Inverse methods that already fail in simulations with idealized conditions should not be expected to perform well on clinical data either. On the other hand, simulations may lack realism regarding the complexity of cardiac excitation, conduction properties of the torso and measurement errors occuring in a clinical setting. The drawback of clinical data is that the ground truth is either sparse (e.g. only the excitation origin is known, but not the activation times across the ventricles) or not very reliable (activation times recorded with sequential intracardiac mapping are subject to errors in the localization of the catheter and the time-alignment of multiple beats). Furthermore, clinical BSP measurements are often far from ideal and there are errors in the geometries obtained from tomographic imaging.

In each of the following chapters, one of the three datasets will be introduced and the corresponding results of the inverse problem will be reported and discussed.

Simulated Ventricular Pacings

12.1 Dataset

The simulations used here are the same as in [42]. 137 pacing positions were distributed over the epi- and endocardium (Fig. 12.1) and excitation simulations were performed with an anisotropic ($v = 0.6\,\text{m/s}$, $a = 2.7$) and an isotropic ($v = 0.6\,\text{m/s}$, $a = 1$) eikonal model as described in section 3.6. The fiber orientation is depicted in Fig. 3.2. TMVs were obtained at a sampling rate of 1 kHz by aligning the time course shown in Fig. 12.2 (left) with the ATs. An example of the resulting spatial distribution of TMVs is shown in Fig. 12.2 (right). Forward calculations were performed using BEM and a variant of the torso model in Fig. 6.1 (either inhomogeneous including the heart, cavitary blood, lungs, liver and the rest of the torso or homogeneous including only the heart and the rest of the torso). WGN was added to the BSPs to yield an average SNR of 20 dB (mean over all 200 electrodes during the activation interval).

To study the effect of different modeling and regularization assumptions, four different scenarios were evaluated (Table 12.1). S2–S4 are derived from S1, which uses the most realistic modeling assumptions for the excitation and the forward model and assumes a perfect inverse model. S2 represents a scenario with imperfect inverse model by using a homogeneous torso model for reconstructions. S3 uses a homogeneous torso for both forward and inverse calculations and therefore is similar to the situation in torso tank experiments. S4 uses an isotropic instead of an anisotropic excitation model, which is important to understand the impact of regularization assumptions on inverse solutions.

12.1.1 Choice of Parameters

Individual regularization parameters λ were determined for Tik EEP, Tik and Tik aniso as well as each pacing. Only the QRS interval was taken into account to compute the L-curve. In [42, appendix IV], we found that the L-curve criterion overestimated λ by approximately one decade. As we wanted to get an impression of the performance of methods given good
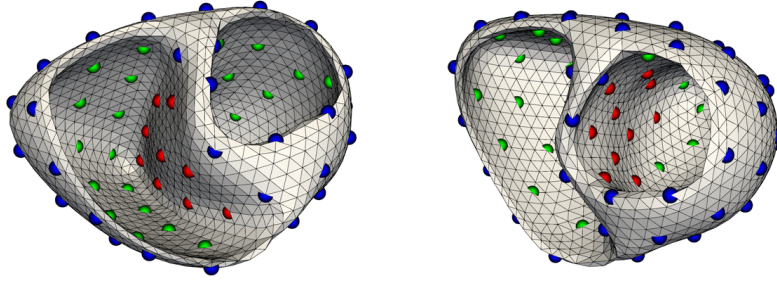
Figure 12.1: 137 pacing positions shown on the heart mesh used for reconstructions (2307 nodes, mean edge length: 6 mm). *Red spheres:* Septal pacing positions. *Green spheres:* Non-septal endocardial pacing positions. *Blue spheres:* Epicardial pacing positions.
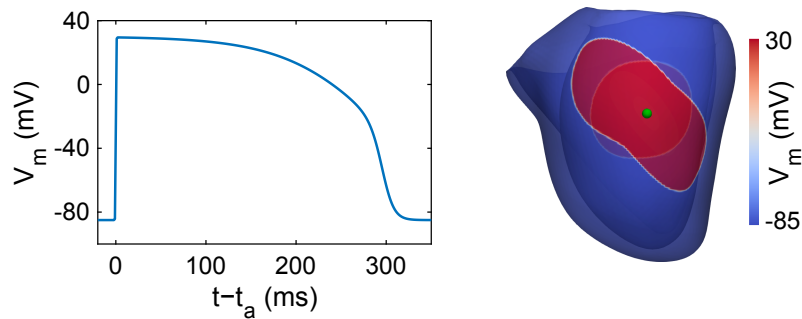
Figure 12.2: *Left:* Time course of TMVs V_m aligned with the ATs t_a. *Right:* Spatial distribution of TMVs 70 ms after pacing at the lateral wall of the LV. Reproduced from [42] with permission.

Table 12.1: Scenarios evaluated in this simulation study. The homogeneous (hom) torso model includes only the heart and the rest of the torso, while the inhomogeneous (inhom) model additionally includes cavitary blood, lungs and the liver. The anisotropic (aniso) excitation model has a 2.7-fold larger CV in fiber direction than across, while the isotropic (iso) model has the same CV in all directions. Deviations from the baseline are highlighted in italic font.

Scenario	S1 (baseline)	S2	S3	S4
Excitation model	aniso	aniso	aniso	*iso*
Forward torso model	inhom	inhom	*hom*	inhom
Inverse torso model	inhom	*hom*	*hom*	inhom

parameters, we therefore decided to decrease the λ resulting from the L-curve criterion by one decade. Table 12.2 lists the resulting median values of λ across all pacings. The same λ as for Tik was used for TND and as initial value $\lambda_{L,1}$ for DR. DR was applied without periodic boundary conditions. For TND, we assumed perfect knowledge of the TMV amplitude by setting the upper bound V_{max} to 115 mV. For TikGS, the values λ_p of the individual components were directly defined by the L-curve criterion. BR was evaluated either without additional second-order Tikhonov constraint ($\lambda = 0$) or using a λ 100 times the value for Tik ($\lambda \neq 0$). This choice worked well on the clinical data in the next chapter and was used here for comparison. For all inverse methods, STA was used to estimate ATs.

Table 12.2: Median values of λ across all pacings for all variants of Tik and all scenarios.

Scenario	S1	S2	S3	S4
Tik EEP	1.4e0	4.3e0	2.5e0	2.1e0
Tik	2.4e-3	5.1e-3	4.0e-3	3.8e-3
Tik aniso	1.9e-4	2.4e-4	2.1e-4	3.2e-4

12.2 Results and Discussion

Fig. 12.3 shows metrics for inverse methods that do not use any simulated data for reconstruction. The activation time correlation is shown on the left and the localization error on the right. The gray violin plot (Rand) represents the mean geodesic distance from each of the excitation origins to all other nodes and therefore reflects the localization error that would result (on average) from a random guess. The red points in each violin plot represent septal pacing positions (red spheres in Fig. 12.1).

For anisotropic excitations, Tik in combination with EEPs performs better than in combination with TMVs – both in terms of activation time correlation and localization error. For an isotropic excitation however (S4), Tik with TMVs performs better. This indicates that for TMVs, the transmural regularization is problematic when the wavefront does not have the same shape on the epi- and endocardium. BSPs are roughly proportional to the difference between the depolarized areas on the epi- and the endocardium (see section 3.4). Therefore, although the transmural ambiguity has to be resolved in some way, forcing transmural similarity also directly destroys a main determinant of BSPs: transmural dissimilarity. For anisotropic excitations, using an anisotropic transmural Laplacian (Tik aniso) can improve the results for TMVs, which confirms that isotropic transmural regularization is problematic. For S1, Tik aniso performs similarly well as Tik EEP (slightly better in terms of AT correlation and slightly worse in terms of the localization error). However, we assumed perfect knowledge of the fiber orientation to construct the anisotropic Laplacian, which is not very realistic. For an isotropic excitation (S4), Tik aniso performs worse than Tik. As the improvement of Tik aniso over Tik also diminishes for an imperfect transfer matrix (S2), we will not consider it for the clinical evaluation. For EEPs, the transmural regularization mainly "copies" the epicardial values to the endocardium where the transfer strength is small. It should be noted that although ATs estimated from EEPs show a slightly higher correlation with the ground truth than ATs estimated from TMVs, they do include more artifacts, which has also been observed in [42]. The activation time correlation mainly captures the global pattern and is relatively insensitive to high-frequency artifacts.

TikGS performs better than Tik if the inverse model is correct (S1, S3 and S4), but worse if it is not (S2). This is caused by suboptimal λs for the 7 individual components, which are hard to determine when the L-curve becomes flatter due to a model mismatch (see Fig. 4.2).

TND performs better than Tik, in particular for the septal pacings (red dots), which indicates that the temporal non-decreasing constraint indeed helps to resolve ambiguities

between the septum and other regions. However, TND was provided with optimal bounds, which cannot be guaranteed in practice.

DR yields the best results for all scenarios and both metrics. However, there are still a few outliers above 30 mm for S1 and the performance decreases further for S2.

For all methods, results improve compared to S1 with either a homogeneous forward model (S3) or an isotropic excitation (S4). However, septal pacings remain difficult for Tik and TikGS even for these two "easy" scenarios.

Fig 12.4 shows metrics for inverse methods using simulated data for reconstruction.

For all scenarios, BR with an additional second-order Tikhonov constraint ($\lambda \neq 0$) leads to worse results than without such a constraint ($\lambda = 0$), especially for septal pacings. Results are best if the type of excitation used to create the basis fits to the type of excitation to be reconstructed. However, BR aniso still performs reasonably well for S4, while BR iso leads to much worse results than BR aniso for S1.

BC is most robust with respect to a mismatch in torso models (S2) and yields almost perfect localization errors for S1 and S3. As the same excitation model has been used to create the BSPs for correlation and the BSPs to be reconstructed, this has to be expected. However, if there is a mismatch in excitation models (S4), the errors are larger than for BR aniso. This indicates that the basis vectors used for BR generalize to some extend from the individual excitations used for basis generation, making it more robust to wrong assumptions in the excitation model than BC.

DLL was only evaluated for S1, where it led to excellent localization errors (both with and without additional SVD filtering). We would like to point out that although the results for DLL are shown under S1, there is actually a mismatch in torso models, because the training data was created using a torso model with only cavitary blood and did not include lungs nor the liver. Furthermore, the CNNs have never seen a BSP from the heart geometry used to create the BSPs to be reconstructed nor has this geometry been derived from the SSM used to create the training data. This demonstrates that in principle, the excitation origin can be localized from BSPs without the need for a patient-specific heart geometry. However, the torso geometry used for training and for creating the data to be reconstructed are the same and thus no error due to projection of the electrodes and interpolation of the BSPs is included in this evaluation.
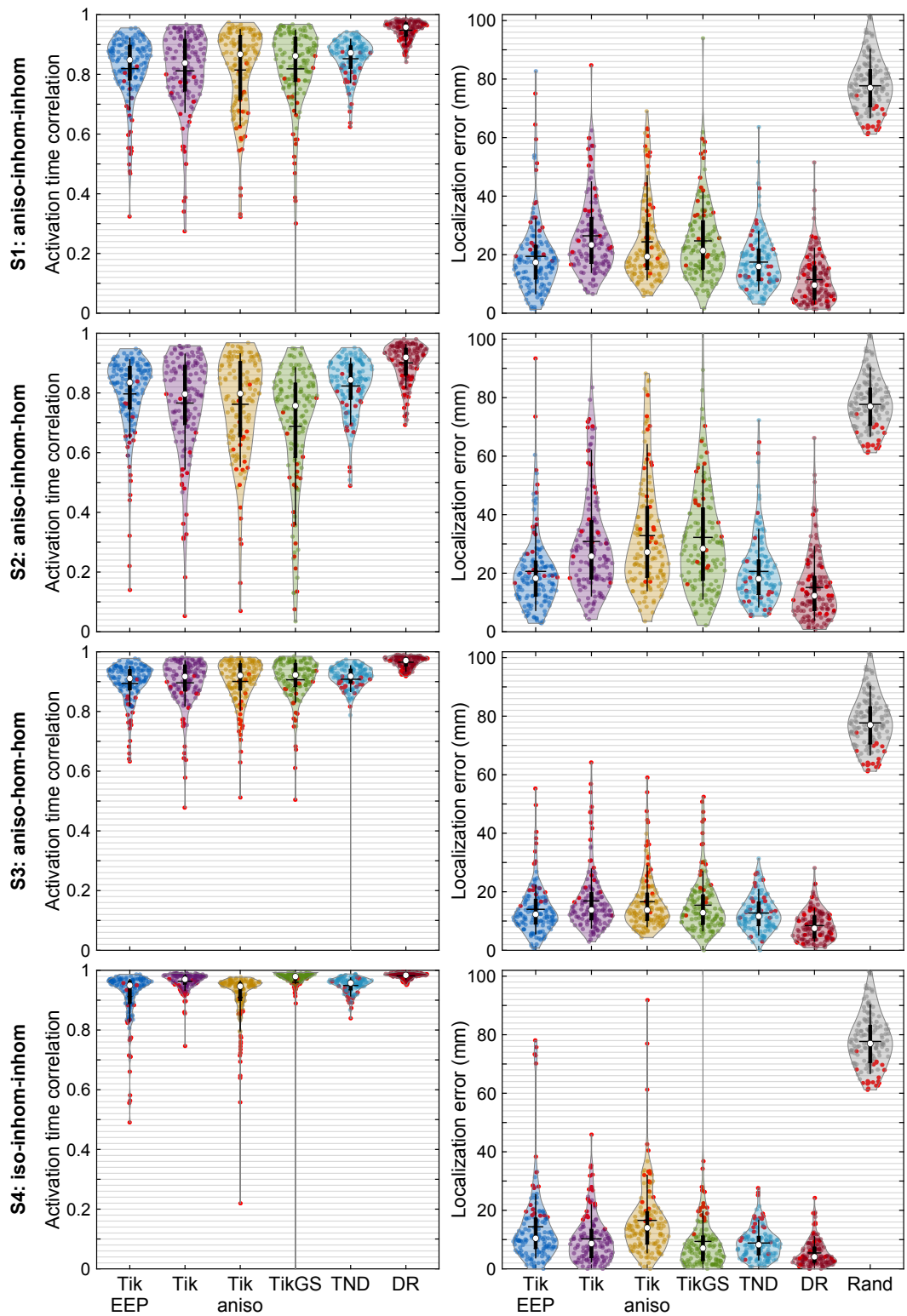
Figure 12.3: Statistics for inverse methods not using any simulated data. *Left*: Activation time correlations. *Right*: Localization errors. STA has been used for all methods.
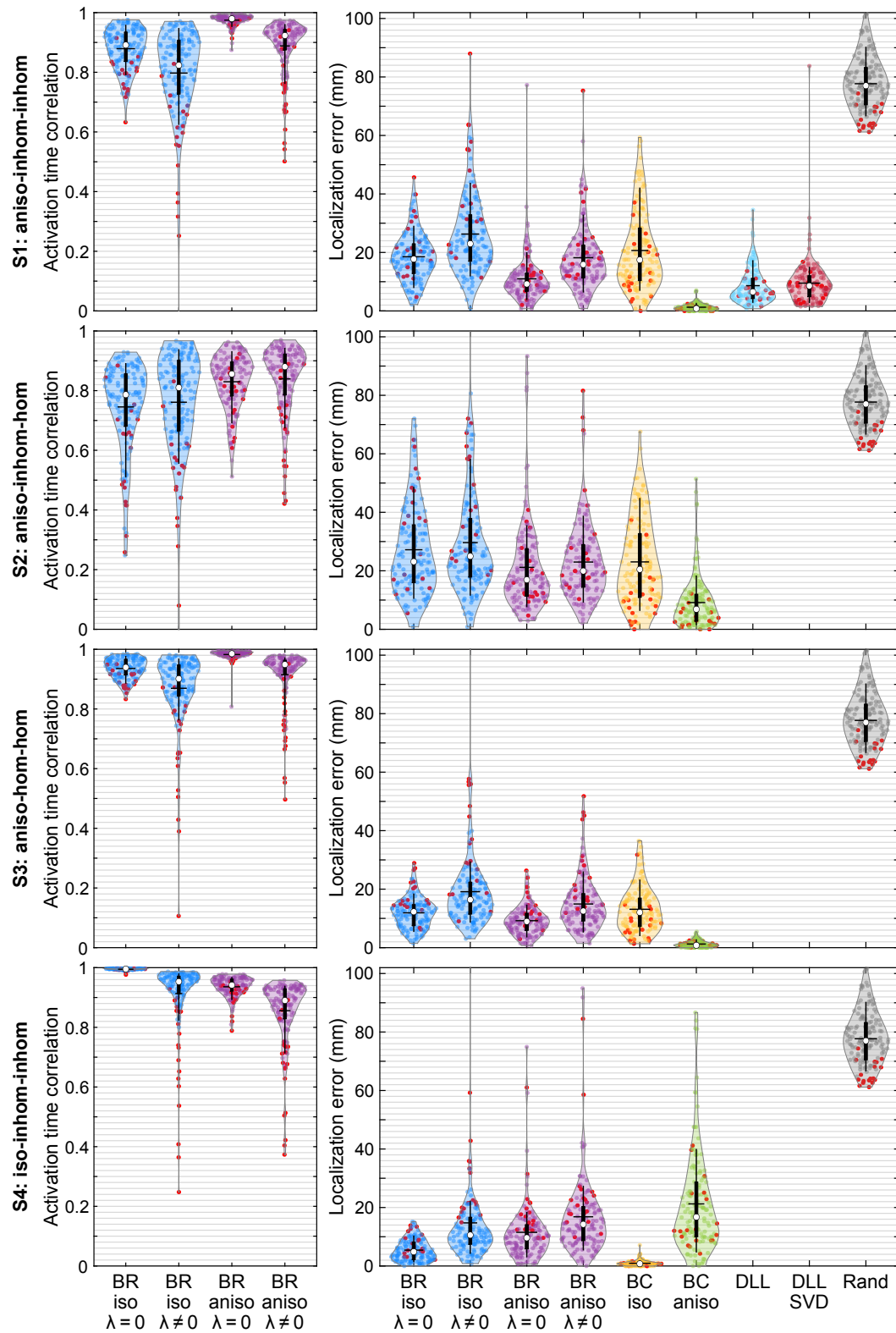
Figure 12.4: Statistics for inverse methods based on simulated data. *Left*: Activation time correlations. *Right*: Localization errors. STA has been used for BR.

Cardiac Resynchronization Therapy Patients

13.1 Dataset

This dataset comprises recordings from 37 CRT patients with implanted biventricular pacemakers. It was acquired in clinical studies [73, 74] at the Almazov National Medical Research Center in Saint Petersburg (Russia). These studies adhered to the Declaration of Helsinki and were approved by the local institutional review board. Written informed consent was obtained from each patient. CT images of the torso and the heart were obtained from each patient and segmented with the software of the Amycard 01C EP system (EP Solutions SA, Yverdon-les-Bains, Switzerland). Triangle meshes of the heart and torso surface as well as positions of the ECG and pacemaker electrodes (also obtained from CT images) were provided by EP Solutions. Heart meshes were remeshed using Instant Meshes [75] to yield a mesh with equally sized triangles and about 2000 nodes. The positions of ECG electrodes were projected onto the torso surface and included as nodes in the mesh. Cavitary blood was added to the torso model by extracting the endocardial surface and closing it at the base. Lungs were only available for a few patients and were thus omitted for all patients. Fig. 13.1 shows torso models for 3 exemplary patients. For most of the 37 patients, BSP recordings of two isolated pacings from different pacemaker electrodes were available: One from an electrode placed at the epicardial side of the LV (30 cases) and one from an electrode placed at the endocardial side of the RV (37 cases). Therefore, this dataset includes a total of 67 pacings. As the electrodes of a biventricular pacemaker are usually implanted at predefined anatomical locations, a clustering can be observed for the pacing positions. Fig. 13.2 illustrates the distribution of pacing positions across the heart.

Patient 11   Patient 13   Patient 15
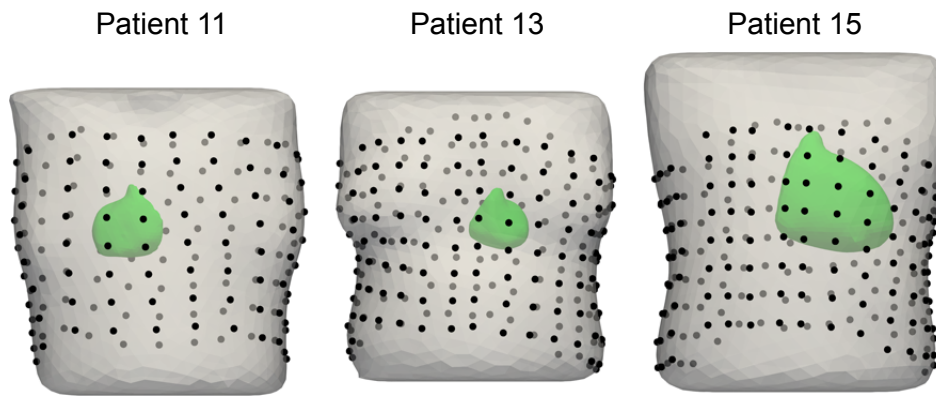
Figure 13.1: Torso models for three exemplary patients. Note the different heart sizes. Patient 11 has dextrocardia. Back dots represent ECG electrodes.
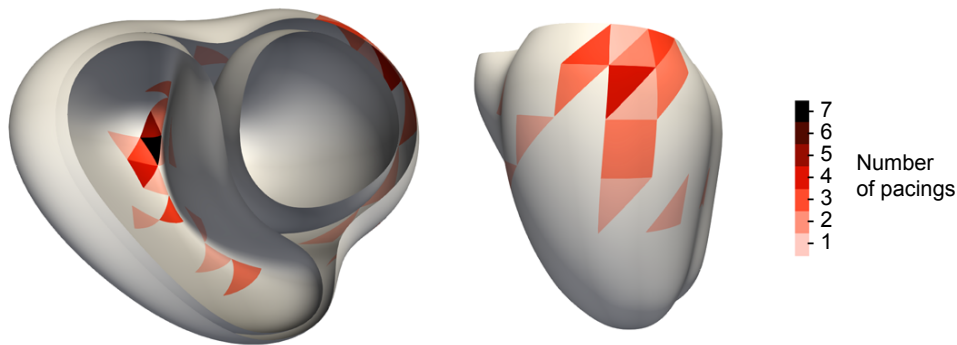
Figure 13.2: Number of pacings in different regions of the heart. Cobiveco was used to transfer the individual pacing positions from the patient geometries to the mean shape of an SSM [41] and a coarse triangle mesh was used for binning.

13.1.1 Pre-Processing of BSPs and Choice of Parameters

To detect bad leads, the BSPs were filtered using the left singular vectors of the transfer matrix corresponding to 90 % of the singular values. An electrode was excluded if the rRMSE between the filtered BSPs and the original BSPs exceeded 50 % or the corresponding correlation coefficient was below 0.9. The remaining unfiltered BSPs were used for reconstructions. Fig. 13.3 shows the number of electrodes for all patients after bad lead removal. A fourth-order Butterworth high-pass filter with a cutoff frequency of 0.5 Hz was applied to remove baseline wander [76].

As the L-curve for some cases was very flat and did not yield a reliable λ, we used the median resulting from the L-curve criterion across all patients. To take the different numbers of cardiac nodes and electrodes for each patient in to account, the median was computed for

a normalized λ' and was then de-normalized for each patient:

$$\lambda' = \lambda \, \frac{\text{number of cardiac nodes}}{\text{number of electrodes}} \qquad (13.1)$$

This resulted in a λ' of 1.0e2 for Tik EEP and 1.5e-1 for Tik. For TND, we tested upper bounds of 100 mV, 200 mV and 300 mV and chose $V_{max} = 200$ mV, as it performed best. All other parameters were chosen analogously to section 12.1.1. For this dataset, both TA and STA were evaluated for AT estimation.
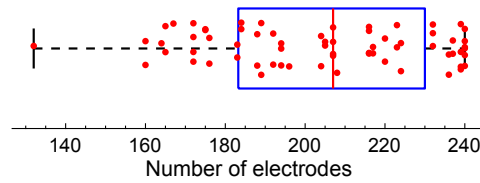
Figure 13.3: Number of electrodes for all 37 patients after bad lead removal.

13.2 Results and Discussion

Fig. 13.4 shows the localization errors resulting with the best AT estimation method selected for each inverse method. The corresponding median and quartiles are listed in Table 13.1. BR aniso performed best, with a median error of 12.8 mm. In contrast to the simulated data, the "optimal" iteration of DR did not yield good results. Better results could be obtained with solutions at earlier iterations. The solution at iteration 15 led to a similar localization error as TND, which was slightly better than Tik but slightly worse than Tik EEP. Although BR aniso gave better results than BR iso, BC iso performed better than BC aniso. DLL performed poorly compared to the simulated data, but using SVD filtering could reduce the error from 36.4 mm to 32.6 mm. For completeness, the results for the corresponding other AT estimation methods are depicted in Fig. 13.5. Also the results for BR without additional second-order Tikhonov constraint ($\lambda = 0$) and for BC without blurring of the correlation coefficients (HWHM = 0 mm) are included. These configurations performed worse than the corresponding ones in Fig. 13.4, although the opposite was true for the simulated data.

Table 13.1: Medians and quartiles corresponding to Fig. 13.4. The best values are marked in bold.

	Tik EEP	Tik	TND	DR i = 15	DR i = opt	BR iso	BR aniso	BC iso	BC aniso	DLL	DLL SVD
Median (mm)	18.5	24.0	20.0	19.6	24.8	21.1	**12.8**	16.6	26.8	36.4	32.6
1st quartile (mm)	11.1	15.9	11.0	12.8	12.9	14.6	**5.9**	12.6	18.5	22.9	20.2
3rd quartile (mm)	25.8	30.8	26.5	27.7	35.1	27.6	**21.2**	24.1	40.5	47.1	45.6
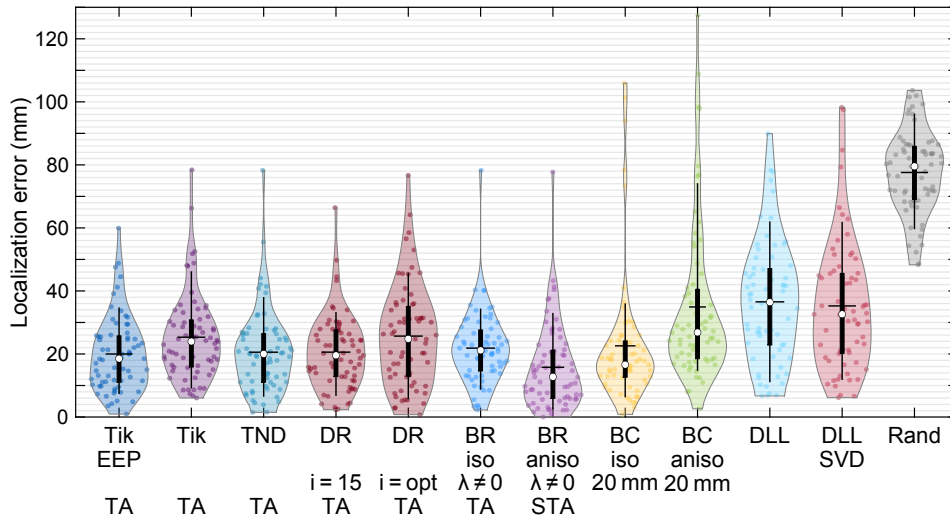
Figure 13.4: Localization errors for the CRT data. Here, the AT estimation method performing best was chosen for each inverse method. 20 mm for BC refers to the HWHM used for smoothing the interpolated correlation values.
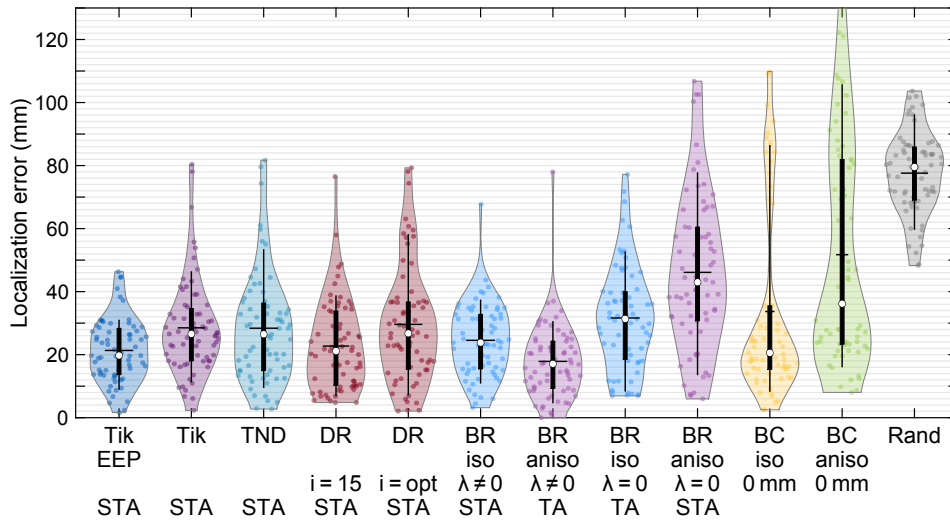
Figure 13.5: As Fig. 13.4 but for the respective other AT estimation method. Also shown is BR without second-order Tikhonov constraint ($\lambda = 0$) and BC with a HWHM of 0 mm.

Ventricular Tachycardia Patients

14.1 Dataset

This dataset comprises 6 patients who underwent intracardiac mapping for ablation of a scar-related VT. The data were acquired at University Medical Centre Mannheim (UMM). BSPs were recorded in a total of 13 cases, but a ground truth (CARTO-recorded ATs) was only available for 10 cases. Out of these, 4 cases were VTs and 6 cases were pacings. Table 14.1 provides an overview of the dataset. The torso models were generated in the same way as for the CRT dataset, but additionally lungs were included.

To compare the inverse reconstructions with the intracardiac mapping data, the CARTO-recorded ATs had to be merged with the tomography-derived geometries used for ECGI. Due to substantial deviations between the shapes of the CARTO-recorded and tomography-derived endocardial surfaces, rigid alignment and nearest-neighbor mapping led to unsatisfactory results. Instead, Cobiveco was utilized to transfer the ATs. Fig. 14.1–14.3 illustrate the results for the 3 excitations of patient 35. Results for all other patients can be found in appendix A. The CARTO ATs were transferred to a twice subdivided version of the ECGI mesh (ca. 1.5 mm edge length). For computation of the activation times correlation, reconstructed ATs were Laplacian interpolated to this subdivided mesh and correlation was performed only across endocardial nodes for which true ATs were available. The true excitation origin was determined by blurring the CARTO ATs using a tangential Laplacian and a HWHM of 5 mm.

Table 14.1: Overview of the VT dataset.

Patient	34			35				38	39			43	44
Imaging	CT			CT				MRI	CT			CT	CT
Num. electrodes	113			174				102	144			157	129
Excitation	LV p.	RV p.	VT	LV p.	RV p.	VT1	VT2	VT	LV p.	RV p.	VT	VT	VT
Num. beats averaged	5	4	5	3	5	7	7	8	4	3	7	7	7
CARTO	yes	yes	no	yes	yes	yes	no	yes	yes	yes	no	yes	yes
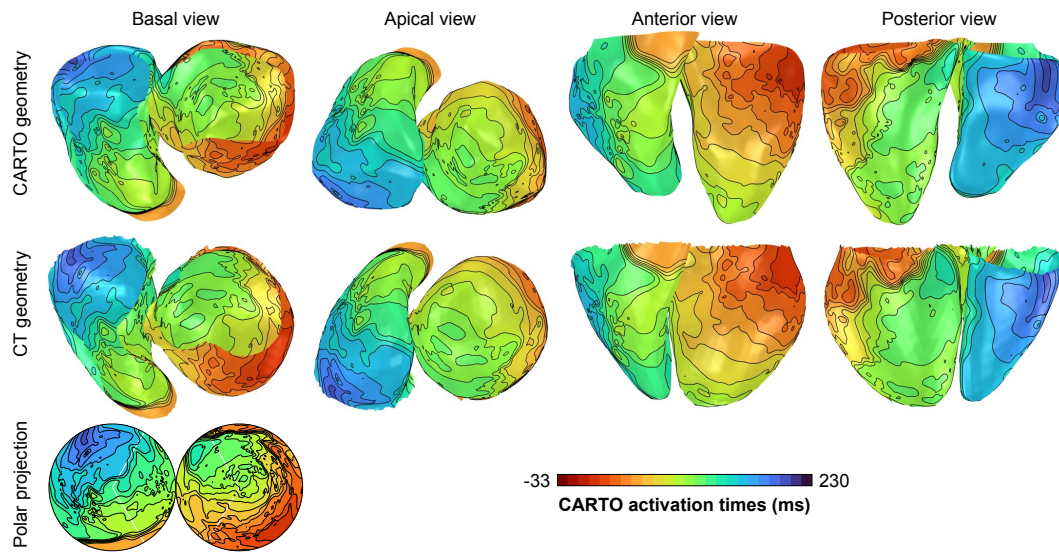
Figure 14.1: CARTO activation times for patient 035, LV pacing. *First row:* Activation times on the corresponding geometry obtained using intracardiac mapping (exported from the CARTO system). *Second row:* Result of transferring the activation times to the tomography-derived geometry using Co-biveco [37]. These activation times served as ground truth for inverse reconstructions. *Third row:* Corresponding polar projection showing the entire endocardial surface without occlusions.
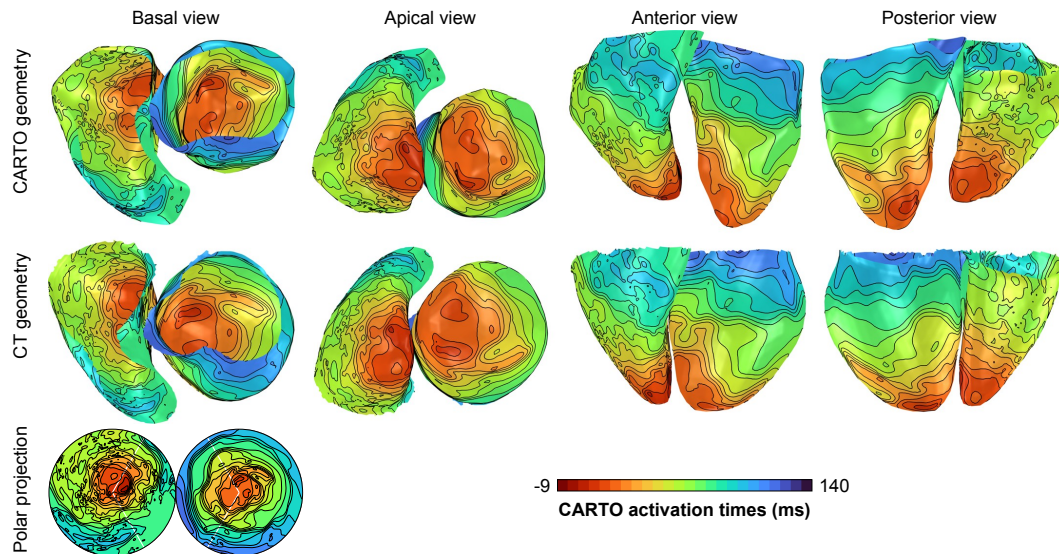
Figure 14.2: CARTO activation times for patient 035, RV pacing.
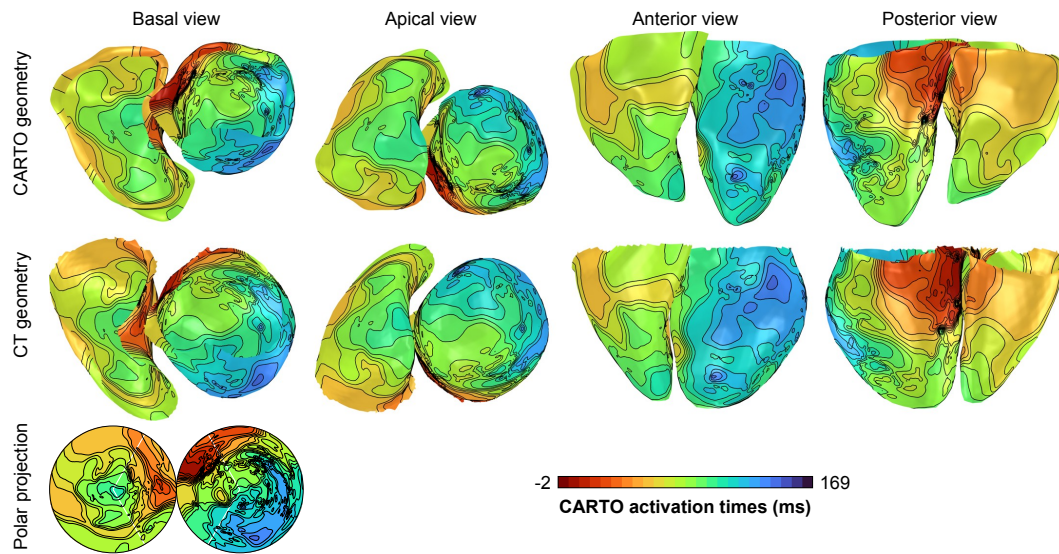
Figure 14.3: CARTO activation times for patient 035, VT1.

14.1.1 Pre-Processing of BSPs and Choice of Parameters

Bad lead detection and high-pass filtering was the same as for the CRT dataset. Individual beats were aligned using the cross-correlation of the derivative of the first temporal singular vector of BSPs and beats sharing a correlation coefficient >0.97 were averaged. The number of electrodes after bad lead removal and the number of beats averaged for each case are given in Table 14.1. λ' was determined as for the CRT dataset, which resulted in values of 1.3e2 for Tik EEP and 2e-1 for Tik. Periodic boundary conditions were used for DR. All other parameters were chosen as for the CRT dataset. Only TA was evaluated for AT estimation.

14.2 Results and Discussion

Table 14.2 lists the activation time correlations. The best median correlation coefficient could be obtained for BR iso, which performed well for all pacings but not for the VTs. For VTs, the best results could be obtained with Tik.

The localization errors are listed in Table 14.3. Here, BR aniso and Tik EEP performed best in terms of the median but Tik resulted in the best localization of VT exit points. DLL failed.

Table 14.2: Activation time correlations for the VT dataset. TA was used for all methods. The best results in each column are marked in bold.

Patient	34		35			38	39		43	44	Median
Excitation	LV p.	RV p.	LV p.	RV p.	VT1	VT	LV p.	RV p.	VT	VT	$(1^{st}–3^{rd}$ quartile)
Tik EEP	0.69	0.52	0.69	0.68	0.69	0.16	0.62	0.65	0.65	0.36	0.65 (0.52 – 0.69)
Tik	0.83	0.60	0.92	0.84	**0.83**	0.18	0.77	0.75	**0.76**	0.67	0.76 (0.67 – 0.83)
TND	0.91	0.70	0.92	0.88	0.69	0.15	0.76	0.77	0.48	0.64	0.73 (0.64 – 0.88)
DR i = 15	0.80	0.65	0.86	0.83	0.78	0.15	0.68	0.76	0.53	0.61	0.72 (0.61 – 0.80)
BR iso $\lambda \neq 0$	**0.92**	0.67	**0.94**	0.89	0.76	0.18	**0.85**	**0.82**	0.23	**0.72**	**0.79** (0.67 – 0.89)
BR aniso $\lambda \neq 0$	0.86	**0.77**	0.91	**0.91**	0.62	**0.37**	0.69	0.81	0.28	0.63	0.73 (0.62 – 0.86)

Table 14.3: Localization errors (mm) for the VT dataset. TA was used for all methods. The best results in each column are marked in bold.

Patient	34		35			38	39		43	44	Median
Excitation	LV p.	RV p.	LV p.	RV p.	VT1	VT	LV p.	RV p.	VT	VT	$(1^{st}–3^{rd}$ quartile)
Tik EEP	20.7	16.4	18.3	25.5	37.6	51.6	21.4	21.9	25.9	52.7	23.7 (20.7 – 37.6)
Tik	24.8	13.8	16.0	19.9	**29.9**	83.2	25.3	30.4	**23.0**	41.6	25.0 (19.9 – 30.4)
TND	23.8	10.5	19.6	19.1	32.8	67.8	22.5	32.4	42.6	42.0	28.1 (19.6 – 42.0)
DR i = 15	20.6	15.7	33.1	20.2	39.4	70.6	**15.9**	28.1	47.3	65.7	30.6 (20.2 – 47.3)
BR iso $\lambda \neq 0$	**10.1**	7.1	**3.9**	20.1	46.5	76.7	26.9	26.1	51.5	**26.4**	26.2 (10.1 – 46.5)
BR aniso $\lambda \neq 0$	13.1	19.4	17.6	24.5	64.8	61.4	22.3	**20.6**	60.9	39.4	**23.4** (19.4– 60.9)
BC iso 20 mm	17.3	**6.0**	26.0	**14.6**	31.6	42.0	35.1	23.9	62.0	55.4	28.8 (17.3 – 42.0)
BC aniso 20 mm	22.4	16.4	78.8	22.3	85.8	**40.0**	75.1	57.6	64.5	80.9	61.0 (22.4 – 78.8)
DLL SVD	110.0	9.4	89.5	20.1	63.9	59.4	53.2	50.4	108.7	91.3	61.6 (50.4 – 91.3)

FINAL REMARKS

Chapter **15**

Discussion

Our results show a substantial discrepancy between simulated and clinical data. While sophisticated methods like TND and DR performed well on simulated data, they did not lead to clear improvements on clinical data. We suspect that this is caused by a larger error in the torso model for the clinical data. When large errors in the torso model are present, also correct assumptions about the sources might impair the solution. Tikhonov regularization makes the least specific assumptions and tolerates model inaccuracies, whereas more specific assumptions might translate these inaccuracies more directly into the sources. On the other hand, specific assumptions are required to resolve ambiguities in the inverse problem.

Changes in the position and orientation of the heart within the torso are known to have a large impact on BSPs [77–79] and are a potential source for errors in solutions to the inverse problem. Optimizing the heart position [80–82] might improve the results for clinical data. Although some studies have concluded that simple torso models are sufficient for ECGI in a clinical setting [83], more recent closed-chest animal experiments [84, 85] suggest that torso inhomogeneities are important. Our simulation study in chapter 12 also showed that using a simpler torso model for the inverse than for the forward problem has a detrimental effect on reconstructions. In this work, the anisotropy of myocardial conductivies was neglected. Another important factor affecting the forward model might be anisotropic sceletal muscle [86, 87]. Even if all major torso compartments are taken into account, segmentation inaccuracies [88, 89] can lead to errors in the transfer matrix. Furthermore, the conductivies may vary substantially between patients.

Chapter **16**

Conclusion

In this thesis, ECGI was formulated in terms of two different representations of the cardiac sources on the surface of the myocardium: TMVs and EEPs. New approaches to analyze the relation between these surface sources and the potentials on the body surface were introduced and revealed differences between the two source representations with important consequences for the inverse problem. For EEPs, only values on the epicardium and a small part of the basal endocardium were found to have a strong relation to BSPs, which makes this source representation inadequate for reconstruction of endocardial activity. For TMVs, also the endocardium showed large transfer strengths. However, this comes at the price of ambiguous transfer coefficients between the epi- and the endocardium and requires transmural and/or temporal regularization. While transmural regularization can address ambiguities between both sides of the free walls, it cannot resolve ambiguities between the septal endocardium and the free walls. Only temporal regularization has the potential to resolve the latter. Both transmural and temporal regularization introduce additional assumptions about the cardiac sources, which may or may not be appropriate for certain activities to be reconstructed. Restricting oneself to reconstruct a representation of the sources on only the epicardium (either EEPs on the epicardium plus a small part of the basal endocardium or PPs on the epicardium plus a cap closing the surface at the base) makes these additional assumptions unnecessary – although they may still help to stabilize the solution. However, the reconstructed EPs on the epicardium will also include endocardial activity, which complicates their interpretation needed to arrive at diagnostically relevant information like ATs.

After analyzing the forward problem and introducing new operators for transmural regularization, two novel inverse methods incorporating spatio-temporal prior knowledge into ECGI were introduced: DR uses explicit constraints, while BR uses simulated data to constrain the solution. Furthermore, a deep learning method (DLL) to localize the excitation origin directly from BSPs was presented, which was only trained on simulated data and does not require patient-specific geometries. The three new methods were applied to a simulated and two clinical datasets and compared with four state-of-the-art methods. While DR and DLL performed best on the simulated dataset, BR using a basis created from anisotropic excitations performed best on the CRT dataset. On the data recorded in VT patients, however, none of the novel methods could bring an improvement compared to Tik. We conclude that

DR only works well if the torso model is accurate, BR only if the excitations used to create the basis fit to the activity to be reconstructed and Tik still works best for irregular activity in deseased hearts, as it makes the least specific assumptions.

Outlook

To explain the discrepancy between the results for simulated and clinical data, systematic experimental studies are necessary in order to identify factors compromising the validity of the torso model as well as the validity of assumptions about the cardiac activity made during regularization. Closed-chest experiments are required for the former, while experiments with isolated hearts or torso tanks can be used for the latter.

Regarding the proposed methods to solve the inverse problem, the following advancements or extensions could be made:

- The delay-based regularization could be extended to ...
  - start with strong temporal smoothing for AT estimation (large σ) and decrease it throughout the iterations in order to increase the robustness of AT estimation while the TMV time courses have ambiguous deflections and allowing a more precise AT estimation when the deflections in the TMV time courses become unique during later iterations.
  - use separately estimated activation and repolarization times for time alignment, with a linear transition between the corresponding delays for intermediate time steps (during the plateau phase and the beginning of repolarization).
  - perform a coupled reconstruction of multiple or even different beats by imposing similarity not only between time-aligned TMVs of nearby nodes within the same beat but also between time-aligned TMVs of the same nodes across beats.

- The body surface potential regression could be extended to ...
  - include excitation simulations using many different fiber orientations and CVs to reflect the uncertainty in these parameters.

- The deep learning-based localization may be improved by ...
  - a network architecture using a low-dimensional latent representation, as suggested in [90, 91].
  - including multiple torso geometries and variations of the organ conductivites in the synthetic training data.
  - including local variations in CV for the excitation simulations.

○ additional training on clinical data or utilizing domain adaptation to address the discrepancy between simulated and clinical data [92].

Finally, a few general ideas for future directions are suggested:

- The anisotropic Laplacian may be used to tune the strength of transmural regularization by defining fibers in transmural direction and adjusting the anisotropy ratio.

- A local weighting of regularization [93] based on the local transfer strength may be used to reduce biases towards regions with large transfer strengths, see also [94]. In Tikhonov regularization of TMVs, for example, the ambiguity between the septum and the RV anterior wall usually leads to a reconstruction of septal activity on the RV anterior wall, because there the transfer strength is larger than on the septum and thus the same residual norm can be reached with a smaller magnitude of sources and thus with a smaller solution norm.

- Systematically perturbing the local weighting of regularization may be one way to assess uncertainties in inverse solutions arising due to ambiguities.

Appendix 1
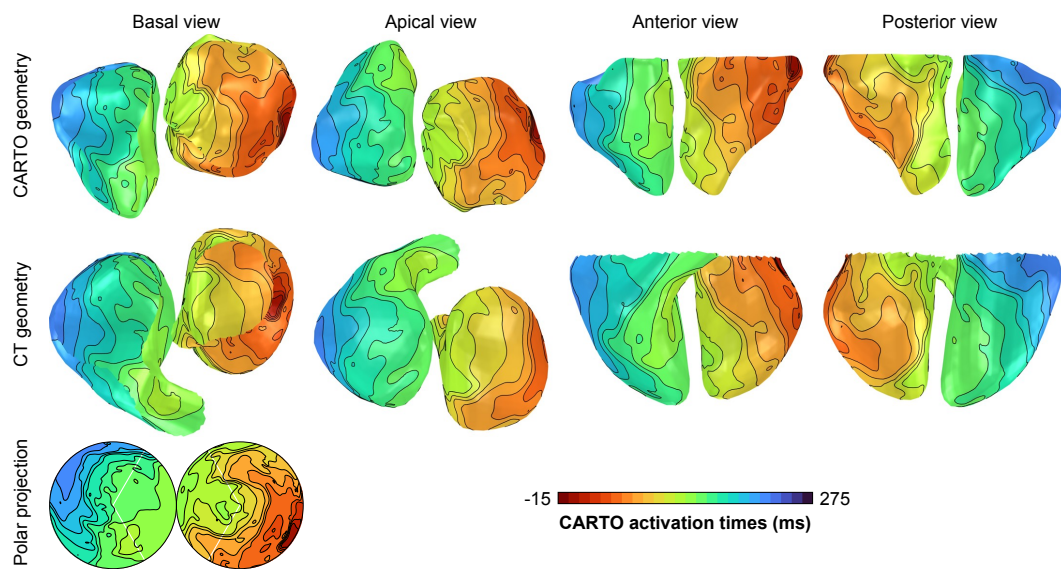
Figure A.1: CARTO activation times for patient 034, LV pacing.
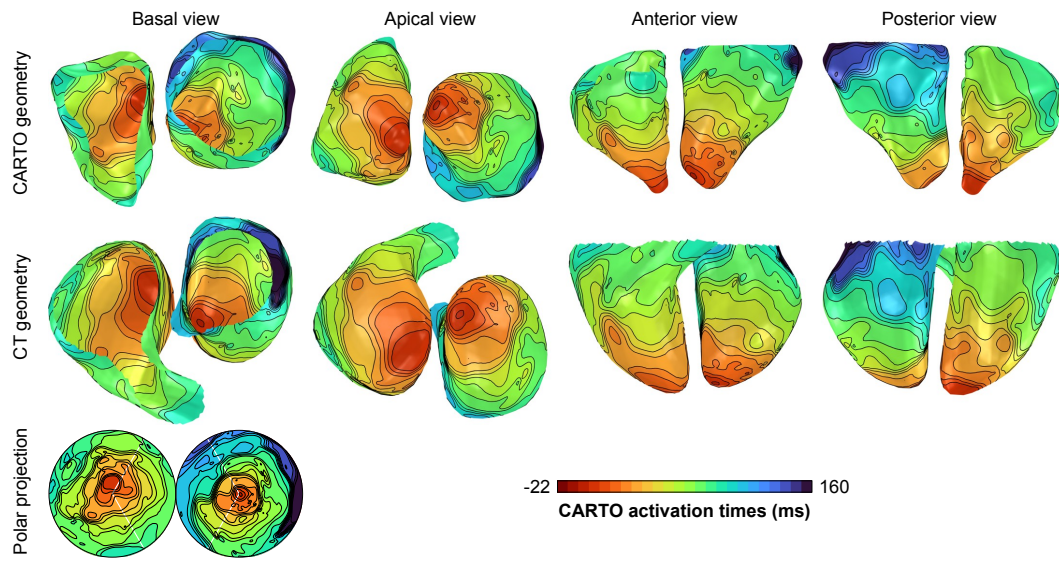
Figure A.2: CARTO activation times for patient 034, RV pacing.
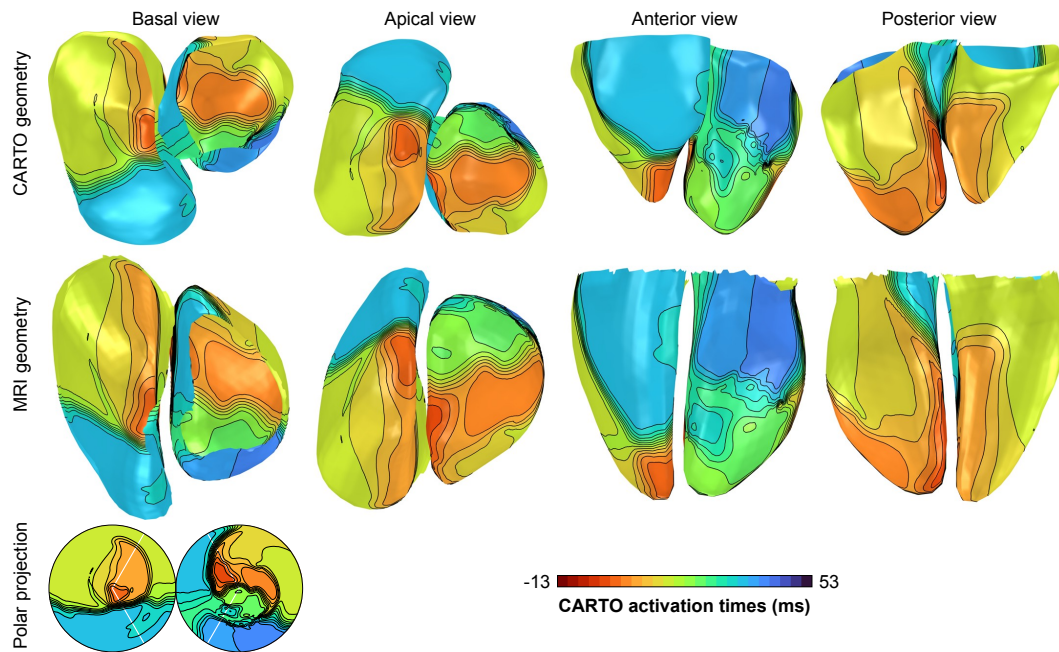
Figure A.3: CARTO activation times for patient 038, VT.
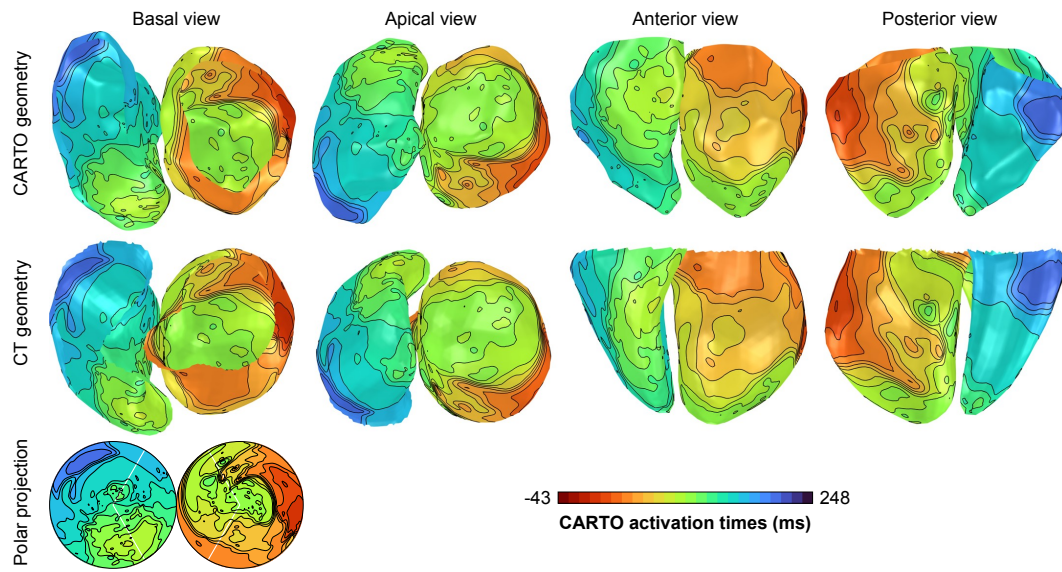
Figure A.4: CARTO activation times for patient 039, LV pacing.
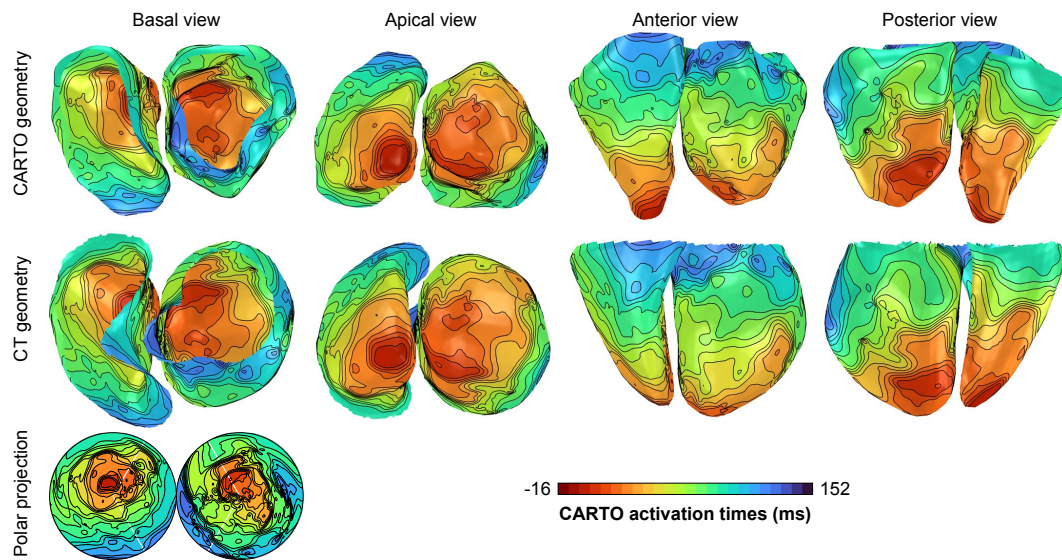
Figure A.5: CARTO activation times for patient 039, RV pacing.
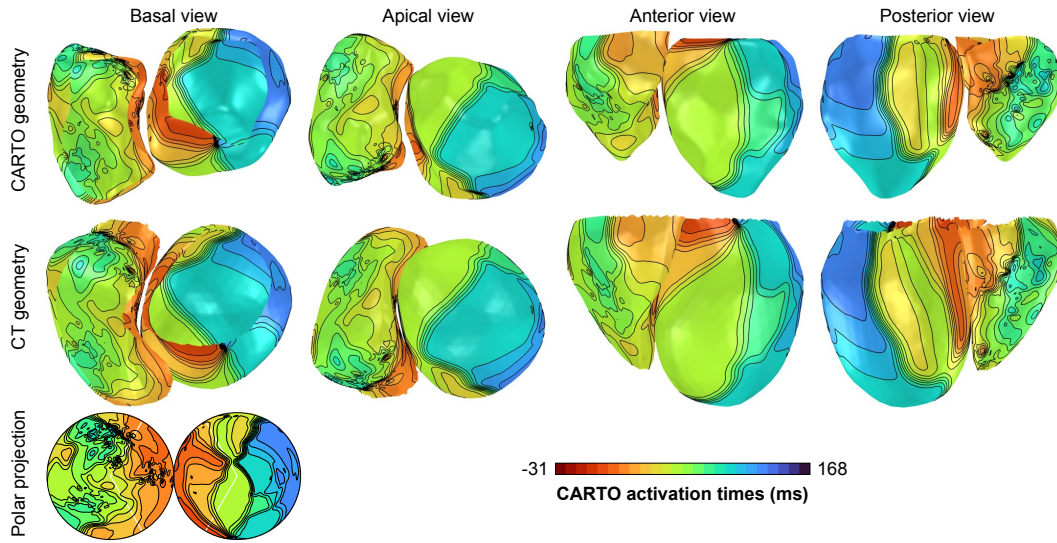
Figure A.6: CARTO activation times for patient 043, VT.
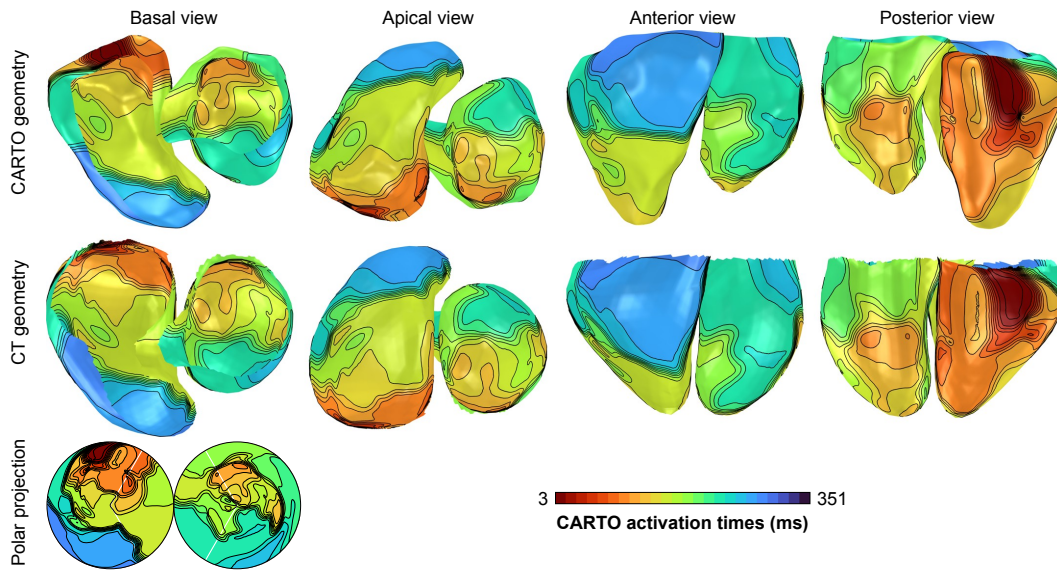
Figure A.7: CARTO activation times for patient 044, VT pacing.

References

[1] J. G. Betts, K. A. Young, J. A. Wise, et al., *Anatomy & Physiology (OpenStax version July 15, 2021)*. Rice University, 2013. https://openstax.org/books/anatomy-and-physiology/pages/1-introduction

[2] P. W. Macfarlane, "Lead systems," in *Comprehensive Electrocardiology*. Springer, 2010, pp. 375–425. doi:10.1007/978-1-84882-046-3_11

[3] B. Taccardi, B. B. Punske, R. L. Lux, et al., "Useful lessons from body surface mapping," *J Cardiovasc Electrophysiol*, vol. 9, pp. 773–786, 1998. doi:10.1111/j.1540-8167.1998.tb00965.x

[4] O. Skipa, "Linear inverse problem of electrocardiography: epicardial potentials and transmembrane voltages," PhD thesis, Institute of Biomedical Engineering, Karlsruhe Institute of Technology (KIT), 2004. https://publikationen.bibliothek.kit.edu/1000000039

[5] D. B. Geselowitz, "On bioelectric potentials in an inhomogeneous volume conductor," *Biophys J*, vol. 7, pp. 1–11, 1967. doi:10.1016/S0006-3495(67)86571-8

[6] R. Plonsey and D. B. Heppner, "Considerations of quasi-stationarity in electrophysiological systems," *Bull Math Biophys*, vol. 29, pp. 657–664, 1967. doi:10.1007/BF02476917

[7] L. Tung, "A bi-domain model for describing ischemic myocardial DC potentials," PhD thesis, Massachusetts Institute of Technology (MIT), 1978. http://hdl.handle.net/1721.1/16177

[8] D. B. Geselowitz and T. W. Miller, "A bidomain model for anisotropic cardiac muscle," *Ann Biomed Eng*, vol. 11, pp. 191–206, 1983. doi:10.1007/BF02363286

[9] G. Scharf and C. Scharf, "Electrophysiology of living organs from first principles," *arXiv Biological Physics*, 2010, arxiv:1006.3453.

[10] Y. Yamashita and D. B. Geselowitz, "Source-field relationships for cardiac generators on the heart surface based on their transfer coefficients," *IEEE Trans Biomed Eng*, pp. 964–970, 1985. doi:10.1109/TBME.1985.325647

[11] D. B. Geselowitz, "On the theory of the electrocardiogram," in *Proc IEEE*, vol. 77, no. 6, 1989, pp. 857–876. doi:10.1109/5.29327

[12] A. van Oosterom, "Solidifying the solid angle," *J Electrocardiol*, vol. 35 Suppl, pp. 181–192, 2002. doi:10.1054/jelc.2002.37176

[13] V. Kalinin, A. Kalinin, W. H. W. Schulze, D. Potyagaylo, and A. Shlapunov, "On the correctness of the transmembrane potential based inverse problem of ECG," in *Comput Cardiol*, 2017, pp. 1–4. doi:10.22489/CinC.2017.077-438

[14] J. Malmivuo and R. Plonsey, *Bioelectromagnetism: principles and applications of bioelectric and biomagnetic fields*. Oxford University Press, 1995. doi:10.1093/acprof:oso/9780195058239.001.0001

[15] M. Stenroos, V. Mäntynen, and J. Nenonen, "A Matlab library for solving quasi-static volume conduction problems using the boundary element method," *Comput Methods Programs Biomed*, vol. 88, pp. 256–263, 2007. doi:10.1016/j.cmpb.2007.09.004

[16] M. S. Lynn and W. P. Timlake, "The use of multiple deflations in the numerical solution of singular systems of equations, with applications to potential theory," *SIAM J Numer Anal*, vol. 5, pp. 303–322, 1968.

[17] M. Potse, B. Dube, and A. Vinet, "Cardiac anisotropy in boundary-element models for the electrocardiogram," *Med Biol Eng Comput*, vol. 47, pp. 719–29, 2009. doi:10.1007/s11517-009-0472-x

[18] M. Stenroos, "The transfer matrix for epicardial potential in a piece-wise homogeneous thorax model: the boundary element formulation," *Phys Med Biol*, vol. 54, p. 5443, 2009. doi:10.1088/0031-9155/54/18/006

[19] D. Potyagaylo, "Non-invasive electrocardiographic imaging of ventricular activities: Data-driven and model-based approaches," PhD thesis, Institute of Biomedical Engineering, Karlsruhe Institute of Technology (KIT), 2016. doi:10.5445/IR/1000058533

[20] P. C. Franzone and L. Guerri, "Spreading of excitation in 3-D models of the anisotropic cardiac tissue. I. validation of the eikonal model," *Math Biosci*, vol. 113, pp. 145–209, 1993. doi:10.1016/0025-5564(93)90001-Q

[21] Z. Fu, R. M. Kirby, and R. T. Whitaker, "A fast iterative method for solving the eikonal equation on tetrahedral domains," *SIAM J Sci Comput*, vol. 35, pp. c473–94, 2013. doi:10.1137/120881956

[22] D. D. Streeter, H. M. Spotnitz, D. P. Patel, R. J. J, and E. H. Sonnenblick, "Fiber orientation in the canine left ventricle during diastole and systole," *Circ Res*, vol. 24, pp. 339–347, 1969. doi:10.1161/01.RES.24.3.339

[23] J. D. Bayer, R. C. Blake, G. Plank, and N. A. Trayanova, "A novel rule-based algorithm for assigning myocardial fiber orientation to computational heart models," *Ann Biomed Eng*, vol. 40, pp. 2243–2254, 2012. doi:10.1007/s10439-012-0593-5

[24] D. Panozzo and A. Jacobson, "libigl tutorial," accessed: 2021-10-01. https://libigl.github.io/tutorial

[25] A. Jacobson, "Algorithms and interfaces for real-time deformation of 2D and 3D shapes," PhD thesis, Swiss Federal Institute of Technology (ETH) Zürich, 2013. doi:10.3929/ethz-a-009790664

[26] A. Jacobson, "gptoolbox: Geometry processing toolbox," 2021. https://github.com/alecjacobson/gptoolbox

[27] G. Golub and C. Van Loan, *Matrix computations*, 4th ed., Johns Hopkins Studies in the Mathematical Sciences. Johns Hopkins University Press, 2013.

[28] J. Hadamard, "Sur les problèmes aux dérivées partielles et leur signification physique," *Princeton university bulletin*, pp. 49–52, 1902.

[29] A. J. Pullan, L. K. Cheng, M. P. Nash, A. Ghodrati, R. MacLeod, and D. H. Brooks, "The inverse problem of electrocardiography," in *Comprehensive Electrocardiology*. Springer, 2010, pp. 299–344. doi:10.1007/978-1-84882-046-3_9

[30] P. C. Hansen, "REGULARIZATION TOOLS: A matlab package for analysis and solution of discrete ill-posed problems," *Numer Algorithms*, vol. 6, pp. 1–35, 1994. doi:10.1007/BF02149761

[31] A. N. Tikhonov and V. Y. Arsenin, *Solutions of ill-posed problems*. Winston & Sons, New York, 1977.

[32] M. Milanic, V. Jazbinsek, R. S. Macleod, D. H. Brooks, and R. Hren, "Assessment of regularization techniques for electrocardiographic imaging," *J Electrocardiol*, vol. 47, pp. 20–28, 2014. doi:10.1016/j.jelectrocard.2013.10.004

[33] P. C. Hansen, "The L-curve and its use in the numerical treatment of inverse problems," in *Computational Inverse Problems in Electrocardiology*. WIT Press, 2000, pp. 119–142.

[34] J. P. Barnes and P. R. Johnston, "Application of robust generalised cross-validation to the inverse problem of electrocardiology," *Comput Biol Med*, vol. 69, pp. 213–25, 2016. doi: 10.1016/j.compbiomed.2015.12.011

[35] J. Chamorro-Servent, R. Dubois, and Y. Coudière, "Considering new regularization parameter-choice techniques for the tikhonov method to improve the accuracy of electrocardiographic imaging," *Front Physiol*, vol. 10, 2019. doi:10.3389/fphys.2019.00273

[36] J. Bayer, A. J. Prassl, A. Pashaei, et al., "Universal ventricular coordinates: A generic framework for describing position within the heart and transferring data." *Med Image Anal*, vol. 45, pp. 83–93, 2018. doi:10.1016/j.media.2018.01.005

[37] S. Schuler, N. Pilia, D. Potyagaylo, and A. Loewe, "Cobiveco: Consistent biventricular coordinates for precise and intuitive description of position in the heart – with MATLAB implementation," *Med Image Anal*, vol. 74, p. 102247, 2021, arxiv:2102.02898. doi:10.1016/j.media.2021.102247

[38] A. J. Yezzi and J. L. Prince, "An Eulerian PDE approach for computing tissue thickness." *IEEE Trans Med Imaging*, vol. 22, pp. 1332–9, 2003. doi:10.1109/TMI.2003.817775

[39] C. Dapogny, C. Dobrzynski, and P. Frey, "Three-dimensional adaptive domain remeshing, implicit domain meshing, and applications to free and moving boundary problems," *J Comput Phys*, vol. 262, pp. 358–378, 2014. doi:10.1016/j.jcp.2014.01.005

[40] W. Bai, W. Shi, A. de Marvao, et al., "A bi-ventricular cardiac atlas built from 1000+ high resolution MR images of healthy subjects and an analysis of shape and motion." *Med Image Anal*, vol. 26, pp. 133–45, 2015. doi:10.1016/j.media.2015.08.009

[41] S. Schuler and A. Loewe, "Biventricular statistical shape model of the human heart adapted for computer simulations," 2021. doi:10.5281/zenodo.4506463

[42] S. Schuler, M. Schaufelberger, L. R. Bear, et al., "Reducing line-of-block artifacts in cardiac activation maps estimated using ECG imaging: A comparison of source models and estimation methods," *IEEE Trans Biomed Eng*, 2021, arxiv:2108.06602. doi:10.1109/TBME.2021.3135154

[43] A. van Oosterom and G. J. Huiskamp, "The effect of torso inhomogeneities on body surface potentials quantified using "tailored" geometry," *J Electrocardiol*, vol. 22, pp. 53–72, 1989. doi:10.1016/0022-0736(89)90023-X

[44] D. A. Brody, "A theoretical analysis of intracavitary blood mass influence on the heart-lead relationship," *Circ Res*, vol. 4, pp. 731–738, 1956. doi:10.1161/01.RES.4.6.731

[45] A. van Oosterom and R. Plonsey, "The brody effect revisited," *J Electrocardiol*, vol. 24, pp. 339–348, 1991. doi:10.1016/0022-0736(91)90016-f

[46] S. Schuler, D. Potyagaylo, and O. Dössel, "ECG imaging of simulated atrial fibrillation: Imposing epi-endocardial similarity facilitates the reconstruction of transmembrane voltages," in *Comput Cardiol*, vol. 44, 2017. doi:10.22489/CinC.2017.245-303

[47] B. Erem, J. Coll-Font, R. M. Orellana, P. Stovicek, and D. H. Brooks, "Using transmural regularization and dynamic modeling for noninvasive cardiac potential imaging of endocardial pacing with imprecise thoracic geometry," *IEEE Trans Med Imaging*, vol. 33, pp. 726–738, 2014. doi:10.1109/TMI.2013.2295220

[48] C. Geuzaine and J.-F. Remacle, "Gmsh: A 3-D finite element mesh generator with built-in pre- and post-processing facilities," *Int J Numer Methods Eng*, vol. 79, pp. 1309–1331, 2009. doi:10.1002/nme.2579

[49] T. F. Oostendorp, A. van Oosterom, and G. Huiskamp, "Interpolation on a triangulated 3D surface," *J Comput Phys*, vol. 80, pp. 331–343, 1989. doi:10.1016/0021-9991(89)90103-4

[50] M. Andreux, E. Rodolà, M. Aubry, and D. Cremers, "Anisotropic Laplace-Beltrami operators for shape analysis," in *Computer Vision - ECCV 2014 Workshops*, Lect Notes Comput Sci, vol. 8928. Springer, 2015, pp. 299–312. doi:10.1007/978-3-319-16220-1_21

[51] S. Schuler, J. D. Tate, T. F. Oostendorp, R. S. MacLeod, and O. Dössel, "Spatial downsampling of surface sources in the forward problem of electrocardiography," in *Functional Imaging and Modeling of the Heart (FIMH)*, Lect Notes Comput Sci, vol. 11504. Springer, 2019, pp. 29–36. doi:10.1007/978-3-030-21949-9_4

[52] F. Greensite and G. Huiskamp, "An improved method for estimating epicardial potentials from the body surface," *IEEE Trans Biomed Eng*, vol. 45, pp. 98–104, 1998. doi:10.1109/10.650360

[53] W. H. W. Schulze, Z. Chen, J. Relan, et al., "ECG imaging of ventricular tachycardia: evaluation against simultaneous non-contact mapping and CMR-derived grey zone," *Med Biol Eng Comput*, pp. 1–12, 2016. doi:10.1007/s11517-016-1566-x

[54] B. Messnarz, B. Tilg, R. Modre, G. Fischer, and F. Hanser, "A new spatiotemporal regularization approach for reconstruction of cardiac transmembrane potential patterns," *IEEE Trans Biomed Eng*, vol. 51, pp. 273–281, 2004. doi:10.1109/TBME.2003.820394

[55] M. Grant and S. Boyd, "CVX: Matlab software for disciplined convex programming, version 2.2," http://cvxr.com/cvx, 2020.

[56] E. D. Andersen, MOSEK ApS, *The MOSEK optimization toolbox, version 9.2.38*, 2021. https://www.mosek.com

[57] A. G. Kléber, M. J. Janse, and V. G. Fast, *Normal and abnormal conduction in the heart*. American Cancer Society, 2011, pp. 455–530. doi:10.1002/cphy.cp020112

[58] J. Coll-Font, L. Wang, and D. Brooks, "A common-ground review of the potential for machine learning approaches in electrocardiographic imaging based on probabilistic graphical models," in *Comput Cardiol*, vol. 45, 2018. doi:10.22489/CinC.2018.348

[59] D. H. Brooks, G. F. Ahmad, R. S. MacLeod, and G. M. Maratos, "Inverse electrocardiography by simultaneous imposition of multiple constraints," *IEEE Trans Biomed Eng*, vol. 46, pp. 3–18, 1999. doi:10.1109/10.736746

[60] G. Huiskamp and F. Greensite, "A new method for myocardial activation imaging," *IEEE Trans Biomed Eng*, vol. 44, pp. 433–446, 1997. doi:10.1109/10.581930

[61] P. M. van Dam, T. F. Oostendorp, A. C. Linnenbank, and A. van Oosterom, "Non-invasive imaging of cardiac activation and recovery," *Ann Biomed Eng*, vol. 37, pp. 1739–1756, 2009. doi:10.1007/s10439-009-9747-5

[62] A. M. Janssen, D. Potyagaylo, O. Dössel, and T. F. Oostendorp, "Assessment of the equivalent dipole layer source model in the reconstruction of cardiac activation times on the basis of BSPMs produced by an anisotropic model of the heart." *Med Biol Eng Comput*, vol. 56, pp. 1013–1025, 2018. doi:10.1007/s11517-017-1715-x

[63] B. Erem, P. M. van Dam, and D. H. Brooks, "Identifying model inaccuracies and solution uncertainties in noninvasive activation-based imaging of cardiac excitation using con- vex relaxation," *IEEE Trans Med Imaging*, vol. 33, pp. 902–12, 2014. doi:10.1109/TMI.2014.2297952

[64] S. Schuler, D. Potyagaylo, and O. Dössel, "Delay-based regularization for ECG imaging of transmembrane voltages," in *Comput Cardiol*, vol. 46, 2019. doi:10.22489/CinC.2019.375

[65] Q. Ni, R. S. MacLeod, R. L. Lux, and B. Taccardi, "A novel interpolation method for electric potential fields in the heart during excitation," *Ann Biomed Eng*, vol. 26, pp. 597–607, 1998. doi:10.1114/1.41

[66] S. Schuler, A. Wachter, and O. Dössel, "Electrocardiographic imaging using a spatio-temporal basis of body surface potentials—application to atrial ectopic activity," *Front Physiol*, vol. 9:1126, 2018. doi:10.3389/fphys.2018.01126

[67] S. Schuler, D. Potyagaylo, and O. Dössel, "Using a spatio-temporal basis for ECG imaging of ventricular pacings: Insights from simulations and first application to clinical data," in *Conf Proc IEEE Eng Med Biol Soc*, 2019, pp. 1559–1562. doi:10.1109/EMBC.2019.8857537

[68] M. J. M. Cluitmans, M. Clerx, N. Vandersickel, R. L. M. Peeters, P. G. A. Volders, and R. L. Westra, "Physiology-based regularization of the electrocardiographic inverse problem." *Med Biol Eng Comput*, vol. 55, pp. 1353–1365, 2017. doi:10.1007/s11517-016-1595-5

[69] S. Xie, R. Girshick, P. Dollár, Z. Tu, and K. He, "Aggregated residual transformations for deep neural networks," in *Proc IEEE Comput Soc Conf Comput Vis Pattern Recognit*, 2017, pp. 1492–1500. doi:10.1109/CVPR.2017.634

[70] S. Schuler, N. Pilia, M. Rees, et al., "Non-invasive localization of the ventricular excitation origin without patient-specific geometries using deep learning," ahead of submission.

[71] G. B. Moody, W. Muldrow, and R. G. Mark, "A noise stress test for arrhythmia detectors," in *Comput Cardiol*, vol. 11, no. 3, 1984, pp. 381–384.

[72] B. Erem, D. H. Brooks, P. M. van Dam, J. G. Stinstra, and R. S. MacLeod, "Spatiotemporal estimation of activation times of fractionated ECGs on complex heart surfaces," in *Conf Proc IEEE Eng Med Biol Soc*, 2011, pp. 5884–5887. doi:10.1109/IEMBS.2011.6091455

[73] A. S. Revishvili, E. Wissner, D. S. Lebedev, et al., "Validation of the mapping accuracy of a novel non-invasive epicardial and endocardial electrophysiology system," *Europace*, vol. 17, pp. 1282–1288, 2015. doi:10.1093/europace/euu339

[74] M. Chmelevsky, M. Budanova, S. Zubarev, D. Potyagaylo, T. Treshkur, and D. Lebedev, "Clinical evaluation of noninvasive ECGI epi-endocardial mapping accuracy," in *Comput Cardiol*, vol. 45, 2018, pp. 1–4. doi:10.22489/CinC.2018.387

[75] W. Jakob, M. Tarini, D. Panozzo, and O. Sorkine-Hornung, "Instant field-aligned meshes," *ACM Trans Graph*, vol. 34, pp. 1–15, 2015. doi:10.1145/2816795.2818078

[76] L. R. Bear, Y. Serinagaoglu, W. W. Good, et al., "The impact of torso signal processing on noninvasive electrocardiographic imaging reconstructions," *IEEE Trans Biomed Eng*, pp. 436–447, 2020. doi:10.1109/TBME.2020.3003465

[77] R. S. MacLeod, Q. Ni, B. Punske, P. R. Ershler, B. Yilmaz, and B. Taccardi, "Effects of heart position on the body-surface electrocardiogram," *J Electrocardiol*, vol. 33, pp. 229–237, 2000. doi:10.1054/jelc.2000.20357

[78] D. J. Swenson, S. E. Geneser, J. G. Stinstra, R. M. Kirby, and R. S. MacLeod, "Cardiac position sensitivity study in the electrocardiographic forward problem using stochastic collocation and boundary element methods," *Ann Biomed Eng*, vol. 39, p. 2900, 2011. doi:10.1007/s10439-011-0391-5

[79] U. C. Nguyên, M. Potse, F. Regoli, et al., "An in-silico analysis of the effect of heart position and orientation on the ECG morphology and vectorcardiogram parameters in patients with heart failure and intraventricular conduction defects," *J Electrocardiol*, vol. 48, pp. 617–625, 2015. doi:10.1016/j.jelectrocard.2015.05.004

[80] M. Rodrigo, A. M. Climent, A. Liberos, et al., "Solving inaccuracies in anatomical models for electrocardiographic inverse problem resolution by maximizing reconstruction quality," *IEEE Trans Med Imaging*, vol. 37, pp. 733–740, 2017. doi:10.1109/TMI.2017.2707413

[81] J. Coll-Font and D. H. Brooks, "Tracking the position of the heart from body surface potential maps and electrograms," *Front Physiol*, vol. 9, p. 1727, 2018. doi:10.3389/fphys.2018.01727

[82] J. A. Bergquist, J. Coll-Font, B. Zenger, et al., "Improving localization of cardiac geometry using ECGI," in *Comput Cardiol*, 2020, pp. 1–4. doi:10.22489/CinC.2020.273

[83] C. Ramanathan and Y. Rudy, "Electrocardiographic imaging: II. effect of torso inhomogeneities on noninvasive reconstruction of epicardial potentials, electrograms, and isochrones," *J Cardiovasc Electrophysiol*, vol. 12, pp. 241–252, 2001. doi:10.1046/j.1540-8167.2001.00241.x

[84] L. R. Bear, L. K. Cheng, I. J. LeGrice, et al., "Forward problem of electrocardiography: is it solved?" *Circ Arrhythm*, vol. 8, pp. 677–684, 2015. doi:10.1161/CIRCEP.114.001573

[85] M. J. Cluitmans, P. Bonizzi, J. M. Karel, et al., "In vivo validation of electrocardiographic imaging," *JACC Clin Electrophysiol*, vol. 3, pp. 232–242, 2017. doi:10.1016/j.jacep.2016.11.012

[86] P. C. Stanley, T. C. Pilkington, and M. N. Morrow, "The effects of thoracic inhomogeneities on the relationship between epicardial and torso potentials," *IEEE Trans Biomed Eng*, pp. 273–284, 1986. doi:10.1109/TBME.1986.325711

[87] D. U. Keller, F. M. Weber, G. Seemann, and O. Dössel, "Ranking the influence of tissue conductivities on forward-calculated ECGs," *IEEE Trans Biomed Eng*, vol. 57, pp. 1568–1576, 2010. doi:10.1109/TBME.2010.2046485

[88] S. Ghimire, J. Dhamala, J. Coll-Font, et al., "Overcoming barriers to quantification and comparison of electrocardiographic imaging methods: A community-based approach," in *Comput Cardiol*, 2017, pp. 1–4. doi:10.22489/CinC.2017.370-289

[89] J. D. Tate, W. W. Good, N. Zemzemi, et al., "Uncertainty quantification of the effects of segmentation variability in ECGI," in *Functional Imaging and Modeling of the Heart (FIMH)*, Lect Notes Comput Sci. Springer, 2021, pp. 515–522. doi:10.1007/978-3-030-78710-3_49

[90] T. Bacoyannis, B. Ly, N. Cedilnik, H. Cochet, and M. Sermesant, "Deep learning formulation of electrocardiographic imaging integrating image and signal information with data-driven regularization," *EP Eur*, vol. 23, pp. i55–i62, 2021. doi:10.1093/europace/euaa391

[91] K. Bujnarowski, P. Bonizzi, M. Cluitmans, R. Peeters, and J. Karel, "CT-scan free neural network-based reconstruction of heart surface potentials from ECG recordings," in *Comput Cardiol*, 2020, pp. 1–4. doi:10.22489/CinC.2020.200

[92] M. Alawad and L. Wang, "Learning domain shift in simulated and clinical data: localizing the origin of ventricular activation from 12-lead electrocardiograms," *IEEE Trans Med Imaging*, vol. 38, pp. 1172–1184, 2018. doi:10.1109/TMI.2018.2880092

[93] D. Potyagaylo, W. H. Schulze, and O. Dössel, "Local regularization of endocardial and epicardial surfaces for better localization of ectopic beats in the inverse problem of ECG," in *Comput Cardiol*, 2014, pp. 837–840.

[94] T. Köhler, M. Wagner, M. Fuchs, H.-A. Wischmann, R. Drenckhahn, and A. Theißen, "Depth normalization in MEG/EEG current density imaging," in *Conf Proc IEEE Eng Med Biol Soc*, vol. 2, 2006, pp. 812–813. doi:10.1109/IEMBS.1996.651989

List of Publications and Supervised Theses

Journal Articles

- **S. Schuler**, M. Schaufelberger, L. R. Bear, J. A. Bergquist, M. J. M. Cluitmans, J. Coll-Font, Ö. N. Onak, B. Zenger, A. Loewe, R. S. MacLeod, D. H. Brooks, and O. Dössel, *Reducing Line-of-block Artifacts in Cardiac Activation Maps Estimated Using ECG Imaging: A Comparison of Source Models and Estimation Methods*, IEEE Trans Biomed Eng, 2021.
- **S. Schuler**, N. Pilia, D. Potyagaylo, and A. Loewe, *Cobiveco: Consistent biventricular coordinates for precise and intuitive description of position in the heart – with MATLAB implementation*, Med Image Anal, vol. 74:102247, 2021.
- **S. Schuler**, A. Wachter, and O. Dössel, *Electrocardiographic Imaging Using a Spatio-Temporal Basis of Body Surface Potentials – Application to Atrial Ectopic Activity*, Front Physiol, vol. 9:1126, 2018.
- **S. Schuler**, N. Pilia, M. Rees, G. Moik, D. Potyagaylo, A. Loewe, and O. Dössel, *Non-invasive Localization of the Ventricular Excitation Origin Without Patient-specific Geometries Using Deep Learning*, ahead of submission.
- C. Nagel, **S. Schuler**, O. Dössel, and A. Loewe, *A bi-atrial statistical shape model for large-scale in silico studies of human atria: Model development and application to ECG simulations*, Med Image Anal, vol. 74:102210, 2021.
- C. Nagel, G. Luongo, L. Azzolin, **S. Schuler**, O. Dössel, and A. Loewe, *Non-Invasive and Quantitative Estimation of Left Atrial Fibrosis Based on P Waves of the 12-Lead ECG-A Large-Scale Computational Study Covering Anatomical Variability*, J Clin Med, vol. 10(8):1797, 2021.
- L. Azzolin, **S. Schuler**, O. Dössel, and A. Loewe, *A Reproducible Protocol to Assess Arrhythmia Vulnerability: Pacing at the End of the Effective Refractory Period*, Front Physiol, vol. 12:656411, 2021.
- R. Moss, E. M. Wülfers, **S. Schuler**, A. Loewe, and G. Seemann, *Impact of cardiac contraction on the ECG – an electro-mechanical whole-heart in silico study*, Front Physiol, 2021.

- T. Gerach, **S. Schuler**, A. Wachter, and A Loewe, *The impact of standard ablation strategies for atrial fibrillation on cardiovascular performance in a four-chamber heart model*, ahead of submission.

- T. Gerach, **S. Schuler**, J. Fröhlich, L. Lindner, E. Kovacheva, R. Moss, E. M. Wülfers, G. Seemann, C. Wieners, and A. Loewe, *Electro-Mechanical Whole-Heart Digital Twins: A Fully Coupled Multi-Physics Approach*, Mathematics, vol. 9(11):1247, 2021.

- E. Kovacheva, T. Gerach, **S. Schuler**, M. Ochs, O. Dössel, and A. Loewe, *Causes of altered ventricular mechanics in hypertrophic cardiomyopathy: an in-silico study*, Biomed Eng Online, vol. 20(69), 2021.

- G. Luongo, L. Azzolin, **S. Schuler**, M. W. Rivolta, T. P. Almeida, J. P. Martínez, D. C. Soriano, A. Luik, B. Müller-Edenborn, A. Jadidi, O. Dössel, R. Sassi, P. Laguna, and A. Loewe, *Machine learning enables noninvasive prediction of atrial fibrillation driver location and acute pulmonary vein ablation success using the 12-lead ECG*, Cardiovascular Digital Health Journal, vol. 2(2), pp. 126-136, 2021.

- G. Luongo, **S. Schuler**, A. Luik, T. P. Almeida, D. C. Soriano, O. Dössel, and A. Loewe, *Non-Invasive Characterization of Atrial Flutter Mechanisms Using Recurrence Quantification Analysis on the ECG: A Computational Study*, IEEE Trans Biomed Eng, vol. 68(3), pp. 914-925, 2021.

- J. van der Waal, V. Meijborg, **S. Schuler**, R. Coronel, and T. Oostendorp, *In silico validation of electrocardiographic imaging to reconstruct the endocardial and epicardial repolarization pattern using the equivalent dipole layer source model*, Med Biol Eng Comput, vol. 58, pp. 1739–1749, 2020.

- D. Nairn, H. Lehrmann, B. Müller-Edenborn, **S. Schuler**, T. Arentz, O. Dössel, A. Jadidi, and A. Loewe, *Comparison of Unipolar and Bipolar Voltage Mapping for Localization of Left Atrial Arrhythmogenic Substrate in Patients With Atrial Fibrillation*, Front Physiol, vol. 11:575846, 2020.

- M. Keller, **S. Schuler**, M. Wilhelms, G. Lenis, G. Seemann, C. Schmitt, O. Dössel, and A. Luik, *Characterization of Radiofrequency Ablation Lesion Development Based on Simulated and Measured Intracardiac Electrograms*, IEEE Trans Biomed Eng, vol. 61(9), pp. 2467-2478, 2014.

Refereed Conference Articles

- **S. Schuler**, D. Potyagaylo, and O. Dössel, *Delay-Based Regularization for ECG Imaging of Transmembrane Voltages*, Comput Cardiol, vol. 46, 2019.

- M. Schaufelberger, **S. Schuler**, L. Bear, M. Cluitmans, J. Coll-Font, O. N. Onak, O. Dössel, and D. Brooks, *Comparison of Activation Times Estimation for Potential-Based ECG Imaging*, Comput Cardiol, vol. 46, 2019.

- **S. Schuler**, D. Potyagaylo, and O. Dössel, *Using a Spatio-Temporal Basis for ECG Imaging of Ventricular Pacings: Insights From Simulations and First Application to Clinical Data*, Conf Proc IEEE Eng Med Biol Soc, pp. 1559-1562, 2019.

- **S. Schuler**, J. D. Tate, T. F. Oostendorp, R. S. MacLeod, and O. Dössel, *Spatial Downsampling of Surface Sources in the Forward Problem of Electrocardiography*, Funct Imaging Model Heart, vol. 11504, pp. 29-36, 2019.

- J. D. Tate, **S. Schuler**, O. Dössel, R. S. MacLeod, and T. F. Oostendorp, *Correcting Undersampled Cardiac Sources in Equivalent Double Layer Forward Simulations*, Funct Imaging Model Heart, vol. 11504, pp. 147-155, 2019.

- **S. Schuler**, A. Loewe, and O. Dössel, *Forcing Transmembrane Voltages to Decrease Slowly: A Temporal Regularization for ECG Imaging*, Comput Cardiol, vol. 45, 2018.

- **S. Schuler**, D. Potyagaylo, and O. Dössel, *ECG Imaging of Simulated Atrial Fibrillation: Imposing Epi-Endocardial Similarity Facilitates the Reconstruction of Transmembrane Voltages*, Comput Cardiol, vol. 44, 2017.

- J. Brenneisen, **S. Schuler**, E. Kovacheva, T. Gerach, O. Dössel, and A. Loewe, *Influence of Geometrical Properties for the Calculation of a Pressure-Free Whole Heart Geometry.* WCCM-ECCOMAS, pp. 1-9, 2020.

- G. Luongo, **S. Schuler**, M. W. Rivolta, O. Dössel, R. Sassi, and A. Loewe, *Automatic ECG-based Discrimination of 20 Atrial Flutter Mechanisms: Influence of Atrial and Torso Geometries*, Comput Cardiol, vol. 47, 2020.

- T. Gerach, **S. Schuler**, E. Kovacheva, O. Dössel, and A. Loewe, *Consequences of Using an Orthotropic Stress Tensor for Left Ventricular Systole*, Comput Cardiol, vol. 47, 2020.

- E. Kovacheva, L. Baron, **S. Schuler**, T. Gerach, O. Dössel, and A. Loewe, *Optimization Framework to Identify Constitutive Law Parameters of the Human Heart*, Cur Dir Biomed Eng, vol. 6(3), pp. 95-98, 2020.

- A. Müller, E. Kovacheva, **S. Schuler**, O. Dössel, and L. Baron, *Effects of local activation times on the tension development of human cardiomyocytes in a computational model*, Cur Dir Biomed Eng, vol. 4(1), pp. 247-250, 2018.

- J. Greiner, S. Pollnow, **S. Schuler**, G. Lenis, G. Seemann, and O. Dössel, *Simulation of intracardiac electrograms around acute ablation lesions*, Cur Dir Biomed Eng, vol. 2(1), pp. 607-610, 2016.

- **S. Schuler**, M. W. Keller, T. Oesterlein, G. Seemann, and O. Dössel, *Influence of Catheter Orientation, Tissue Thickness and Conduction Velocity on the Intracardiac Electrogram*, Biomed Eng / Biomed Tech, vol. 58(s1), 2013.

- M. W. Keller, **S. Schuler**, A. Luik, C. Schmitt, and O. Dössel, *Evaluating changes in electrogram morphology during radiofrequency ablation of cardiac arrhythmias*, Biomed Eng / Biomed Tech, vol. 58(s1), 2013.

- M. W. Keller, **S. Schuler**, A. Luik, G. Seemann, C. Schilling, C. Schmitt, and O. Dössel, *Comparison of simulated and clinical intracardiac electrograms*, Conf Proc IEEE Eng Med Biol Soc, pp. 6858-6861, 2013.

- M. W. Keller, **S. Schuler**, G. Seemann, and O. Dössel, *Differences in intracardiac signals on a realistic catheter geometry using mono and bidomain models*, Comput Cardiol, vol. 39, pp. 305-308, 2012.

Refereed Conference Abstracts

- **S. Schuler**, L. Baron, A. Loewe, and O. Dössel, *Developing and coupling a lumped element model of the closed loop human vascular system to a model of cardiac mechanics*, Biomed Eng / Biomed Tech, vol. 62(S1), p. S69, 2017.
- L. Azzolin, J. Sanchez, **S. Schuler**, O. Dössel, and A. Loewe, *Initiation and maintenance of re-entrant cardiac propagation: a computational vulnerability study*, GRC Cardiac Arrhythmia Mechanisms, 2019.
- G. Luongo, **S. Schuler**, T. P. Almeida, D. C. Soriano, O. Dössel, and A. Loewe, *Discrimination of Atrial Flutter on Simulated 12-Lead-ECG Signals by Applying Biosignal Processing*, GRC Cardiac Arrhythmia Mechanisms, 2019.
- G. Luongo, **S. Schuler**, O. Dössel, and A. Loewe, *12-Lead ECG Feature Identification to Discriminate Different Types of Atrial Flutter*, Conf Proc IEEE Eng Med Biol Soc, 2019.

Reports and Theses

- **S. Schuler**, and O. Dössel, *Nicht-invasive Bildgebung der Aktivierungssequenzen und des Substrates für ventrikuläre Tachykardien*, Final report for the German Research Foundation (DFG), 2021.
- **S. Schuler**, *New Algorithms to Reconstruct Cardiac Sources and Signals from ECG and BSPM*, Final report for EP Solutions SA, 2020.
- **S. Schuler**, *Developing and Coupling a Lumped Parameter Model of the Closed Loop Human Vascular System to a Model of Cardiac Mechanics*, Master's thesis, Institute of Biomedical Engineering, Karlsruhe Institute of Technology (KIT), 2016.
- **S. Schuler**, *Simulation von intrakardialen Elektrogrammen während der Katheterablation*, Bachelor's thesis, Institute of Biomedical Engineering, Karlsruhe Institute of Technology (KIT), 2012.

Supervised Student Theses

- Maike Rees, *Analysis of the Explainability of a Deep Learning Algorithm for the Localization of Ventricular Ectopic Foci Based on Body Surface Potential Maps*, Master's thesis, Institute of Biomedical Engineering, Karlsruhe Institute of Technology (KIT), 2021.
- Gerald Moik, *Reconstruction of the Excitation Origin in the Ventricles using Body Surface Potential Maps*, Master's thesis, Institute of Biomedical Engineering, Karlsruhe Institute of Technology (KIT), 2019.
- Matthias Schaufelberger, *Activation Times Estimation in ECG Imaging: Comparison of Source Models and Estimation Methods*, Master's thesis, Institute of Biomedical Engineering, Karlsruhe Institute of Technology (KIT), 2019.
- Pedro Álvarez Guirado, *Classification of Atrial Ectopic Beats into Spatial Segments based on the 12-lead ECG*, Master's thesis, Institute of Biomedical Engineering, Karlsruhe Institute of Technology (KIT) / Universitat Politècnica de València (UPV), 2018.

Awards & Grants

- Winner of the Rosanna Degani Young Investigator Award, Computing in Cardiology 2019, Singapore. **S. Schuler**, D. Potyagaylo, and O. Dössel, *Delay-Based Regularization for ECG Imaging of Transmembrane Voltages*.
- Travel scholarship by the German Academic Exchange Service (DAAD), 2019.
- Semi-Finalist at the Rosanna Degani Young Investigator Award competition, Computing in Cardiology 2020, Rimini. Tobias Gerach, **S. Schuler**, E. Kovacheva, O. Dössel, and A. Loewe, *Consequences of Using an Orthotropic Stress Tensor for Left Ventricular Systole*.
- Fellowship for the Summer Course on Image-Based Biomedical Modeling, Park City, Utah, 2017.
- Second prize at the student competition, Annual Conference of the German Society for Biomedical Engineering (DGBMT) 2016, Basel. J. Greiner, S. Pollnow, **S. Schuler**, G. Lenis, G. Seemann, and O. Dössel, *Simulation of Intracardiac Electrograms around Acute Ablation Lesions*.
- Finalist at the student competition, Annual Conference of the German Society for Biomedical Engineering (DGBMT) 2013, Graz. **S. Schuler**, M. W. Keller, T. Oesterlein, G. Seemann, and O. Dössel, *Influence of Catheter Orientation, Tissue Thickness and Conduction Velocity on the Intracardiac Electrogram*.